Large Eddy Simulation of Subsonic Mixing Layers

By

Shaw-Ching Sheen

Dissertation submitted to the Faculty of the
Virginia Polytechnic Institute and State University
in partial fulfillment of the requirements for the degree of
Doctor of Philosophy
in
Engineering Mechanics

APPROVED:

Saad A. Ragab, Chairman

Demetri Telionis

Muhammad R. Hajj

Eugene F. Brown

Wing F. Ng

January, 1993
Blacksburg, Virginia

Large Eddy Simulation of Subsonic Mixing Layers

By

Shaw-Ching Sheen
Saad A. Ragab, Chairman
Engineering Mechanics

(ABSTRACT)

Large eddy simulation is used to study the large-scale structures in a low subsonic mixing layer and their breakdown to small scales. For 3-D simulations, different finite-difference and pseudo-spectral schemes are tested. The (2, 4) MacCormack Scheme developed by Gottlieb and Turkel (1976) shows the best overall performance. It is very fast and supplies enough but not excessive artificial dissipation. Though slower than MacCormack scheme, the pseudo-spectral method has its advantage: high resolution of the high-wavenumber range when adequate de-aliasing scheme is used. When efficient fast Fourier transform routines are available, this method can be a very good alternative to the MacCormack scheme. Most of the simulations use a modified Smagorinsky-type model (Erlabacher *et al.* 1992). The effect of different models and model constants is also studied. It is found that the two subgrid-scale (SGS) models, the Smagorinsky model and the linear combination model (Bardina *et al.* 1983), show significant difference even at the low wavenumber range of the spectra.

In the study of three-dimensional subsonic temporal mixing layers, it is found that the streamwise vortex tubes play an important role in the transition process. The vortex interaction of the streamwise vortex tubes and undulated spanwise vortex structures proves to be the dominant mechanism in the development of three-dimensionality and the subsequent generation of small-scale motions. In the absence of pairing of the spanwise vortex tubes, this vortex interaction causes uneven distribution of vorticity along the span of the spanwise vortex tubes and the breaking of the large structures. Following the breaking of the spanwise vortex tubes, the

secondary streamwise vortex tubes become the dominant vortex structures.

In the case involving pairing, it is found that the relative motion of the spanwise vortex tubes in the pre-pairing process creates much stronger strain rate field between the pairing vortex tubes than the case without pairing. The stronger strain rate field leads to the formation of streamwise vortex tubes with very high vorticity and low induced pressure. This also leads to much stronger vortex interaction between the spanwise and streamwise vortex tubes due to the increased strength of the streamwise vortex tubes.

Acknowledgements

I wish to express my gratitude to Dr. Ragab for his guidance throughout this work and for leading me into the world of free shear flows. Thanks are also due to the other members of my committee: Drs. Telionis, Ng, Brown, and Hajj, for serving in my committee.

I also like to thank Mr. Madhu Sreedhar for reading this manuscript.

Finally thanks to my parents for their support and encouragement.

The research has been supported by the Office of Naval Research under Contracts No. N00014-89-J-1544 and N00014-91-J-1233 (principal investigator, Dr. Saad Ragab). I thank Drs. Spiro Lekoudis and Patrick Purtell, who have been the scientific officers of the contracts.

TABLE OF CONTENTS

Chapter 1: Introduction 1

1.1 Motivation 1

1.2 Convective Mach Number 2

1.3 Large-scale Structures of Mixing Layers 3

1.4 Linear Stability Analysis 4

1.5 Numerical Simulation of Turbulent Mixing Layers 5

1.6 Objectives 7

Chapter 2: Numerical Simulation of Turbulent Flows 8

2.1 Direct Numerical Simulations 8

2.2 Large Eddy Simulations 9

2.2.1 Filtering 10

2.2.2 Equations of LES for compressible flows 12

2.2.3 Subgrid-scale model 15

Chapter 3: Numerical Methods 19

3.1 Computational Domain and Boundary Conditions 19

3.1.1 Spatially and temporally developing mixing layers 19

3.1.2 Boundary conditions in the transverse direction 20

3.2 Governing Equations 21

3.2.1 Non-dimensionalization 21

3.2.2 Governing equations of LES 22

3.3 Numerical Schemes 22

3.3.1 MacCormack (2, 4) scheme 23

3.3.2 Runge-Kutta time advancement schemes 24

3.3.3 Evaluation of spatial derivatives 26

3.4 Initial Conditions and Random Flow Field 29

Chapter 4: Two-dimensional Simulations 32

Chapter 5: Control of Large-scale Structures Using Linear Stability Eigenfunctions 34

5.1 Introduction 34

5.2 Major Vortex Structures in a Mixing Layer 35

5.3 Nonlinear Development of Stability Eigenfunctions 38

5.3.1 Phase of the (2, 2) mode 38

5.3.2 Three-dimensional subharmonic mode 40

Chapter 6: Development and Breakdown of Large-scale Structures ... 42

6.1 Computational Box and Initial Conditions 42

6.2 Case A 43

6.3 Case B 48

6.4 Case C 53

6.5 Chapter Summary 54

Chapter 7: Comparison of Numerical Schemes 55

7.1 Comparison of Finite-difference Schemes 55

7.2 Comparison of MacCormack scheme and Pseudo-spectral scheme 56

Chapter 8: Conclusions 59

Bibliography 62

Vita 149

LIST OF ILLUSTRATIONS

Fig. 3.1 Computational box for a temporally developing mixing layer. 67

Fig. 4.1 One-dimensional energy spectra of a 2-D mixing layer, $M^+ = 0.4$, T_2/T_1=1; (a) time = 0, (b) time = 51.2, (c) time = 83.2, (d) time = 128. 68

Fig. 4.2 Vorticity contours, (a) time = 51.2, (b) time = 83.2, (c) time = 128. 70

Fig. 5.1 (A) Spanwise vorticity (ω_z), and (B) transverse velocity (v), contours of the (2, 0) mode in the $x - y$ plane. Negative values are shown by thick lines. 71

Fig. 5.2 The formation of the K-H vortices by the v-perturbations of the (2, 0) mode. 72

Fig. 5.3 (A) ω_z, and (B) v contours of the (1, 0) mode in the $x-y$ plane. Negative values are shown by thick lines, (C) locations of K-H vortices and saddle points of the (1,0) and (2,0) modes, phase difference = $\pi/2$. 73

Fig. 5.4 (A) ω_x, and (B) ω_y contours of the (2, 2) mode in the interface $x - z$ plane. Negative values are shown by thick lines. 75

Fig. 5.5 Contours of the v-perturbations of the (2, 2) mode on the interface and the predicted undulation of the vortex line at $x = 1/4L_x$. Negative values are shown by thick lines. 76

Fig. 5.6 Growth of modal energy. (A) $E^o_{00} - E_{00}$, (B) E_{20}, (C) E_{02}, (D) E_{22}. $A_{20} = 0.02, A_{22} = 0.02$. $\phi_{22} = 0$, — ; $\phi_{22} = \pi/4$, - - - ; $\phi_{22} = \pi/2$, – – –. 77

Fig. 5.7 Growth of momentum thickness. $A_{20} = 0.02, A_{22} = 0.02$. $\phi_{22} = 0$, — ; $\phi_{22} = \pi/4$, - - - ; $\phi_{22} = \pi/2$, – – –. 79

Fig. 5.8 Growth of (A) u', (B) v', and (C) w'. $A_{20} = 0.02, A_{22} = 0.02$. $\phi_{22} = 0$, — ; $\phi_{22} = \pi/4$, - - - ; $\phi_{22} = \pi/2$, – – –. 80

Fig. 5.9 Growth of modal energy. (A) $E^o_{00} - E_{00}$; (B) E_{20}; (C) E_{11}; (D) E_{02}. $A_{20} = 0.02, A_{11} = 0.005$. $\phi_{11} = \pi/2$, — ; $\phi_{11} = \pi$, - - -. 81

Fig. 5.10 Growth of momentum thickness. $A_{20} = 0.02, A_{11} = 0.005$. $\phi_{11} = \pi/2$, —; $\phi_{11} = \pi$, - - -. 83

Fig. 5.11 Growth of (A) u', (B) v', and (C) w'. $A_{20} = 0.02, A_{11} = 0.005$. $\phi_{11} = \pi/2$, —; $\phi_{11} = \pi$, - - -. 84

Fig. 5.12 Projections of low-pressure region in the simulation of helical pairing mode. 85

Fig. 6.1 Growth of modal energy; case A. 86

Fig. 6.2 (A) Contours of spanwise vorticity; $\omega_{max} = -0.039, \omega_{min} = -0.732, \Delta\omega = 0.077$, (B) velocity vectors. Case A, $t = 32.7$; $x - y$ plane, $z = 1/8L_z$. 88

Fig. 6.3 Surface with constant $\omega_{xy}, \sqrt{\omega_x^2 + \omega_y^2}$; case A, $t = 40.8$; (A) perspective view, $\omega_{xy} = 0.25$, (B) projection on the $x - z$ plane, $\omega_{xy} = 0.22$, (C) projection on the $x - y$ plane, $\omega_{xy} = 0.22$. 89

Fig. 6.4 Vortex lines through the streamwise vortex tubes; case A, $t = 40.8$; (A) perspective view, (B) projection on the $x - y$ plane. 91

Fig. 6.5 Surface with constant (A) pressure, $P/(\rho_1 RT_1) = 0.9$, projection on the $x - z$ plane, (B) spanwise vorticity, $\omega_z = -0.85$, projection on the $x - y$ plane; case A, $t = 40.8$. 92

Fig. 6.6 (A) contours of ω_{xy} with the sign of ω_x, $\omega_{max} = 0.689$, $\omega_{min} = -0.689$, negative values are shown by solid lines, (B) velocity vectors; case A, $t = 48.7$; $z - y$ plane, $x = 1/4L_x$; plots are truncated at $y = \pm 12$. ... 93

Fig. 6.7 (A) contours of ω_{xy} with the sign of ω_x, $\omega_{max} = 1.418$, $\omega_{min} = -1.418$, negative values are shown by solid lines, (B) velocity vectors; case A, $t = 64.0$; $z - y$ plane, $x = 1/4L_x$; plots are truncated at $y = \pm 12$. ... 94

Fig. 6.8 Projections of vortex structures on the $x - z$ plane; $t = 64.0$, case A; (A) $P/(\rho_1 RT_1) = 0.91$, (B) $\omega_{xy} = 1.250$. 95

Fig. 6.9 (A) Contours of ω_y, $\omega_{max} = 0.873$, $\omega_{min} = -2.269$, (B) Contours of ω_x, $\omega_{max} = 1.517$; $\omega_{min} = -1.517$; in the $x - y$ plane at $z = 1/8L_z$; negative values are shown by solid lines, plots are truncated at $y = \pm 12$. (C) projection of K-H vortex tube vortex lines on the $x-y$ plane; $t = 64.0$, case A. 96

Fig. 6.10 Projections of large structures on the $x - z$ plane; case A, $t = 71.3$; (A) $P/(\rho_1 RT_1) = 0.88$, (B) $\omega_{xy} = 1.35$, (C) $\omega_z = -1.2$. 98

Fig. 6.11 Growth of kinematic energy for small-scale motions with wavenumber higher than 4α (1.6); case A. 100

Fig. 6.12 Growth of momentum thickness; case A. 101

Fig. 6.13 Growth of modal energy; case B. 102
Fig. 6.14 Growth of momentum thickness; case B. 104
Fig. 6.15 Projection of constant pressure surface and vortex lines on the $x - z$ plane, $P/(\rho_1 RT_1) = 0.89$; $t = 51.2$, case B. 105
Fig. 6.16 Projection of constant ω_{xy} surface on the $x - z$ plane, $\omega_{xy} = 1.1$; $t = 61.4$, case B. 106
Fig. 6.17 Projections of constant pressure surface and vortex lines; (A) on the $x - z$ plane, (B) on the $x - y$ plane, only structures between $z = 0$ and $z = 1/4L_z$ are shown; $P/(\rho_1 RT_1) = 0.89$; $t = 61.4$, case B. 107
Fig. 6.18 Projections of vortex lines in Fig. 6.17; (A) on $x - z$ plane, (B) on $x - y$ plane; $t = 61.4$; case B. 108
Fig. 6.19 Perspective view of vortex lines resulting from the reconnection mechanism; $t = 61.4$; case B. 109
Fig. 6.20 Projections of vortex lines on the $x - z$ and $z - y$ planes; $t = 61.4$; case B. 110
Fig. 6.21 Projections of constant pressure surface; $t = 71.1$, case B; (A) $x - z$ plane, $P/(\rho_1 RT_1) = 0.86$, complete structures, (B) $x - z$ plane, $P/(\rho_1 RT_1) = 0.88$, upper-stream structures, (C) $x - z$ plane, $P/(\rho_1 RT_1) = 0.88$, lower-stream structures, (D) $z - y$ plane, $P/(\rho_1 RT_1) = 0.88$, structures between $x = 1/4L_x$ and $x = 1/2L_x$. 111
Fig. 6.22 Contours in the $z - y$ plane at $x = 1/2L_x$; $t = 71.1$; case B; (A) ω_x; $\omega_{max} = 0.673$, $\omega_{min} = -1.749$, (B) ω_{xy} with the sign of ω_x; $\omega_{max} = 1.755$, $\omega_{min} = -1.755$; negative values are shown by solid lines, plots are truncated at $y = \pm 12$. 113
Fig. 6.23 Projections of the vortex line through point A in Fig. 6.22; $t = 71.1$, case B. 114
Fig. 6.24 Projections of the vortex line through point B in Fig. 6.22; $t = 71.1$, case B. 115
Fig. 6.25 Projections of the vortex line through point C in Fig. 6.22; $t = 71.1$, case B. 116
Fig. 6.26 Projections of constant pressure surface on the $x - z$ plane; $t = 80.6$, case B, $P/(\rho_1 RT_1) = 0.87$; (A) upper-stream structures, (B) lower-stream structures. 117

Fig. 6.27 Projections of constant ω_z surface on the $x-z$ plane; $t = 80.6$; case B, $\omega_z = -1.1$; (A) upper-stream structures, (B) lower-stream structures. 118
Fig. 6.28 Contours of ω_z at $z = 1/4L_z$; $t = 80.6$; case B; $\omega_{max} = 1.243$, $\omega_{min} = -3.231$; negative values are shown by solid lines. 119
Fig. 6.29 Projection of surface with constant vorticity magnitude, $\omega = 1.6$; $t = 80.6$, case B. 120
Fig. 6.30 Contours of ω_z at $z = 1/8L_z$; $t = 80.6$, case B; $\omega_{max} = 1.688$, $\omega_{min} = -1.688$. 121
Fig. 6.31 Contours of ω_z at $z = 1/4L_z$; $\omega_{max} = 1.188$, $\omega_{min} = -3.088$; $t = 80.8$, case B without random disturbance. 122
Fig. 6.32 Projections of vortex lines through the K-H vortex tubes; $t = 71.2$; case B without random disturbance. 123
Fig. 6.33 Projections of constant pressure surface and vortex lines; $t = 80.8$, case B, without random disturbance; $P/(\rho_1 RT_1) = 0.855$; (A) upper-stream structures, on $x-z$ plane, (B) structures between $x = 1/4L_x$ and $x = 1/2L_x$, on $z-y$ plane. 124
Fig. 6.34 Projections of vortex lines; $t = 80.8$; case B, without random disturbance; vortex lines start at $x = 1/2L_x$, along and near the interface ($y = 0$). 125
Fig. 6.35 Projections of vortex lines; $t = 80.8$; case B, without random disturbance; vortex lines start at $z = 5/8L_z$, along and near the interface ($y = 0$). 126
Fig. 6.36 Projections of vortex lines; $t = 80.8$; case B, without random disturbance; vortex lines start at $z = 3/4L_z$, along and near the interface ($y = 0$). 127
Fig. 6.37 Contours of ω_z, $t = 98.9$; case B; (A) at $z = 1/8L_z$, $\omega_{max} = 1.544$, $\omega_{min} = -2.426$, (B) at $z = 1/4L_z$, $\omega_{max} = 1.800$, $\omega_{min} = -1.800$; negative values are shown by solid lines. 128
Fig. 6.38 Projection of constant pressure surface on the $x-z$ plane, $t = 98.9$, $P/(\rho_1 RT_1) = 0.885$, case B 130
Fig. 6.39 Growth of kinematic energy in the small-scale motions; case B. 131
Fig. 6.40 (A) u', —; v', - - -; w', – – –. (B) $\overline{u'v'}$, —; $\overline{u'w'}$, - - -; $\overline{v'w'}$, – – –. $t = 108.4$, case B. 132

Fig. 6.41 Growth history of modal energy; case C. 133
Fig. 6.42 Projection of constant ω_z surface on the $x-z$ plane; $t = 46.9$, case C; $\omega_z = -0.8$. 134
Fig. 6.43 Projections of constant ω_{xy} surface; case C; (A) $t = 56.03$, $\omega_{xy} = 0.65$, on $x-z$ plane, (B) $t = 64.7$, $\omega_{xy} = 1.0$, on $x-z$ plane, (C) $t = 64.7$, $\omega_{xy} = 1.0$, on $z-y$ plane; structures between $x = 0.43L_x$ and $x = 0.93L_x$. 135
Fig. 6.44 (A) projection of constant ω_z surface on the $x-z$ plane, $\omega_z = -0.9$, (B) contours of ω_z in plane A-A in (A), $\omega_{max} = 0.478$, $\omega_{min} = -1.242$, (C) contours of ω_z in the $x-y$ plane at $z = 1/2L_z$, $\omega_{max} = 0.423$, $\omega_{min} = -2.115$; case C, $t = 64.7$. 137
Fig. 6.45 Projections of constant pressure surface on the $x-z$ plane, case C; (A) $t = 89.7$, $P/(\rho_1 RT_1) = 0.90$, (B) $t = 98.9$, $P/(\rho_1 RT_1) = 0.89$. 139
Fig. 6.46 Contours of ω_z; case C, $t = 98.9$; (A) plane A-A in Fig. 6.45, $\omega_{max} = 1.449$, $\omega_{min} = -1.449$, (B) plane B-B in Fig. 6.45, $\omega_{max} = 0.990$, $\omega_{min} = -2.574$; plots are truncated at $y = \pm 15$. 140
Fig. 6.47 Growth of kinematic energy in small-scale motions; case C. 141
Fig. 7.1 Growth of modal energy. o o o, MacCormack, $C_R = 0.05$; - - - -, RK/central-difference, $C_R = 0.10$; —, flux-splitting, $C_R = 0.05$. All use Smagorinsky model. 142
Fig. 7.2 Comparison of 1-D energy spectra (A) $t = 71, E_x$, (B) $t = 71, E_z$, (C) $t = 110, E_x$, (D) $t = 110, E_z$. —, MacCormack with Smagorinsky model, $C_R = 0.05$; - - - -, MacCormack with LCM, $C_R = 0.05$; • • •, flux-splitting/RK, $C_R = 0.05$; o o o, central-difference/RK, $C_R = 0.05$; ◇ ◇ ◇, central-difference/RK, $C_R = 0.10$; △△△, central-difference/RK, $C_R = 0.08$. The RK schemes use Smagorinsky model. 143
Fig. 7.3 Comparison of 1-D energy spectra of different dealiasing schemes; (A) E_x, (B) E_z; + + +, 2-step cut-square; o o o, 1-step cut-square; —, 2-step cut-circle; - - - -, 1-step cut-circle. 144

Fig. 7.4 Comparison of energy spectra of pseudo-spectral method and MacCormack scheme at $t = 71$. (A) E_x, (B) E_z; —, MacCormack with LCM; – – –, MacCormack with Smagorinsky model; + + +, pseudo-spectral with Smagorinsky model; (C) E_{3D}; + + +, MacCormack with LCM; square, MacCormack with Smagorinsky model; —, pseudo-spectral with Smagorinsky model. 145

Fig. 7.5 Comparison of energy spectra of pseudo-spectral method and MacCormack scheme at $t = 99$; (A) E_x, (B) E_z; —, MacCormack with LCM; – – –, MacCormack with Smagorinsky model; + + +, pseudo-spectral with Smagorinsky model; (C) E_{3D}; + + +, MacCormack with LCM; square, MacCormack with Smagorinsky model; —, pseudo-spectral with Smagorinsky model. 147

1. INTRODUCTION

1.1 Motivation

Free shear flows are of essential importance in the study of turbulence. They are found in many situations in nature and practical devices. Understanding the physics of free shear flows is vital for the development of new turbulence models. The plane mixing layer, which is formed by the merging of two parallel streams moving with different velocities, is a simple free shear flow because the driving velocity difference is maintained everywhere.

The behavior of incompressible mixing layers has been studied extensively in the past (for review see Ho and Huerre 1984). These studies have provided a broad understanding of mixing layers. For the compressible mixing layer, much fewer works are available. Stability analyses, experiments and numerical simulations all show that the mixing layer grows much less quickly at high Mach number.

In the study of mixing layers, scalar mixing is of particular interest because of its application to chemically reacting flows, which always involve free shear flows. Numerous experiments (Brown and Roshko 1974, Winant and Browand 1974) and numerical simulations (Riley and Metcalfe 1980, Metcalfe *et al.* 1987, Sandham and Reynolds 1989, 1991) have shown that a mixing layer at low Mach number is dominated by the predominantly two-dimensional vortex structures in the initial stage. This two-dimensional flow is unstable to three-dimensional disturbances, which lead to the generation of streamwise streaks found in experiments (Breidenthal

1980, Bernal and Roshko 1986, Lasheras *et al.* 1986, 1988). Further downstream, the mixing layer undergoes transition to small-scale turbulence if the Reynolds number is high enough. This transition has been called mixing transition because of its strong effect on molecular mixing. It is generally agreed that the transition happens during the sequential pairing process of the two-dimensional structures. However, details about the mechanism leading to the transition and the role of streamwise vortex structures in transition still need further study.

The nonlinearity of the governing equations of fluid mechanics is a primary source of difficulties facing a fluid analyst. The nonlinearity leads to the continuous generation of fluid motions with smaller and smaller scales. Because of the limitation of today's computing capability, the grid systems we use in three-dimensional simulations are not expected to resolve all scales existing in most practical flows. To account for the effect of the scales not resolvable by the grid system, the idea of large eddy simulation was proposed. The key to the success of large eddy simulation is the subgrid-scale (SGS) model. Numerous studies have been performed in the last decade to improve the SGS model (Reynolds 1990). One of the major topic in the research of SGS model is the combined effect of model and numerical dissipation. Since different numerical schemes supply different amount of dissipation at different wavelengths, the choice of model should take into account the artificial dissipation of the numerical scheme.

1.2 Convective Mach Number

A parameter called convective Mach number is proposed by Bogdanoff (1983) and Papamoschou and Roshko (1986) to correlate the compressibility effects on the growth rate of compressible mixing layers. The parameter represents the combined effect of velocity ratio, temperature ratio, and Mach number on the growth of a mixing layer. This parameter is used by Papamoschou and Roshko to correlate their experimental data, and to explain the reduction of growth rate as a result of compressibility.

The reasoning behind the convective Mach number is based on the existence of organized large-scale structure in a compressible mixing layer. For an observer

moving with the large structures, the Mach numbers of the free streams are intrinsic Mach numbers for the flow. For each stream, we have

$$M_1^+ = \frac{U_1^* - U_c^*}{a_1^*} \quad \text{and} \quad M_2^+ = \frac{U_c^* - U_2^*}{a_2^*} \tag{1.1}$$

where 1 and 2 denote the fast and slow streams, respectively, and U_c^* is the convective velocity of the large structures. The free stream velocity for the two streams are U_1^* and U_2^* and a^* is the sound speed. For an incompressible mixing layer moving with U_c^*, there is a stagnation point between two spanwise vortices. If the existence of a similar point is assumed for a compressible mixing layer, and the assumption of isentropic process is valid, then the value of U_c^* can be obtained by requiring the pressure through an isentropic process at the stagnation point to be the same for both streams. The convective Mach number, M^+, is then defined as

$$\begin{aligned} M^+ &= \sqrt{M_1^+ M_2^+} \\ &= \frac{M_1(1-\lambda_U)}{(1+\lambda_\rho^{-1/2})\lambda_\gamma^{1/4}} \end{aligned} \tag{1.2}$$

where λ_U, λ_ρ, and λ_γ are the ratios of slow-stream to fast-stream values for velocity, density, and specific heat ratio, respectively.

1.3 Large-scale Structures of Mixing Layers

Mixing layers are a relatively simple type of flow. Yet, the study of mixing layers yields understanding of the basic fluid dynamics of turbulence and mixing, which can then be applied to more complicated flows.

The basic features of an incompressible mixing layer are the two-dimensional primary vortex structures, which have been observed in most experiments at low Mach number (Brown and Roshko 1974, Winant and Browand 1974, among others). These spanwise vortices are the result of the Kelvin-Helmholtz instability of the shear layer formed by the streamwise velocity difference. Essentially, this two-dimensional instability can be described as an endless redistribution of vorticity which originally exists at the interface (Corcos and Sherman 1984). The sequential pairings of these spanwise vortices are the major mechanism responsible for the growth of the mixing layer, both turbulent and laminar. In addition to the spanwise Kelvin-Helmholtz (K-H)

vortices, another intrinsic feature of mixing layers is the streamwise vortices, which are observed in experiments in the form of streamwise streaks between successive spanwise vortices (Brownd and Roshko 1974, Breidenthal 1980). These secondary structures were studied in detail by Bernal and Roshko (1986), whose results show that these streaks consist of counter-rotating streamwise vortices that wrap around the neighboring Kelvin-Helmholtz primary vortices. Recent works on the origin and evolution of streamwise streaks include those by Lasheras and co-workers (1986, 1988). The secondary structures have also been observed in numerical simulations of mixing layers (Metcalfe *et al.* 1987, Sandham and Reynolds 1989, 1991, Roger and Moser 1991). They evolve from the vorticity perturbations existing between the successive K-H vortices. Under the influence of the strain rate field created by the K-H vortices, these perturbations undergo axial stretching, resulting in the formation of vortex tubes whose axes are aligned with the principal direction of the positive strain (Metcalfe *et al.* 1987, Sandham and Reynolds 1989, 1991). As the strength of streamwise vortices grows to a level comparable to that of the K-H vortices, the streamwise vortex tubes begin to influence the primary spanwise vortex tubes. The interaction between the two sets of vortices causes distortion in the spanwise vortex tubes. The existence of these structures has been verified in various experiments and numerical simulations for incompressible mixing layers. The structures in a highly compressible mixing layer can be very different, however.

1.4 Linear Stability Analysis

Linear stability analysis is an efficient tool for the study of mixing layers in the initial stage. Although unable to replace numerical simulations, it provides valuable information about the range of amplified frequencies, the most amplified frequency, and the maximum growth rate. Its efficiency allows the extensive investigation of effects of such parameters as Mach number, Reynolds number, velocity ratio, temperature ratio, etc. This information proves to be valuable guidelines for numerical simulation and helps avoid the unnecessary waste of computational resources. In addition, the eigenfunctions of stability analysis can provide initial and boundary conditions for numerical simulation. With adequate phases and amplitudes, these eigenfunctions can reproduce the basic structures in a mixing layer.

For an extensive study and literature review of linear stability analysis in a compressible mixing layer, the reader is referred to Ragab and Wu (1988, 1989, and 1990), Wu (1989), and Sandham and Reynolds (1989, 1991).

Most of stability analyses have been conducted for the hyperbolic tangent mean velocity profile. Application to the incompressible mixing layer was presented by Michalke (1965a, 1965b), and Monkewitz and Huerre (1982) and to the compressible one by Lessen *et al.* (1965, 1966). The effects of the mean velocity profiles were studied by Monkewitz and Huerre (1982). The work of Ragab and Wu (1988) on compressible mixing layers shows that the compressible mixing layer, like the incompressible one, has a basically inviscid, inflectional instability. Their results also show that the non-parallel effects are negligible in compressible mixing layers.

In the investigation of secondary stability, the major work is due to Pierrehumbert and Widnall (1982) for the incompressible mixing layer. They used a base state given by Stuart vortex (Stuart 1967). For the 3D fundamental mode, they found that the core 'translative' mode is more unstable than the core 'bulging' mode. As for the subharmonic mode, the most amplified one is the 2D pairing mode.

The only work in secondary stability for the compressible mixing layer was by Ragab and Wu (1989). The basic state they used is the mean profile superimposed on the neutral mode of the two-dimensional primary stability analysis. They found that, above a convective number of 0.4, the helical pairing mode is more amplified than the 2D pairing mode.

1.5 Numerical Simulation of Turbulent Mixing Layers

Techniques for numerical simulation of mixing layers can be divided into two categories: (1) direct numerical simulation (DNS), and (2) large eddy simulation (LES). Direct numerical simulations aim at accurate solutions of the full Navier-Stokes equations with no modeling. However, this approach is limited to low-Reynolds-number flows due to today's limitations in computing power. The first direct nu-

merical simulation of mixing layers was presented by Riley and Metcalfe (1980). Recent works (Metcalfe *et al.* 1987, Moser and Rogers 1991) have shown some experimentally observed phenomena including the secondary streamwise vortices, and the mushroom-shaped structures in the scalar field. Moser and Rogers also made a detailed study of small-scale transition in the mixing layer. Lele (1989) simulated the development of 2D compressible mixing layers using a compact finite-difference scheme with spectral-like accuracy. With the projected increase in computing power, in the foreseeable future, direct numerical simulation will still be used to study turbulence physics, to help in the development of turbulence models, and to assess turbulence closure theories.

The objective of large eddy simulation (LES) is to calculate numerically the large scales of turbulent motion, which are responsible for the primary transport of momentum and energy, using a model for the small scales. It is intended to be used in the study of turbulence at high Reynolds numbers, and in the prediction of flows of technological interests.

The work of Deardorff (1970) on channel flow is the first application of LES to problems of engineering interest. The majority of LES results obtained to date employed an eddy-viscosity-type model (Smagorinsky 1963). An improved model referred to as the linear combination model has been developed and tested by Bardina *et al.* (1983). Erlebacher *et al.* (1990, 1992) presented a generalization of the linear combination model to compressible flows. The major shortcoming of a Smagorinsky-type model is its fixed model constants, which are generally obtained by correlating with the results of DNS of homogeneous turbulence. For different types of flows, the model constants must be adjusted. Moin *et al.* (1991) developed a dynamic subgrid-scale model whose model constants are computed as a function of instantaneous flow variables. Their results of isotropic turbulence agree well with experimental data and DNS data.

However, most of the works on LES fail to investigate the effect of numerical dissipation on small-scale motions and the interaction between the subgrid model and the numerical dissipation. In addition, not much work has been done to study the development of large structures through the analysis of available data obtained in

numerical simulation.

1.6 Objectives

In summary, the topics that will be studied in this work are

- Development of numerical methods for large eddy simulation of transitional and turbulent flows in a compressible mixing layer. The combined effect of turbulence model and numerical dissipation will be studied.
- The study of large-scale structures evolving from different initial conditions, including initial conditions specified by the eigenfunctions of linear stability analysis with different amplitudes and phases. The purpose of this study is to supply information for the control of large vortex structures in a mixing layer.
- The breaking of large-scale structures and the transition process to small scales in a mixing layer. The purpose of this study is to find out the mechanisms that lead to the breakdown of basic vortex structures in a mixing layer.

In chapter 2, the two techniques for numerical simulation of turbulent flows, DNS and LES, will be reviewed. The numerical methods are discussed in chapter 3. A brief introduction of two-dimensional pairing is presented in chapter 4. Most of results are presented in chapters 5, 6, and 7. Chapter 5 discusses the development of various stability eigenfunctions. The study of detailed vortical structures and transition process is presented in chapter 6. In chapter 7, the accuracy of different numerical methods and turbulence models are studied.

2. NUMERICAL SIMULATION OF TURBULENT FLOWS

Experiments, theoretical approaches, and numerical simulations all have important roles in extending our knowledge in turbulence research. Each has its unique importance, and none will replace any other. Compared with experiments, numerical simulations can cover only a small range both in time and in space. Experiments can do many things much faster than numerical simulations, such as statistical analysis. Numerical simulations, however, can supply data that can be obtained in no other way. And, with the rapid development of computer technology, numerical simulations should be able to play an increasingly important role.

2.1 Direct Numerical Simulations

Direct numerical simulations (DNS) resolve all scales of fluid motions from the largest scales imposed by external effects down to the smallest scales which are responsible for the dissipation of turbulent kinetic energy into thermal energy. Since the disparity of scales of fluid motion increases with Reynolds number, this approach is limited to flows with low Reynolds numbers. Because of this limit, DNS is primarily used in the study of turbulence physics and the development of turbulence models instead of predicting flows of technical interests.

Also because turbulence contains a broad range of eddies, DNS generally need highly accurate numerical methods. In the study of homogeneous turbulence, spectral

methods, which provide very accurate spatial differentiation (Orszag and Patterson 1972), have proven to be a powerful tool. Spectral methods, however, are much more difficult to implement in complex domains than finite difference methods. Finite difference methods with near-spectral accuracy (Lele 1989) are beginning to be used in DNS. Rai and Moin (1989) have evaluated promising high-order finite difference methods for DNS, and speculated that these methods may be more cost-effective than spectral methods for complex geometries.

Direct numerical simulations have been very successful in the study of isotropic turbulence (Orszag and Patterson 1972), fully developed channel flow (Kim *et al.* 1987) and zero-pressure-gradient boundary-layer flow (Spalart 1988). There is no doubt that DNS will be of growing importance in providing better understanding of turbulence physics and guidance in turbulence modeling. As the computational capabilities expand, DNS will be used more extensively in scientific studies of turbulence. In addition, application of DNS in engineering problems will become more likely with the growing availability of powerful computers. However, with the projected advances of computers, DNS will still be limited to low Reynolds number for the foreseeable future.

2.2 Large Eddy Simulations

As mentioned before, direct numerical simulation of turbulent flows of technological importance at high Reynolds numbers will not be feasible in the near future due to a wide range of scales existing in such flows. Consequently, reasonable solutions to this kind of problems must be based on some form of turbulence modeling. In the past, different turbulence models have been developed for the Reynolds averaging equations. The major deficiency of this approach is that all scales in the flow must be modeled. Since we expect large structures in the turbulent flows to be highly dependent on geometries, it is difficult to find a universal turbulence model that will work reasonably well in various flows. This explains why the traditional turbulence models have had only limited success.

While the large structures in turbulent flows prove to be difficult to model in a universal way, the small scales, which are much more universal in character than

the large ones, should be less problem dependent and might be modeled successfully. This motivates the idea of calculating the large structures directly and using a model for the small-scale motions.

In large eddy simulation (LES), the large scales of fluid motion, which are responsible for the primary transport, will be computed directly while a model is used for the unresolvable scales. It is intended to be used in the study of turbulent flows at high Reynolds numbers, in the development of turbulence models, and in predicting flows of technical interest.

2.2.1 Filtering

Since the success of LES relies on modeling the small-scale motions while the large structures are computed explicitly, we must find a way to separate the large and small scales mathematically, and this can be achieved by filtering (Leonard 1974).

Filtering is a process by which scales smaller than a certain cut-off value are eliminated from the total flow, and hence it defines the resolvable part of the flow. One can define the filtered variable $\overline{f}$ by

$$\overline{f}(x,t) = \int_D G(x-x',\Delta_f) f(x',t) dx' \tag{2.1}$$

where $G(x-x',\Delta_f)$ is the filter function, D is the flow domain and Δ_f is the filter width, which defines the smallest scales of the resolved field and is generally proportional to the computational mesh. The filter function is normalized by requiring

$$\int_D G(x-x')dx' = 1. \tag{2.2}$$

Also note that in the limit as Δ_f goes to zero, G become a Dirac delta function (Erlebacher 1990), that is

$$\lim_{\Delta_f \to 0} \int_D G(x-x',\Delta_f) f(x',t) dx' = \int_D \delta(x-x') f(x',t) dx' = f(x,t) \tag{2.3}$$

It is assumed that the function G is such that filtering and differentiation with respect to space and time commute, that is

$$\overline{\frac{\partial f}{\partial t}} = \frac{\partial \overline{f}}{\partial t} \tag{2.4}$$

$$\overline{\frac{\partial f}{\partial x_j}} = \frac{\partial \overline{f}}{\partial x_j} \tag{2.5}$$

Equation (2.5) can be satisfied when f or G vanish on the boundary of D.

Following are the one-dimensional forms of three common filters.

(1) Gaussian filter

$$G(x - x', \Delta_f) = (\frac{6}{\pi \Delta_f^2})^{\frac{1}{2}} exp(-6\frac{(x - x')^2}{\Delta_f^{\,2}}), \tag{2.6}$$

The Fourier transforms of f and $\overline{f}$ have the following relation

$$\hat{\overline{f}}(k) = \hat{f}(k) exp(-\frac{1}{24}(k\Delta_f)^2), \tag{2.7}$$

where $\hat{\overline{f}}(k)$ and $\hat{f}(k)$ are the Fourier transforms of $\overline{f}$ and f, respectively, and k is the wavenumber.

This filter is widely used in homogeneous turbulence and in homogeneous directions of inhomogeneous turbulence.

(2) Sharp cut-off filter

This filter will remove all Fourier modes having wavenumbers greater than the specified cutoff, $k_c = \pi/\Delta_f$, and retain all modes with smaller wavenumbers in the resolved field. It is generally used in the direction in which spectral differentiation is used. In physical space, the sharp cut-off has the form

$$G(x - x', \Delta_f) = \frac{sin(\pi(x - x')/\Delta_f)}{\pi(x - x')} \tag{2.8}$$

When this filter is used with spectral methods, the filtering process is done in Fourier space.

(3) Box filter

$$G(x-x',\Delta_f)=\begin{cases}1/\Delta_f \text{ for } & x-\Delta_f/2<x'<x+\Delta_f/2\\ 0 \text{ otherwise}\end{cases} \tag{2.9}$$

This filter represents uniformly-weighted averaging over a finite width.

Filtering in LES is different from the time averaging or ensemble averaging in turbulence theory. When f is decomposed into resolvable scale and subgrid scale, $f=\overline{f}+f'$, it is noted that

$$\overline{f'}\neq 0 \quad \text{and} \quad \overline{\overline{f}}\neq\overline{f} \tag{2.10}$$

except for the sharp cut-off filter (Erlebacher *et al.* 1990).

In multidimensional flow, depending on the numerical methods, the boundary conditions, and the physics of fluid motions, we may use different filters or different filter widths in different directions. The three-dimensional filter function will be obtained from the filter functions in the three directions by the following relation

$$G(\mathbf{x},\mathbf{x}')=\prod_{i=1}^{3}G_i \tag{2.11}$$

where G_i are the filter functions in different directions.

2.2.2 Equations of LES for compressible flows

To obtain the governing equations of LES, we begin with the compressible Navier-Stokes equations

$$\frac{\partial\rho}{\partial t}+\frac{\partial(\rho u_j)}{\partial x_j}=0 \tag{2.12}$$

$$\frac{\partial\rho u_i}{\partial t}+\frac{\partial(\rho u_i u_j+p\delta_{ij}-\tau_{ji})}{\partial x_j}=0 \tag{2.13}$$

$$\frac{\partial\rho E}{\partial t}+\frac{\partial[(\rho E+p)u_j-u_i\tau_{ij}+q_j]}{\partial x_j}=0 \tag{2.14}$$

where ρ, u_j and p are the density, velocity vector and pressure, respectively. The total specific energy is given by

$$E = e + \frac{1}{2}u_j u_j \tag{2.15}$$

where e is the specific internal energy, and the viscous stress tensor τ_{ij} and heat flux vector q_j are given by

$$\tau_{ij} = \lambda \frac{\partial u_k}{\partial x_k}\delta_{ij} + \mu[\frac{\partial u_i}{\partial x_j} + \frac{\partial u_j}{\partial x_i}] \tag{2.16}$$

and

$$q_j = -\kappa \frac{\partial T}{\partial x_j} \tag{2.17}$$

respectively. Here λ and μ are the second and first viscosity coefficients, respectively and k is the thermal conductivity. For a perfect gas with constant specific heats c_v and c_p, we have the following relations

$$e = c_v T \tag{2.18}$$

and

$$p = \rho R T \tag{2.19}$$

For compressible flows, the Favre-filtered (density-weighted-filtered) field, which is defined in an analogous manner to the Favre time average, is introduced (Erlebacher *et al.* 1992).

$$\tilde{f} = \frac{\overline{\rho f}}{\overline{\rho}} \tag{2.20}$$

The total flow field may be decomposed into a resolvable field and a subgrid-scale field,

$$f = \tilde{f} + f' \tag{2.21}$$

Note that, when density is not constant,

$$\tilde{\bar{f}} \neq \tilde{f} \quad \text{and} \quad \tilde{f}' \neq 0 \tag{2.22}$$

even when sharp cut-off filter is used.

Filtering the mass and momentum equations, we obtain

$$\frac{\partial \overline{\rho}}{\partial t} + \frac{\partial (\overline{\rho} \tilde{u}_j)}{\partial x_j} = 0 \tag{2.23}$$

$$\frac{\partial \overline{\rho} \tilde{u}_i}{\partial t} + \frac{\partial}{\partial x_j}[\overline{\rho} \tilde{u}_i \tilde{u}_j + \overline{p} \delta_{ij} + R_{ij} + L_{ij} + C_{ij} - \overline{\tau}_{ji}] = 0 \tag{2.24}$$

where

$$R_{ij} = \rho \widetilde{u_i' u_j'} \tag{2.25}$$

$$L_{ij} = \overline{\rho}(\widetilde{\tilde{u}_i \tilde{u}_j} - \tilde{u}_i \tilde{u}_j) \tag{2.26}$$

$$C_{ij} = \overline{\rho}(\widetilde{\tilde{u}_i u_j'} + \widetilde{\tilde{u}_j u_i'}) \tag{2.27}$$

are referred to as the Reynolds-stress, Leonard-stress, and cross-stress terms. The filtered pressure is given by

$$\overline{p} = \overline{\rho} R \tilde{T} \tag{2.28}$$

Filtering the equation for total energy, we obtain

$$\frac{\partial (\overline{\rho} \tilde{E} + q)}{\partial t} + \frac{\partial}{\partial x_j}[(\overline{\rho} \tilde{E} + \overline{p}) \tilde{u}_j + K_j + Q_j - \overline{u_i \tau_{ij}} + \overline{q_j}] = 0 \tag{2.29}$$

where

$$\tilde{E} = \tilde{e} + \frac{1}{2} \tilde{u}_i \tilde{u}_i \tag{2.30}$$

$$q = \frac{1}{2}(R_{kk} + L_{kk} + C_{kk}) \tag{2.31}$$

$$K_j = \frac{1}{2}\overline{\rho}(\widetilde{\tilde{u}_i\tilde{u}_i\tilde{u}_j} - \tilde{u}_i\tilde{u}_i\tilde{u}_j + \widetilde{u_i'u_i'\tilde{u}_j} + \widetilde{\tilde{u}_i u_j'} + \widetilde{u_i'u_i'u_j'} + 2\widetilde{u_i'\tilde{u}_i}\tilde{u}_j + 2\widetilde{u_i'\tilde{u}_i u_j'}) \tag{2.32}$$

$$Q_j = c_p\overline{\rho}(\widetilde{T'u_j'} + \widetilde{\tilde{T}\tilde{u}_j} - \tilde{T}\tilde{u}_j + \widetilde{T'\tilde{u}_j} + \widetilde{\tilde{T}u_j'}) \tag{2.33}$$

2.2.3 Subgrid-scale model

The filtering of nonlinear terms in the Navier-Stokes equations produces terms that can not be computed directly from the resolved field. The effect of these subgrid terms has to be accounted for by some kind of turbulence model.

Most commonly used model of R_{ij} is an extension of eddy viscosity model. For incompressible flow, the Reynolds stress term, $\overline{u_i'u_j'}$, can be modeled as:

$$\overline{u_i'u_j'} = \nu_T\frac{1}{2}(\frac{\partial\overline{u_i}}{\partial x_j} + \frac{\partial\overline{u_j}}{\partial x_i}) = \nu_T\overline{S}_{ij} \tag{2.34}$$

Two choices of ν_T are

$$\nu_T = c\Delta^2(\overline{S}_{ij}\overline{S}_{ij})^{\frac{1}{2}} \tag{2.35}$$

or

$$\nu_T = c\Delta^2(\overline{\omega}_i\overline{\omega}_i)^{\frac{1}{2}} \tag{2.36}$$

where S_{ij} is the strain rate tensor and c is the model constant (Ferziger 1977).

Equation (2.35) is due to Smagorinsky (1963) and is based on the balance of local shear production and local dissipation. The second one, based on dimensional analysis, has the useful property of being zero in irrotational regions but lacks the physical foundation of Smagorinsky's model.

In equations (2.35) and (2.36), Δ is of the same order as the filter widths (or the smallest resolved scales). When the same filter with equal filter width is used in all directions, the filter width, Δ_f, is a natural choice for Δ. However, except in

the simulation of homogeneous turbulence, we generally use different filter widths as well as different filter functions in three directions. A definition of Δ that can represent the average of the three filter widths is needed.

Two common definitions of Δ are

$$\Delta = (\Delta_x \Delta_y \Delta_z)^{\frac{1}{3}} \tag{2.37}$$

and

$$\Delta^2 = \frac{(\Delta_x{}^2 + \Delta_y{}^2 + \Delta_z{}^2)}{3} \tag{2.38}$$

where Δ_x, Δ_y, and Δ_z are the filter widths in the three orthogonal directions.

Erlebacher *et al.* (1992) extends the incompressible model to compressible flows

$$R_{ij} = -2C_R\Delta^2\overline{\rho}\sqrt{\Pi}(\widetilde{S_{ij}} - \frac{1}{3}\widetilde{S_{kk}}\delta_{ij}) + \frac{2}{3}C_I\Delta^2\overline{\rho}\Pi\delta_{ij} \tag{2.39}$$

where

$$\widetilde{S_{ij}} = \frac{1}{2}(\frac{\partial\tilde{u}_i}{\partial x_j} + \frac{\partial\tilde{u}_j}{\partial x_i}) \tag{2.40}$$

is the rate of strain tensor of the resolvable field, and

$$\Pi = \widetilde{S_{ij}}\widetilde{S_{ij}} \tag{2.41}$$

The cross stress term is modeled with the scale similarity model

$$C_{ij} = \overline{\rho}(\tilde{u}_i\tilde{u}_j - \tilde{\tilde{u}}_i\tilde{\tilde{u}}_j) \tag{2.42},$$

which is analogous to its incompressible counterpart suggested by Bardina *et al.* (1983). This model can be regarded as an attempt to extrapolate the computed large-scale field to get information in subgrid scale motions.

Therefore, the sum of cross stress and Leonard stress terms can be written as

$$L_{ij} + C_{ij} = \overline{\rho}(\widetilde{\tilde{u}_i\tilde{u}_j} - \tilde{\tilde{u}}_i\tilde{\tilde{u}}_j) \tag{2.43}$$

The combination of equations (2.39) and (2.43) is referred as the linear combination model (LCM). Equation (2.43) can be computed directly by using the definition of the filtered variable if density is constant. In compressible flows, to calculate $C_{ij} + L_{ij}$, we need to know the value of unfiltered density. Since the distribution of density is much more smooth than velocity components in subsonic flows, we expect the difference between filtered and unfiltered values of of density to be very small. Hence, the use of filtered density in the calculation of $L_{ij} + C_{ij}$ should be acceptable.

In the energy equation, the temperature-velocity correlation terms are modeled by a gradient-transport model:

$$\widetilde{T'u_j'} = -C_T \Delta^2 \sqrt{\Pi} \frac{\partial \tilde{T}}{\partial x_j} \tag{2.44}$$

and the scale similarity model produce:

$$\widetilde{T'\tilde{u}_j} + \widetilde{\tilde{T}u_j'} = \tilde{T}\tilde{u} - \tilde{\tilde{T}}\tilde{\tilde{u}}_j \tag{2.45}$$

Substituting Eqs(2.44) and (2.45) into Eq(2.33), we obtain

$$Q_j = c_p \bar{\rho}(-C_T \Delta^2 \sqrt{\Pi} \frac{\partial \tilde{T}}{\partial x_j} + \widetilde{\tilde{T}\tilde{u}_j} - \tilde{\tilde{T}}\tilde{\tilde{u}}_j) \tag{2.46}$$

where the constant C_T is written as

$$C_T = \frac{C_R}{Pr_T} \tag{2.47}$$

Pr_T is a turbulent Prandtl number.

In this work, the total energy is chosen as the primitive variable in energy equation to avoid the modeling of temperature dilatation correlation (Erlebacher *et al.* 1990). This choice leads to the appearance of K_j, for which no model is available yet. The first two terms can be computed directly. The third and last terms may be modeled by Smagorinsky model with the following approximation (Ragab *et al.* 1992)

$$\tilde{u}_i \widetilde{u_j' u_k'} \approx \widetilde{u_j' u_k'} \tilde{u}_i \tag{2.48}$$

Scale similarity model may be used for the remaining terms when similar approximation is made.

Model constants

Erlebacher *et al.* (1992) attempted to obtain the subgrid model constant, C_R, by correlating the results of direct numerical simulations of compressible isotropic turbulence using spectral methods. Two different methods are used in their work to calculate the constant. And the constant obtained by the two different methods differ by about a factor of two. It is also likely that the constant would be different if the flow data at different Reynolds numbers is used. In addition, the model is based on the balance of local shear production and dissipation of fully developed turbulent flow, a fixed model constant will not be able to produce accurate predictions of subgrid-scale dissipation in the laminar/turbulent transition region. To overcome these deficiencies, Germano *et al.* (1991) developed a dynamic subgrid-scale model with model constants that are functions of space and time. The model uses the strain rate at two different scales and thus utilizes spectral information in the large-scale field to extrapolate the small-scale stress.

More sophisticated turbulence model

In the research of atmospheric boundary layer, the filter width is so large that a very large fraction of the total transport of important quantities is carried by the subgrid scale turbulence, and the eddy viscosity model is found to be insufficient (Deardorff 1973). Therefore, a higher level of modeling, which uses dynamic equations for the Reynolds stresses or any other quantities that appear in the governing equations, may become necessary. In this approach, these dynamic equations will contain higher-order correlation terms, which still need some kind of modeling or another set of even higher-level dynamics equations.

3. NUMERICAL METHODS

3.1 Computational Domain and Boundary Conditions

Throughout this work, (x, y, z) are used to denote the streamwise, transverse, and spanwise coordinates respectively. The computation box is shown in figure 3.1.

3.1.1 Spatially and temporally developing mixing layers

Two different types of mixing layer problems can be solved numerically. The spatially developing mixing layer uses the same reference frame as the experiments, with inflow boundary at one end of the computational box and outflow boundary at the other. Given the convective nature of the instability waves, the mixing layer will be dominated by the upstream disturbances, which are specified as a function of time in numerical simulation. The outflow boundary conditions should avoid any reflection back into the simulation. Although this approach is physically realistic, a large computational box is needed to see significant development of the mixing layer. As noted in chapter 1, transition occurs during sequential vortex pairings. Therefore, to study turbulence transition using a spatially developing mixing layer will require a huge computational box in the transverse direction as well as in the streamwise direction because of the rapid growth of mixing layers during the pairing process.

An alternative that uses the computer resources more efficiently is to fix the com-

putational box in a reference frame moving with the velocity of the large structures. This approach may be thought of as an approximation to the evolution of a single set of flow structures as they are convected downstream in the spatially developing layer (Rogers and Moser 1991). The role of time and the streamwise spatial direction are thus reversed. The flow is assumed to be statistically homogeneous in planes parallel to the interface that separates the two streams. Hence, periodic boundary conditions can be applied in the two coordinate directions in these planes. In a mixing layer with convective Mach number in the low subsonic region, we expect the large structure to move with the mean velocity of the lower and upper streams. Therefore, the choice of the convective velocity will cause no difficulty. However, in the case of a mixing layer with convective Mach number in the supersonic range, the phase speed of the large structures will not necessarily equal the mean velocity. Use of the mean velocity as the convective velocity of the reference frame is questionable in the case of high convective Mach number.

3.1.2 Boundary conditions in the transverse direction

Far-field boundary conditions

When an unbounded mixing layer is considered, two different far-field boundary conditions can be used. The first one sets the derivatives of all variables in the transverse direction to be zero. For convective Mach numbers in the low subsonic range, this boundary condition works fine as long as the large structures in the mixing layer are well within the computational domain.

The second boundary condition uses the scheme of Thompson (1987). The basic idea is to consider the characteristic form of the Euler equations at the boundary. Outgoing characteristics use information within the computational domain, while time derivatives of incoming characteristics are set to zero to ensure that no wave enters the domain during the simulation.

For a mixing layer with low convective Mach number (M^+ =0.4), no substantial difference is found between these two treatments of boundary conditions as long as the computation box is large enough.

3.2 Governing Equations

3.2.1 Non-dimensionalization

Non-dimensionalization of the governing equations is obtained by using as the reference state the upper freestream properties, which are denoted by subscript 1.

In the following sections, asterisk is used to represent the dimensional variables and the dimensionless variables are defined as

$$\begin{aligned}
(x, y, z) &= \frac{(x^*, y^*, z^*)}{L^*} \\
u_i &= \frac{u_i^*}{U_1^*} \\
\rho &= \frac{\rho^*}{\rho_1^*} \\
T &= \frac{T^*}{T_1^*} \\
P &= \frac{P^*}{\rho_1^* {U_1^*}^2} \\
E &= \frac{E^*}{{U_1^*}^2} \\
\mu &= \frac{\mu^*}{\mu_1^*}
\end{aligned} \tag{3.1}$$

The upper free-stream velocity, U_1^*, is chosen as the reference velocity. The reference length L^* is one half of the vorticity thickness of the mean velocity profile, which is a hyperbolic tangent function. The vorticity thickness is defined as

$$\delta_\omega^* = \frac{U_{max}^* - U_{min}^*}{(dU^*/dy^*)_{max}} \tag{3.2}$$

where U^* the streamwise velocity component averaged over the $x - z$ plane. In temporal simulation $U_1^* = -U_2^*$. The equation of state has the dimensionless form

$$P = \frac{\rho T}{\gamma {M_1}^2} \tag{3.3}$$

if perfect gas assumption is used, where M_1 is the upper freestream Mach number and γ is the specific heat ratio, for which the value of 1.4 is used.

The definition of specific total energy,

$$E^* = C_v T^* + \frac{1}{2}(u_1^{*2} + u_2^{*2} + u_3^{*2}), \tag{3.4}$$

has the nondimensional form of

$$E = T\frac{1}{(\gamma - 1)\gamma M_1{}^2} + \frac{1}{2}(u_1^2 + u_2^2 + u_3^2). \tag{3.5}$$

3.2.2 Governing equations of LES

In LES of temporally developing mixing layers, the molecular viscous and conduction terms are neglected because there exists no solid boundary. The dimensionless governing equations have the same forms as those described in Chapter 2 (Equations 2.23, 2.24, 2.29, 2.39, 2.43, 2.44, 2.45, 2.47), except for Q_j in Equation (2.46), which, in dimensionless form, is rewritten as

$$Q_j = \frac{1}{(\gamma - 1)M_1^2}(-C_T\Delta^2\sqrt{\Pi}\frac{\partial \tilde{T}}{\partial x_j} + \widetilde{\tilde{T}\tilde{u}_j} - \tilde{\tilde{T}}\tilde{\tilde{u}}_j) \tag{3.6}$$

3.3 Numerical Schemes

This section presents the formulation of numerical schemes that are used in this work. The first one is a modified MacCormack scheme, which is fourth-order accurate in space and second-order in time. The major advantages of this scheme are its built-in artificial dissipation and its simple algorithm, which facilitates vectorization. All other schemes that are discussed in this section use the Runge-Kutta time advancement method and the same finite-difference form for the turbulence model. The methods used to evaluate the convective terms include a third-order flux-difference-splitting scheme, fourth-order central difference, sixth-order Pade scheme, and a pseudo-spectral scheme. Since the Runge-Kutta scheme supplies little dissipation itself, additional dissipation is needed. Except for the flux-splitting scheme, which has substantial numerical dissipation, the other three need special treatment to eliminate the aliasing errors. In addition, even the simplest central-difference form is slower than the MacCormack scheme.

3.3.1 MacCormack (2,4) scheme

This is a modified MacCormack scheme developed by Gottlieb and Turkel (1976) and used in boundary layer research by Bayliss *et al.* (1986).

The scheme is explicit second-order accurate in time and fourth-order in space. For the one dimensional equation $q_t + f_x = 0$, the predictor step is

$$\overline{q_j} = {q_j}^n - \frac{\Delta t}{6\Delta x}[7(f_{j+1} - f_j) - (f_{j+2} - f_{j+1})] \tag{3.7}$$

and the corrector step is

$${q_j}^{n+1} = \frac{1}{2}({q_j}^n + \overline{q_j}) - \frac{\Delta t}{12\Delta x}[7(\overline{f}_j - \overline{f}_{j-1}) - (\overline{f}_{j-1} - \overline{f}_{j-2})] \tag{3.8}$$

In operator form the two steps (3.7) and (3.8) can be written as

$$q^{n+1} = {L_x}^{FB} q^n \tag{3.9}$$

the FB superscript refers to forward predictor (3.7) and backward corrector (3.8). There is an alternate version which employs a forward predictor and a backward corrector. We denote such a scheme by ${L_x}^{BF}$. For multidimensional equations, operator splitting technique (Strang 1968) is used. Discretization in three dimensions is achieved by using one dimensional operators in a symmetrical fashion. Following Ragab *et al.* (1992), we use

$$q^{n+4} = L_x^- L_y^- L_z^- L_z^+ L_y^+ L_x^+ q^n \tag{3.10}$$

where

$$L_x^- = {L_x}^{BF} {L_x}^{FB} \tag{3.11}$$

$$L_x^+ = {L_x}^{FB} {L_x}^{BF} \tag{3.12}$$

with similar definitions for the y and z operators.

The implementation of this scheme is straightforward if the flux function f contains no derivative. To include the viscous term, the approach of Gottlieb and Turkel (1976) is used. For a forward sweep, the first order derivative in the same direction

is evaluated by a two-point backward difference, i.e., $U_{x,i} = \frac{U_i - U_{i-1}}{\Delta x}$ and conversely for the backward sweep. For the derivative in the direction normal to the sweep, second order central difference is used.

Boundary point treatment

Consider the forward predictor, for example. If $i = N$ denotes a boundary point, then the values of flux vector are not available at $i = N + 1$ and, thus, the scheme cannot be applied at the point $i = N - 1$. In this work a third order extrapolation (Bayliss *et al.* 1986) is used to get the flux values at $i = N + 1$ so that the scheme can be applied up to $i = N - 1$. The f_{N+1} is defined as

$$f_{N+1} = 4f_N - 6f_{N-1} + 4f_{N-2} - f_{N-3} \tag{3.13}$$

Similarly for backward predictor or corrector,

$$f_0 = 4f_1 - 6f_2 + 4f_3 - f_4 \tag{3.14}$$

if $i = 1$ is the boundary point on the other end.

3.3.2 Runge-Kutta time advancement schemes

A. Second-order three-stage

The time integration can be summarized as follows (Hirsch 1990).

$$\begin{aligned} q^0 &= q^n \\ q^1 &= q^n - \alpha_1 \Delta t R(q^0) \\ q^2 &= q^n - \alpha_2 \Delta t R(q^1) \\ q^3 &= q^n - \alpha_3 \Delta t R(q^2) \\ q^{n+1} &= q^3 \end{aligned} \tag{3.15}$$

where R is the residual of the governing equations. The values of αs are $\alpha_1 = 1/3, \alpha_2 = 1/2, \alpha_3 = 1$.

B. Low storage third-order Runge-Kutta

This scheme is due to Wray (1986). It uses two storage spaces for each variable. Assume the two storage space are X and Y respectively. For each time step, three evaluations of residual are involved. The procedure for one complete time step is summarized as follows:

$$\begin{aligned} X &= q^n \quad ; \quad Y = R(X) \\ X &= X + a\Delta t Y \quad ; \quad Y = X + (A-a)\Delta t Y \\ X &= X \quad ; \quad Y = R(Y) \\ X &= X + b\Delta t Y \quad ; \quad Y = X + (B-b)\Delta t Y \\ X &= X \quad ; \quad Y = R(Y) \\ q^{n+1} &= X + c\Delta t Y \end{aligned} \tag{3.16}$$

To obtain the third-order accuracy, the following equations have to be satisfied

$$\begin{aligned} a + b + c &= 1 \\ (a+B)c + Ab &= 1/2 \\ (a+B)^2 c + A^2 b &= 1/3 \\ ABc &= 1/6 \end{aligned} \tag{3.17}$$

There are four equations for five unknowns. To solve this set of equations, we need one additional equation, which is chosen to be

$$B = b \tag{3.18}$$

This condition will enable us to use only two storage spaces for each variable when R is of finite difference form. When we go back to the Wray's algorithm in (3.16), we notice that using two storage spaces for each variable can be realized only when the residual function, $R(X)$ can be decided solely by the value of local X, otherwise the value of R in the second stage (third equation in (3.16)) will replace the content of space Y, which will influence the residual at the neighboring points. This problem can be solved by using the same value for B and b. Thus, in the second evaluation of R, the value of R is multiplied by $b\Delta t$ and add to X to replace X, while the values of Y is kept intact until this stage finishes. At the end of this stage (third and fourth equations in (3.16)), X and Y have the same contents. One of the two spaces is used to store the residual, while the other is reserved for data from second stage, which can not be replaced until the end of this stage.

The additional equation, $B = b$, combined with equation (3.17) gives

$$6c^3 - 6c^2 + 3c - 1 = 0 \tag{3.19}$$

The real root is

$$c = \frac{1}{3} + \left(\frac{1}{27} + \frac{1}{18\sqrt{2}}\right)^{\frac{1}{3}} - \left(-\frac{1}{27} + \frac{1}{18\sqrt{2}}\right)^{\frac{1}{3}} \tag{3.20}$$

The other four coefficients are

$$\begin{aligned} A &= c\left(2 - 6(1-c)^2 c\right) \\ b = B &= \frac{1}{6Ac} \\ a &= 1 - b - c \end{aligned} \tag{3.21}$$

3.3.3 Evaluation of spatial derivatives

A. Fourth-order central difference

A derivative $\left(\frac{\partial \phi}{\partial x}\right)$ at node i is evaluated by

$$\phi_i' = \frac{8(\phi_{i+1} - \phi_{i-1}) - (\phi_{i+2} - \phi_{i-2})}{12\Delta x} \tag{3.22}$$

which is used for the convective terms.

B. Modified Pade scheme

A family of high order modified Pade schemes has been derived by Lele (1989). The first derivatives can be obtained by solving the following tridiagonal system:

$$\phi_{j-1}' + a\phi_j' + \phi_{j+1}' = b\,\frac{\phi_{j+1} - \phi_{j-1}}{2\Delta y} + c\,\frac{\phi_{j+2} - \phi_{j-2}}{4\Delta y} \tag{3.23}$$

using available boundary conditions.

A family of fourth order schemes is obtained if

$$b = \frac{2 + 4a}{3} \quad \text{and} \quad c = \frac{4 - a}{3} \tag{3.24}$$

For a=3, the fourth order error will vanish and we have a sixth order scheme, which will be used for evaluating the derivatives of the convective terms in the transverse direction.

C. Spectral differentiation

In temporal simulation, the periodic boundary conditions are used in streamwise and spanwise directions. Thus the spatial derivatives in these two directions can be easily evaluated using Fourier series.

Removal of aliasing errors

In this work, the Fourier collocation method, also called pseudo-spectral method, is used to compute the convective terms. The collocation method calculates products in the nonlinear terms in the physical space. Then the Fourier coefficients of the product are obtained using the fast Fourier transform algorithm. This approach is more efficient than computing the product directly in the Fourier space (Galerkin method), especially for cubic, or even higher order, nonlinear terms which appear in the governing equations for the compressible flows. The disadvantage of the collocation method is the accumulation of aliasing errors near the highest resolvable wavenumber. Aliasing error happens during the calculation of product in the physical space. The multiplication produces Fourier components unresolvable by the grid system. In the following discrete Fourier transform, those high wavenumber components will alias to lower wavenumbers. The effect of aliasing errors is most apparent near the tail of the spectrum (the highest resolvable wavenumber), although they affect all the components in the Fourier space. In finite-difference schemes, the aliasing errors can be controlled by added dissipation (explicit artificial dissipation or implicit dissipation from numerical scheme like upwind finite difference). For the pseudo- spectral method, the most popular dealiasing method is the $\frac{3}{2}$ rule (Canuto *et al.* 1988). The $\frac{3}{2}$ rule can be implemented by locally refining the grid along the direction of differentiation using Fourier interpolation. The alternative approach is to eliminate one-third of highest Fourier modes of each variable.

D. Flux-difference splitting

In this method convective terms are handled using flux difference splitting techniques involving Roe's approximate Reimann solver (Roe 1981). For computing fluxes on the cell faces, the following third-order interpolation formulae are used (Hirsch 1990).

$$U^L{}_{i+1/2} = U_i + \frac{\epsilon}{4}[(1-k)(U_i - U_{i-1}) + (1+k)(U_{i+1} - U_i)] \tag{3.25}$$

$$U^R{}_{i+1/2} = U_{i+1} + \frac{\epsilon}{4}[(1+k)(U_{i+1} - U_i) + (1-k)(U_{i+2} - U_{i+1})] \tag{3.26}$$

where $\epsilon = 1$ and $k = 1/3$.

The approximate Riemann solver is then used to calculate the the flux at $i + \frac{1}{2}$ by assuming a contact discontinuity formed by the two states $U^L{}_{i+1/2}$ and $U^R{}_{i+1/2}$. at the interface. And the value of $\frac{\partial f}{\partial x}$ is obtained by

$$\frac{\partial f}{\partial x} = \frac{f_{i+1/2} - f_{i-1/2}}{\Delta x} \tag{3.27}$$

E. Viscous terms

The viscous terms (molecular and turbulence model) will be evaluated using second order central difference in which first order derivatives will be calculated at the center face between grid points. For example,

$$\left(\frac{\partial \tau_{xy}}{\partial x}\right)_{ij} = \frac{\tau_{xy,(i+\frac{1}{2},j)} - \tau_{xy,(i-\frac{1}{2},j)}}{\Delta x} \tag{3.28}$$

In $\tau_{xy,(i+1/2,j)}$, the average of values at i and $i+1$ will be used for the zeroth terms, while the derivative in x direction will be computed by

$$\left(\frac{\partial \phi}{\partial x}\right)_{i+\frac{1}{2},j} = \frac{\phi_{i+1,j} - \phi_{i,j}}{\Delta x}, \tag{3.29}$$

The derivative in y direction will be evaluated by the following way

$$\left(\frac{\partial \phi}{\partial y}\right)_{i+\frac{1}{2},j} = \frac{(\phi_{i+1,j+1} + \phi_{i,j+1}) - (\phi_{i+1,j-1} + \phi_{i,j-1})}{4\Delta y} \tag{3.30}$$

The extension to other terms is straightforward.

3.4 Initial Conditions and Random Flow Field

The mean velocity in the streamwise direction is given by a hyperbolic tangent function:

$$U(y) = \left(\frac{U_1 + U_2}{2}\right) + \left(\frac{U_1 - U_2}{2}\right) tanh\,(y) \tag{3.31}$$

The mean temperature is obtained from the mean velocity profile via the Crocco-Busemann relation (Schlitching 1979), which assumes parallel flow and unit Prandtl number.

$$T^* = -\frac{u^{*2}}{2c_p} + C_1 u^* + C_2 \tag{3.32}$$

The constants of C_1 and C_2 can be obtained by using the boundary conditions

$$\begin{cases} T = 1 & \text{when} \quad u = 1 \\ T = T_2 & \text{when} \quad u = U_2 \end{cases} \tag{3.33}$$

when U_1^* and T_1^* are chosen as the reference state. We thus obtain the following dimensionless relation

$$T = M_1^2 \frac{(\gamma - 1)}{2} (u(1 + U_2) - u^2 - U_2) + \frac{T_2(1 - u)}{(1 - U_2)} + \frac{(u - U_2)}{(1 - U_2)} \tag{3.34}$$

The mean pressure is assumed to be uniform, and then density can be obtained by using the equation of state.

Perturbation added to the mean profiles include eigenfunctions from linear stability analysis (Ragab and Wu 1988, 1989) and/or a random velocity field.

Eigenfunctions of linear stability analysis

The eigenfunctions of unstable modes of linear stability analysis are obtained by the code developed by Ragab and Wu (Wu 1989). The eigenfunctions are superimposed onto the mean flow with an adequate amplitude. For example, for streamwise velocity component, the disturbance of a certain mode can be written as

$$u'_{(\alpha\beta)} = \sqrt{2} A_{rms} \text{Real} \left\{ \hat{u}_{\alpha,\beta}(y) e^{i(\alpha x + \phi)} cos(\beta z) \right\} \tag{3.35}$$

and similarly for transverse velocity component, density, and temperature, except for the spanwise velocity, for which $cos(\beta z)$ is replaced by $i\,sin(\beta z)$. Where α and

β are the corresponding wave numbers of this eigenfunction in the streamwise and spanwise directions, respectively, and ϕ is the phase. $\hat{u}$ is normalized such that $\mid \hat{u} \mid_{max} = 1$

Random disturbance

Next we summarize the procedure of generating a random divergence-free velocity field with a specified 3-D energy spectrum (Maruyama 1988).

1. A random number generator is used to produce a random vector field, Φ, in the physical space.

2. By taking the curl of Φ, we will get a random divergence-free vector field. To make this vector field have the specified spectrum, we have to rescale the Fourier modes of Φ first.

The modal energy of a certain Fourier mode (l, m, n) is defined as

$$E_{lmn} = \frac{1}{2}(\hat{u}_{lmn}\hat{u}^*_{lmn} + \hat{v}_{lmn}\hat{v}^*_{lmn} + \hat{w}_{lmn}\hat{w}^*_{lmn}) \tag{3.36}$$

where l, m, and n are the mode number in the three directions, respectively and $\hat{}$ denote the Fourier transform of the variable. The asterisks represent the corresponding complex conjugate.

Next we may devide the Fourier space into shells with equal thickness and then sum up the energy of all the Fourier modes in each shell. By comparing the calculated spectrum with the specified one, we can rescale the Fourier modes of Φ with the square root of the ratio of specified values to the calculated ones in each shell. The velocity field can be obtained by taking the curl of Φ in either physical or Fourier space.

To make the disturbance decay at $y = \pm\infty$, we may multiply this velocity by a function $f(y)$, which decays in $\pm y$ directions. This procedure, of course, will destroy the divergence-free property. An alternative is to multiply Φ by $f(y)$ in physical space before its Fourier modes are rescaled. The process of rescaling will certainly

influence the distribution in y direction, but experience shows that the decaying property of $f(y)$ can be largely maintained.

The pressure disturbance is calculated by solving the Poisson equation

$$\nabla^2 p = -\frac{\partial u_j}{\partial x_i}\frac{\partial u_i}{\partial x_j} \tag{3.37}$$

Assuming no density disturbance, we can obtain the temperature disturbance by using the equation of state.

4. TWO-DIMENSIONAL SIMULATIONS

The objective of this chapter is to study the evolution of 2-D vortical structures in a near incompressible mixing layer. Although two-dimensional simulations are used in different kinds of turbulent flows, especially in meteorology, their applications to the mixing layers should be carefully examined, because the vortex stretching mechanism, which is found to be a major source for the generation of small-scale motions (chapter 6), does not exist in two-dimensional simulations. However, the two-dimensional simulations are capable of producing large structures very similar to those observed in experiments (Lele 1989, Sandham and Reynolds 1989) when the organized three-dimensional flows are not too strong. The cases with strong 3-D secondary vortex flows will be discussed in chapter 6.

The simulated case is a temporally developing mixing layer. The convective Mach number is 0.4, at which the primary stability analysis produces results similar to those in an incompressible mixing layer. The flow field is initialized by the mean components and a divergence-free random velocity field. No density or pressure disturbances are used. According to the linear stability theory, the most amplified 2D wave has a wavenumber of 0.4, hence the corresponding wavelength is 5π. The reference length is one-half of the vorticity thickness of the unperturbed mixing layer. The size of the computational box is chosen to be four times the most amplified wave-length (20 π) in the streamwise direction to show two pairing processes. In the transverse direction, y extends from -30 to 30. A uniform grid of (257,301) points is used.

A Fourier analysis in the x-direction is performed at selected times, and the modal energy, defined as

$$E_k(t) = \int_{ymin}^{ymax} (\hat{u}\hat{u}^* + \hat{v}\hat{v}^*)_k dy \tag{4.1}$$

is computed. Here k is the mode number. Mode k represents the wave with wavelength equal to one-kth of the streamwise size of the computational box. Since the computational box contains four most amplified wavelengths in the streamwise direction, $k = 4$ represents the fundamental mode, while $k = 2$ and $k = 1$ are its first and second subharmonics respectively. The development of E_k is shown in Fig. 4.1. The reference time is is based on the reference length and velocity, which is the upper free-stream velocity. Figure 4.1a shows the initial modal energy of the random velocity field. Spectra at another three selected times are also shown. Note the shift of peak from mode 4 to mode 2 and then to mode 1 in Figs. 4.1b, c, and d. This represents the three stages in the evolution of this mixing layer, the formations of Kelvin-Helmholtz vortices, the first pairing, and the second pairing. Also note the slope of -4 of the spectrum curve. This slope is also observed in the numerical simulation of an incompressible temporally developing mixing layer (Lesieur *et al.* 1988). The DNS results of Herring and McWilliams (1985) on "2-D homogeneous turbulence" also show similar slope. The vorticity contours at the three different times are shown in Fig. 4.2. The formation of spanwise vortices and the two pairing processes can be clearly seen.

5. CONTROL OF LARGE-SCALE STRUCTURES USING LINEAR STABILITY EIGENFUNCTIONS

5.1 Introduction

Mixing at the molecular level, which is extremely important for chemically reacting flows, is influenced by the large-scale structures through the entrainment process as well as by the production of small-scale turbulent motions. Hence, knowledge of the generation of large structures is vital in any attempt to control mixing and combustion in a mixing layer. Nygaard and Glezer (1991) used imbedded heating strips in the splitter plate to produce desired structures. Their experiments show that this technique can control both the frequency and phase of the upstream disturbances.

The purpose of this chapter is to analyze and predict the effect of the eigenfunctions from linear stability analysis and their relative phases on the development of a mixing layer. This analysis can provide useful information in choosing adequate initial conditions to produce the desired structures in the numerical simulation of a temporally developing mixing layer.

In a subsonic mixing layer, the primary vortex structure is the spanwise vortices evolving from the Kelvin-Helmholtz (K-H) instability. The two major secondary structures are the pairing (2-D or helical) of the K-H vortices, and the formation of streamwise vortex tubes. By initializing the numerical simulation with linear

stability eigenfunctions of adequate amplitudes and phases, we are able to control the development of these basic structures in a mixing layer.

The analysis presented in this chapter is for a temporally developing mixing layer with a convective Mach number of 0.4. The reference length is one-half of the vorticity thickness of the unperturbed mixing layer and the reference velocity is the upper free-streamw velocity. The most amplified 2-D wave, according to the linear stability analysis, has a wavenumber $\alpha = 0.4$, hence the wavelength is $2\pi/0.4$. The computational box for the simulations in this chapter as well as the following chapters is chosen to accommodate two most amplified waves in the x direction, i.e., $L_x = 2\pi/0.2$. The length of the box in the spanwise direction, L_z, is also of the same dimension. In the following discussion, the mode (m, n) is used to denote a wave with streamwise wavelength of L_x/m and spanwise wavelength of L_z/n. Therefore, the (2, 0) mode is the most amplified 2-D wave of linear stability analysis and the (1, 0) mode is its first subharmonic.

5.2 Major Vortex Structures in a Mixing Layer

Formation of spanwise vortices

Shown in Fig. 5.1 are the contours of spanwise vorticity (ω_z) and transverse velocity (v) of the (2, 0) mode. These perturbations are obtained by equation (3.35), which is repeated here.

$$u'_{(\alpha\beta)} = \sqrt{2} A_{rms} \text{Real}\left\{\hat{u}_{\alpha,\beta}(y) e^{i(\alpha x+\phi)} cos(\beta z)\right\} \tag{3.35}$$

The equation shows that the use of phase ϕ will shift the disturbance field by ϕ/α in the negative streamwise direction. The thick line represent negative values (as with all other contour plots in this section). The formation of the spanwise vortices is explained by the sketches in Fig. 5.2. The wavy line represents the interface, which is also the location with maximum vorticity in the unperturbed mixing layer. The vertical arrows mark the locations and directions of the maximum $v-$component of the (2, 0) mode (see Fig. 5.1). These perturbations cause the undulation of the interface and form two vortices at $x = \frac{3}{8}L_x$ and $x = \frac{7}{8}L_x$.

For visualization purpose, the centers of the two vortices will be moved to $\frac{1}{4}L_x$ and $\frac{3}{4}L_x$ to show complete vortices inside the computational box. This requires a shift of $\frac{1}{8}L_x$ in length or $\pi/2$ in phase. This phase change is used throughout this work.

Pairing of the spanwise vortices

Shown in Fig. 5.3 are the contours of spanwise vorticity and transverse velocity component of the (1, 0) mode, which is used to excite the 2-D pairing mode of the spanwise vortices. At $y = 0$, the maximum values of v happen at $x = 0$ and $\frac{1}{2}L_x$ with opposite signs. The strongest pairing effect can be obtained by locating the maximum v-perturbations of the (1, 0) mode at the centers of the spanwise vortices of the (2, 0) mode. If the phase of the (2, 0) mode is $\pi/2$, the phase of the (1, 0) mode can be chosen as $\pi/2$, which is equivalent to a shift of $\frac{1}{4}L_x$ in the streamwise direction. This is a phase difference of $3\pi/2$ for the two modes. In this case, the K-H vortex at $\frac{1}{4}L_x$ will be moved upward and then to the right by the upper-stream flow, while the vortex at $\frac{3}{4}L_x$ will be moved downward and to the left. Thus, the merged vortex will be located at $x = \frac{1}{2}L_x$.

The so-called helical pairing mode (Pierrehumbert and Widnall 1982) can be obtained by choosing adequate phases for the (1 , m) modes, where m is a non-zero integer. These modes have similar velocity perturbation contours to those of the (1, 0) mode in the $x - y$ plane at $z = 0$. Therefore, the same phase as the (1, 0) mode should be used. The periodicity in the spanwise direction makes the v component change sign along the span of the K-H vortices and the pairing is expected to alternate between $x = \frac{1}{2}L_x$ and $x = L_x$ along the span. This analysis is based on perturbations with small amplitudes. As the perturbations grow well into the nonlinear range, the behavior of these instability modes may be very different from what linear theory predicts. In fact, the simulation of the helical pairing mode performed by Sandham and Reynolds (1989) shows no sign of pairing. The incompressible secondary stability analysis (Pierrehumbert and Widnall 1982) shows that the growth rate of the helical pairing mode increases with the spanwise wavelength and reaches the asymptotic value as the spanwise wavenumber approaches zero (2-D pairing). These results of stability analysis and numerical simulation show that helical pairing is unlikely to happen at low spanwise wavelength.

For the (1, 0) mode, a small deviation from the optimum phase, $\pi/2$ (or a phase difference of $3\pi/2$) will still induce pairing, but at a slower pace. The effect of phase is discussed by Riley and Metcalfe (1980). They tested three different phases, 0, $\pi/2$, and π, which correspond to phases of $\pi/2$, $\pi/4$, and 0 for the (1, 0) mode in equation (3.35). The phase of 0 (or π) of the (1, 0) mode, will completely suppress pairing and move the vorticity of one of the K-H vortices to the other. The reason for this phenomenon is explained as follows:
When comparing the v-components of the (2, 0) and (1, 0) modes, we note that the perturbations of the (1, 0) mode, with contours similar to those of the (2, 0) (but different streamwise wavelength), is also able to produce its own K-H vortex just like the (2, 0) mode but with twice the size and lower growth rate (according linear stability analysis). When both modes are included in the initial disturbances and the phase of the (1, 0) mode is chosen to be π or 0, the center of the (1, 0) mode K-H vortex will coincide with that of one of the two (2, 0) mode vortices, while the other (2, 0) mode vortex will be located at the saddle point formed by the (1, 0) mode (see Fig. 5.3c). During the formation of the K-H vortex, the vorticity is moved from the braid region to the vortex center. Therefore, at this phase, the (1, 0) mode grows by extracting vorticity from one of the K-H vortices of the (2, 0) mode to supply the other.

Streamwise vortex tubes

Since the generation of streamwise vortex tubes in a mixing layer is caused by the strain rate field between the K-H vortices, to produce strong streamwise vortex tubes, the maximum streamwise and transverse vorticity perturbations should be located at the stagnation points (saddle points) formed by the adjoining K-H vortices. Figures 5.4a and 5.4b show the contours of ω_x and ω_y of the (2, 2) mode on the interface of the mixing layer ($x-z$ plane). The tic marks are at $\frac{1}{4}L_x$ increments. We notice that both vorticity components have maximum absolute values along the span at $x = 0$, $\frac{1}{4}L_x$, $\frac{1}{2}L_x$, $\frac{3}{4}L_x$, and L_x. Therefore, if the phase of the (2, 0) mode is chosen to be $\pi/2$, the stagnation points created by the primary spanwise vortices are formed at $\frac{1}{2}L_x$, and L_x (or 0) and no phase change has to be made for the (2, 2) mode. Another 3-D mode, the (1, 2) mode has similar contours (but

different streamwise wavelength) with maximum ω_x at $\frac{1}{2}L_x$, and L_x (or 0).

Another mechanism caused by the growth of the (2, 2) mode is the undulation of the K-H vortex tubes. In Fig. 5.4, we also notice that the (2, 2) mode has maximum streamwise vorticity perturbation along the K-H vortex tubes with a phase difference of π from the perturbations in the braid regions. These streamwise vorticity perturbations are compounded by the tilting of spanwise vorticity vectors of the K-H vortex cores. This process is explained in Fig. 5.5 by using the contours of the transverse velocity on the initial interface. Positive v-perturbation moves the K-H vortex core into the the upper stream and bend the vortex core in the positive x direction by the mean streamwise velocity component. A vortex line with the predicted distortion is shown with the contours. The arrows mark the positions and directions of the maximum streamwise vorticity perturbations (see Fig. 5.4a). It is clear that the v-perturbation of the (2, 2) mode enhances the streamwise vorticity in the K-H core through tilting of the spanwise vorticity.

5.3 Nonlinear Development of Stability Eigenfunctions

The purpose of this section is to study the development of different combinations of eigenfunctions and phases as they grow into the nonlinear region. A grid system with (55*129*55) points is used. All the simulations are initialized by eigenfunctions only, that is, no random disturbances are used.

The numerical simulations presented here are focused on the secondary structures. Thus, all initial disturbances include the (2, 0) mode. With its high growth rate, this mode will produce the dominant K-H vortex tubes in the early stage of evolution. The secondary structures will not show up until the (2, 0) mode saturates.

5.3.1 Phase of the (2, 2) mode

Pierrehumbert and Widnall (1982), in their secondary stability analysis, found two 3-D fundamental modes (the mode with same streamwise wavelength as the primary spanwise vortex), the bulging mode and the translative mode, in an incompressible

mixing layer. Their analysis shows substantial growth rate only for the translative mode. They did not speculate on the reason that causes the difference, nor did they provide enough information of the flow field of the two modes of analysis. Sandham and Reynolds (1989), using a different approach of stability analysis, which is similar to the one that generates eigenfunctions in this chapter, found that the same bulging and translative effects on the vortex cores can be produced by using adequate phases for their 3-D modes.

The effect of the phase of the (2, 2) mode is studied using three different initial conditions, all with same eigenfunctions, the (2, 0) and (2, 2) modes with amplitudes of 0.02, but different phases. The phase of (2, 0) is $\pi/2$. The three cases differ by the phase of the (2, 2) mode, for which three different values, 0, $\pi/4$, and $\pi/2$, are used. The phase of $\pi/2$ will leave no streamwise and transverse vorticity perturbations at the saddle points created by the K-H vortices. Thus, it has vortex core-bulging effect similar to the bulging mode of Pierrehumbert and Widnall (1982). The phase of 0 has the vortex core translative effect and produces maximum streamwise vorticity perturbations at the saddle points and the K-H vortex core.

The evolution of the following quantities are compared for the three different phases: momentum thickness, the modal energies of the (0, 0), (2, 0), (2, 2), and (0, 2) modes, and quantities representative of the amplitudes of velocity variations. The modal energy of a Fourier mode (m, n), $E_{mn}(t)$, is defined by

$$E_{mn}(t) = \int_{y_{min}}^{y_{max}} (\hat{u}\hat{u}^* + \hat{v}\hat{v}^* + \hat{w}\hat{w}^*)_{mn} dy \tag{5.1}$$

Where asterisk denotes the complex conjugate. The modal energy of the (0, 0) mode, E_{00}, will be shown as $E_{00}^o - E_{00}(t)$, where E_{00}^o is the initial value of E_{00}. Therefore, this value represents the energy lost by the mean flow to all other modes as well as the dissipation and the outflowing fluid. The variation of streamwise velocity component, u', is defined by

$$u' = \sqrt{\overline{(u - U(y))^2}} \tag{5.2}$$

with similar definition for v' and w', where overline denotes averaging over the domain from $y = -9.375$ to $y = 9.375$ and in the $x - z$ plane. $U(y)$ is u component averaged over the $x - z$ plane.

The modal energy, momentum thickness, and velocity variations are shown in Figs. 5.6, 5.7, and 5.8, respectively. The conclusion is that the phases of 0 and $\pi/4$ produce similar results, while the phase of $\pi/2$ has very different behaviors. In general, the case of zero phase has highest energy in the (2, 2) and (0, 2) modes and higher momentum thickness growth rate than the phase of $\pi/4$. The higher value of E_{20} for the case of $\pi/4$ suggests that the streamwise vortex structures obtain energy from the (2, 0) mode as well as the mean flow. The plots of u', v', and w' also show that the zero phase has higher velocity perturbations. The much lower level of velocity perturbations and the 2-D modal energies of the $\pi/2$ phase should be due to another mechanism. At this phase, no organized streamwise vortex tube is expected to form. The DNS results of Sandham and Reynolds (1989, 1991) show no sign of streamwise streaks at this phase.

5.3.2 Three-dimensional subharmonic mode

Next, the structures evolving from the (1, 1) mode superimposed on the (2, 0) mode are studied. The results can be extended to the (1, 2) mode, which is expected to produce similar results but with different spanwise wavelength.

Depending on the choice of phase, this mode may produce completely different structures. When the phase of $\pi/2$ is used, the vertical velocity perturbations have maximum values along the K-H vortex tubes. The direction of the velocity perturbations changes along the span of the K-H vortex tubes and this mode will produce the same structure as the helical pairing mode of Pierrehumbert and Widnall (1982). If the phase is chosen to be π or 0, the maximum streamwise vorticity perturbations appear at the stagnation points formed by the K-H vortex tubes.

The development of modal energies, momentum thickness, and velocity variations for the two different phases are shown in Figs. 5.9, 5.10, and 5.11. The amplitudes of the (2, 0) and (1, 1) modes are 0.02 and 0.005, respectively. After a period of initial growth, the case with phase of π shows almost complete saturation. Most of these quantities level off. The suppression of the mixing layer's growth seems to be closely related to a mechanism that are very similar to the one generated by the (1, 0) mode with phase of π, which is discussed in section 5.2. When the phase of

the (1, 0) mode is π, this mode grows by extracting vorticity from one of the (2, 0) mode's K-H vortices to supply the other. When the same phase is used for the (1, 1) mode, the periodicity in the spanwise direction strengthen and weaken the (2, 0) mode's K-H vortex tubes alternatively along the span. This mechanism cause the K-H vortex tubes to break down into discrete regions of vorticity concentration. The uneven distribution of spanwise vorticity along the spanwise direction may destroy the favorable strain rate field that is needed for the growth of the streamwise vorticity perturbations.

Although the helical pairing case shows significant and continuous growth, no pairing is observed. The vortex structures shown by low pressure surface (Fig. 5.12) show no sign of direct interaction between the two K-H vortex tubes. These results agree with the DNS simulation performed by Sandham and Reynolds (1989).

6. DEVELOPMENT AND BREAKDOWN OF LARGE-SCALE STRUCTURES

In this chapter, numerical simulations are presented to study the development of the most common large structures and their role in the transition process.

6.1 Computational Box and Initial Conditions

The simulations use a temporally developing mixing layer with a convective Mach number of 0.4. In the two homogeneous directions (x and z), the computational box has the dimension of $2\pi/0.2$ that is twice the wavelength of the most amplified 2-D wave. In the transverse (y) direction, the box extends from $y = -24$ to $y = 24$. A uniform grid system with (73*129*73) points is used.

Three different cases are studied. The initial perturbations of all three cases contain a random divergence-free velocity field. In addition to the random disturbances, the first two cases (cases A and B) are also perturbed by the stability eigenfunctions. Both cases include the (2, 0) and (2, 2) modes with phases of $\pi/2$ and 0, respectively. The amplitudes of the two modes are both 0.02. In addition to the above two modes, the first case, case A, also includes the (1, 2) mode with amplitude of 0.005 and phase of $\pi/2$. These amplitudes are based on the upper free-stream velocity. At this phase, maximum streamwise vorticity perturbations happen at the saddle points of the K-H vortices. The second case, case B, also includes the (1, 0) mode with phase of $\pi/2$, the pairing phase, and amplitude of 0.0025. The smaller ampli-

tude is chosen to delay the pairing until the streamwise vortices are fully formed. The value of 0.0025 is found to be adequate after a few test runs using a coarse grid of (55*129*55) points.

Three random divergence-free velocity fields with different energy levels are used in the three cases. The pressure perturbations are computed by solving Poisson's equation (see chapter 3). The strength of random disturbance decays like $e^{-(y/4)^2}$. Its 3-D energy spectrum function E(k) has a uniform value of each shell in Fourier space if $0.412 \leq k \leq 7.09$ and vanishes outside this range, where k is the middle wavenumber for each shell. A total of 72 shells, with equal thickness from 0 to k_{max}, defined as $\sqrt{(\pi/\Delta x)^2 + (\pi/\Delta y)^2 + (\pi/\Delta z)^2}$, are used. The uniform values are 10^{-6}, 10^{-7}, and 10^{-5} for cases A, B, and C, respectively. The RMS of velocity perturbations near the interface for the case of 10^{-5} is approximately 0.02.

All three cases are studied using the MacCormack scheme. In case A, we use the linear combination model (LCM), while in the other two cases the Smagorinsky model is used. The influence of numerical schemes and turbulence model will be discussed in chapter 7.

6.2 Case A

The purpose of this case is to study the formation of the streamwise vortex tubes and their interaction with the primary spanwise (K-H) vortex tubes. Therefore, the initial perturbations include the (2, 0) mode and the (2, 2) mode with same amplitude. The modal energy of the most energetic modes as a function of time are presented in Fig. 6.1. As one would expect, the 2-D fundamental mode, the (2, 0) mode, being the most amplified one, dominates the initial stage in the evolution of the mixing layer. It represents the rapid development of the Kelvin-Helmholtz rollers (K-H rollers), and it saturates at time $t \simeq 35$. The slow growth and low energy content of the 2-D subharmonic, which is given by the (1, 0) mode, shows that pairing of the K-H rollers is absent. The experiments performed by Ho and Huang (1982) show that a forcing frequency of upstream disturbances that is close to the natural frequency, whose counterpart in a temporal layer is the most amplified wavenumber, has the tendency of suppressing the growth of the subharmonic. The

growth of the (1, 0) mode in this case also shows similar tendency. Near the end of this simulation, Fig. 6.1c shows that the most energetic mode is the (0, 2) mode. The disturbance field of the superposition of the modes (0, 2) and (0, -2) gives two rows of counter rotating streamwise vortices (Ragab *et al.* 1992). Therefore, strong streamwise vortices seem to dominate the mixing layer near the end of simulation.

Contours of spanwise vorticity, ω_z, are shown in Fig. 6.2a at $t = 32.7$. The contours are in one of the $x - y$ planes where the streamwise vortex tubes evolving from the (2, 2) mode are expected to appear. We observe that the K-H vortex cores have fully formed. The velocity vectors in the same plane are shown along with the contours of ω_z in Fig. 6.2b, the high strain rate at the saddle point is evident. Because the phase of the 3-D eigenfunction disturbance is chosen such that the maximum streamwise vorticity coincides with the saddle points, we expect a rapid growth of streamwise vorticity in the braid region between the neighboring K-H vortex tubes. When viewed in the $x - y$ plane, the disturbance field of the (2, 2) mode produces an extremum of streamwise vorticity in the braid region and another extremum of the opposite sign in the cores of the K-H rollers. The latter grows by the bending of the K-H vortex tubes.

The structure due to the growth of the (2, 2) mode becomes very clear at $t = 40.8$ as shown in Fig. 6.3, in which the surface of constant ω_{xy}, defined as $(\omega_x{}^2 + \omega_y{}^2)^{\frac{1}{2}}$, is shown by perspective view and projections. Note that for visualization purposes, the box is extended by 50% in the two homogeneous directions using periodic conditions. The remaining 3-D perspectives and 2-D projections in this chapter will use the extended box. The vortex lines through these streamwise streaks (Fig. 6.4) fit the description of the hairpin structures by Bernal and Roshko (1986). In addition to the streamwise vortex tubes, there are the ellipsoid-shaped regions of high ω_{xy} which originate from the tilting of the vorticity vectors along the K-H vortex tubes. The tilting of the spanwise vortex tube will also shift the region of maximum spanwise vorticity and produce the cup-shaped structure shown in Fig. 6.5b, which appear at the heads of the bent spanwise vortex tubes (Fig. 6.5a), while high ω_{xy} happens in the middle of the legs. These cup structures have been observed in the DNS results of Roger and Moser (1991).

Pierrehumbert and Widnall (1982) in their analysis of the translative mode, conjecture that the velocity perturbations at the K-H vortex cores will shift the vortex core up and down into the free streams and make the K-H vortex tubes incline in the mean flow direction. Although the (2, 2) mode does contain significant vertical velocity component in the K-H vortex cores, the plot in Fig. 6.5b shows that the undulation of K-H vortex tubes happens mostly in the streamwise direction.

The strain rate field at the saddle points elongates the streamwise vortex tubes, makes them wrap around the K-H vortex tubes and hence leads to direct vortex interaction between the two kinds of vortex structures. As will be seen later, these interactions will cause severe distortion in the two kinds of vortex tubes and mark the beginning of the breaking of the large structures into small scales.

Next we discuss these vortex interactions and show how the streamwise vortex tubes replace the K-H vortex tubes and become the dominant vortex structures in the mixing layer. Shown in Fig. 6.6a are the contours of ω_{xy}, which takes the sign of ω_x, and velocity vectors in the $z-y$ plane cut through the mean center of one spanwise vortex tube ($x = \frac{1}{4}L_x$) at $t = 48.7$. This plane is also marked in Fig. 6.3c, which shows that the middle row of vortices are the intersection of the plane with the undulated spanwise vortex tube. The top and bottom rows of vortices in Fig. 6.6a come from the elongated streamwise vortex tubes originating from the two neighboring braid regions. The streamwise vorticity components, produced by vortex tilting of the K-H vortex tubes, play a major role in the following evolution of streamwise streaks. The plot of velocity vectors in Fig. 6.6b shows that the induced velocity by the middle row of vortices at the centers of the top row of vortices will make the two central vortices move away from each other and hence bring the outer pair of vortices closer. The opposite movement happens to the lower row of vortices. The new location of the vortices in the same plane at a later time, $t = 64$, is shown in Fig. 6.7. Comparing Fig. 6.6 and Fig. 6.7, one should note the significant dislocation of the streamwise vortex tubes.

To give a clear view of the dislocation of streamwise vortex tubes, the projection of these vortex structures at $t = 64$ on the $x-z$ plane is shown in Fig. 6.8. In addition to the dislocation of the streamwise vortex tubes, we also notice significant distortion

of the K-H vortex tubes. Except for the growth of streamwise vorticity disturbances, part of the distortion is due to the interaction between the K-H vortex tubes and streamwise vortex tubes near the heads of K-H vortex tubes. It is well known that two counter-rotating vortices with equal strength will move in the direction perpendicular to the axis connecting them. Thus, as the strength of the streamwise vortex tubes grows to a level comparable to the streamwise vorticity components in the tilted part of the K-H vortex tubes, near the heads of the undulated K-H tubes, the legs tend to move with the streamwise vortex tubes. These movements are marked by arrows in Fig. 6.8b, in which the dark lines are a pair of vortex lines through the K-H vortex tubes. At this time ($t = 64$), we also notice loss of vorticity in the middle of each leg of the K-H vortex tubes and that causes the breaking of what used to be the spanwise structure. At the location of breaking, $z = \frac{1}{8}L_z$, the contours of ω_y and ω_x in the $x - y$ plane are shown in Fig. 6.9. The contour plot of ω_y shows three centers of vorticity concentration (enclosed in the circles) in each K-H vortex core with one negative ω_y core (solid line) flanked by two positive ones. The two positive vortex cores extend in opposite directions (into and out of the paper) and form one leg of the K-H vortex tubes, while the negative one is caused by the change of direction of vortex lines through this leg. This change can be better demonstrated by the projection of vortex lines in the $x - y$ plane in Fig. 6.9c, which shows the same vortex lines as Fig. 6.8b. The arrows mark the movement near the heads during the vortex interaction with the streamwise vortex tubes. It should be noted that these vortex lines are approximately parallel to the $x - z$ plane early in the formation of streamwise vortex tubes (at $t = 40.8$, for example). The original orientation is shown by dash lines. This change of sign of transverse vorticity component will decrease the magnitude of ω_x through the vortex tilting mechanism, $\omega_y \frac{\partial U}{\partial y}$. And we notice that in the regions with negative ω_y, ω_x has much smaller values (Fig. 6.9b).

The distortion in the middle of each leg of the K-H vortex tubes also marks the end of organized flows at these locations. Before the distortion happens, the circled areas in Fig. 6.9 have only one center of vorticity concentration each. Now, there are three and two centers for Figs. 6.9a and 6.9b respectively. As flows in these regions become less organized, the pressure will not be able to maintain its low

value. At $t = 71.3$, the projection of constant pressure surface is shown in Fig. 6.9a, the dash lines mark the original K-H vortex tubes. We notice that the low pressure existing in the legs of the K-H vortex tubes has disappeared from this plot and the streamwise vortex tubes have become the dominant vortex structures at this time. Figures 6.10b and 6.10c show the projection of ω_{xy} and ω_z surface at the same time. Figure 6.10c shows two different regions that contain high spanwise vorticity. The first comes from the original K-H vortex tubes at their heads after being bent. The second type of spanwise vorticity exists in the middle of the streamwise vortex tubes after these structures undergo substantial distortion. The lines that form the surface in Fig. 6.10a are the intersections of $x - z$ planes with the constant pressure surface and we notice that the streamwise vortex tubes become more oriented in the y direction.

In the study of transition process of a temporally developing mixing layer, one of the difficulties is the lack of a generally applicable criterin of transition. As mentioned before, unlike the boundary layer flows, the growth of the mixing layer thickness is dominated by the pairing of large structures. To study the growth of the small-scale motions, the kinematic energy existing in scales smaller than a chosen value is summed up and shown as a function of time in Fig 6.11. The threshold wavenumber, k, (defined as $\sqrt{k_x^2 + k_y^2 + k_z^2}$), is 4α. We notice that the value begins to increase exponentially from $t \simeq 35$, when the streamwise vortex tubes have fully formed, to $t \simeq 70$ and then gradually levels off. No sudden jump is observed and the breaking of large structures does not seem to influence this process.

The growth of momentum thickness is shown in Fig. 6.12. The first substantial growth happens during the roll-up of the K-H vortices and ends at $t = 35$, approximately when the energy of the (2, 2) mode saturates. The curve basically levels off from 40 to 55. The growth rate picks up again after 55. This is also the time when substantial dislocation of the streamwise vortex tubes happens. We notice that the mixing layer shows very high growth rate between 55 and 70. After 70, the thickness maintain a lower but still very high growth rate. Since most large structures break up after 70, the growth might be due to the turbulent diffusion, while the rapid growth between 55 and 70 seem to have close connection with the dislocation of the

streamwise vortex tubes and distortion of the K-H vortex tubes.

6.3 Case B

The purpose of this simulation is to investigate the influence of the streamwise vortex tubes during the pairing process. Thus, in addition to the (2, 0) and (2, 2) modes of case A, the 2-D subharmonic mode, that is, the (1, 0) mode, is also included in the initial conditions.

The evolution of modal energy for selected modes and momentum thickness is shown in Figs. 6.13 and 6.14. The analysis of stability eigenfunctions in chapter 5 predicts that the (1, 0) mode with phase of $\pi/2$ causes pairing at $x = \frac{1}{2}L_x$. The effect of the (1, 0) mode on the two K-H vortex tubes can be seen in Fig. 6.15, which shows the the projection of constant pressure surface along with a few vortex lines through the streamwise vortex tubes (which are not yet strong enough to appear in this plot) at $t = 51.2$. The relative motion of the two K-H vortex tubes is very clear. As the two spanwise vortex tubes move closer, the strain rate field near the saddle point at $x = \frac{1}{2}L_x$ is strengthened, so are the streamwise and transverse vorticity components, while the opposite happens to the braid region at $x = L_x$. The effect of the K-H vortex tubes' motion on the strength of the streamwise vortex tubes is demonstrated in Fig. 6.16 by the projection of ω_{xy} surface at $t = 61.4$. Three kinds of structures are observed in this plot: the K-H vortex tubes, the streamwise vortex tubes at $x = \frac{1}{2}L_x$ and L_x. We notice that much higher values of ω_{xy} exist in the braid region at $x = \frac{1}{2}L_x$ than at $x = L_x$. The stronger vortex flows in the streamwise vortex tubes at $x = \frac{1}{2}L_x$ induce very low pressure. Figure 6.17 shows the projection of constant pressure surface along with selected vortex lines at $t = 61.4$. The dominant low-pressure region comes from the streamwise vortex tubes ($x = \frac{1}{2}L_x$). Because of the much higher vorticity in the streamwise vortex tubes, the vortex interaction discussed in case A (Figs. 6.6, 6.7, and 6.8b) has much stronger effect on the two kinds of vortex structures and creates the neck-shaped vortex lines (streamwise vortex tubes) in Figs. 6.17 and 6.18. Figure 6.18 shows the same vortex lines as those in Fig. 6.17. A total of five vortex lines are shown, one for each of

the two K-H vortex tubes, two for the streamwise vortex tubes at $x = \frac{1}{2}L_x$, and one for the streamwise vortex tubes at $x = L_x$. As the two counter-rotating streamwise vortex tubes near the neck get very close, because of the existence of dissipation (turbulence model and numerical dissipation in this case), the vortex line through the neck forms a closed vortex line. This kind of connection mechanism for two counter-rotating vortex tubes has been studied by Melander and Hussain (1989). Shown in Fig. 6.19 are vortex lines resulting from the reconnection mechanism.

The vortex lines shown in Figs. 6.18 and 6.19 are chosen to show some basic features in the mixing layer. Depending on the orientations and locations, vortex lines at this time have different behaviors from each other. To give a better view of the vorticity field, more vortex lines are shown in Fig. 6.20.

Although the projetion of constant pressure surface in Fig. 6.17 seems to suggest that the streamwise vortex tubes are taking the dominant role in the flow field, as the two K-H vortex tubes move even closer, these structures coming from the streamwise vortex tubes will finally break down. Shown in Fig. 6.21 are the projections of constant pressure surface at $t = 71.1$. The first three plots (Fig. 6.21a, b, and c) show projections on the $x - z$ plane. Figure 6.21a shows all the structures and may look a little complicated. Figure 6.21b, and c show the structures in the upper ($y > 0$) and lower ($y < 0$) streams separately. The K-H vortex tubes can be easily identified, so are the streamwise vortex tubes in the non-pairing braid region. The remaining structures, looking like a semi-ring from the projection on the $z - y$ plane (Fig. 6.21d), are the remains of the streamwise vortex tubes. Fig. 6.21a shows that the two K-H vortex tubes have almost reached the same streamwise location ($x = \frac{1}{2}L_x$). Since the low pressure suggests the existence of organized vortex flows, the regions that used to be the streamwise vortex tubes but do not appear in Fig. 6.21 should be filled with less organized motions. This assumption is verified by the 2-D contour plots of ω_z and ω_{xy} in the $z - y$ plane at $x = \frac{1}{2}L_x$ in Fig. 6.22.

In this work, attempts are made to find out the mechanism causing the small-scale motions with positive ω_z observed in Fig. 6.22a (dot lines). The reason for this choice is that these structures can be easily analyzed using vortex lines. For a mixing layer discussed in this work, the mean vorticity is in the negative z direction.

Therefore, regions with positive spanwise vorticity can be easily identified on vortex lines. In Fig. 6.22a, there are three kinds of "vortices" with positive values of ω_z, marked by A, B, and C. The vortex lines through these three points are shown in Figs. 6.23, 6.24, and 6.25. The vortex line through A (Fig. 6.23) apparently comes from the streamwise vortex tubes in the non-pairing braid region and is the result of the vortex interaction of counter-rotating vortices similar to that discussed in Fig. 6.18. The shape of the vortex line through B (Fig. 6.24) suggests that it is a vortex line through one of the K-H vortex tubes. The vortex line through C (Fig. 6.25) is found to come from the streamwise vortex tubes in the pairing region. This is also the typical vortex line in the semi-ring structures in Fig. 6.21. All of the positive spanwise vorticity components along the three vortex lines are due to the neck-shaped structures, which are caused by the vortex interaction of streamwise vorticity existing in the K-H vortex tubes and the streamwise vortex tubes. Although this analysis can not prove that this kind of vortex interaction is the major mechanism that leads to the transition in a mixing layer, it does show that it plays an important role in the formation of small-scale motions in the early stage of pairing.

The structures at $t = 80.6$ are discussed next. Figure 6.26 shows the projection of constant pressure surface on the $x - z$ plane. Two separate plots are used for the upper and lower streams, respectively. The semi-ring structures observed at $t = 71.1$ (Fig. 6.21) still maintainss their low pressure. This indicates that the flows in these regions are organized during this period ($t = 71.1$ to $t = 80.6$). In addition, their locations show little change. Some of the structures are the remains of the K-H vortex tubes (marked). We notice that the K-H vortex tube that is formed at $x = \frac{1}{4}L_x$ has moved in the upper stream to the right portion of the computational box, while the one at $x = \frac{3}{4}L_x$ has moved to the left. Another organized structure at this time is the streamwise vortex tubes in the braid region between pairing K-H vortices.

Figure 6.27 shows the projection of constant ω_z surface on the $x - z$ plane in two separate plots. We notice that the semi-ring structures coming from the streamwise vortex tubes (which are oriented in the z direction at this time) produce high

spanwise vorticity component. The 2-D contour plots of spanwise vorticity in Fig. 6.28, which shows contours in the $x-y$ plane at $z = \frac{1}{4}L_z$, also shows that these structures (marked by box in Fig. 6.28) have very high values of ω_z. The projection of surface of constant vorticity magnitude ($\sqrt{{\omega_x}^2 + {\omega_y}^2 + {\omega_z}^2}$) on the $x-z$ plane are shown in Fig. 6.29. There exists a lot of small-scale structures in the pairing region. Another 2-D contours plot for the spanwise vorticity component in the $x-y$ plane at $z = \frac{1}{8}L_z$ is shown in Fig. 6.30. Note that this is the plane that cuts through the center of one of the streamwise vortex tubes when they are still oriented in the streamwise direction. More small-scale motions are observed in this plane.

The symmetry of structures in Figs. 6.27 and 6.29 suggests that the flow field at this time is mostly produced by the development of the stability eigenfunctions. However, the existence of random disturbances does make it difficult to generate good-quality vortex lines. In order to produce better-quality vortex lines, the simulation is repeated without including the random disturbances in the initial conditions. The contour plot in the same plane as Fig. 6.28 is shown in Fig. 6.31. The time is 80.8. No substantial difference is noticed between the two plots (Figs. 6.28 and 6.31). The first set of vortex lines are obtained at $t = 71.2$. They are shown in Fig. 6.32. These two vortex lines represent the basic structure of the two K-H vortex tubes at this time.

Next, the vortex lines at $t = 80.8$ are presented. A set of vortex lines that pass through the remaining organized structures of the streamwise vortex tubes are generated. These vortex lines are for the organized structures in the upper stream, which are located in the right part of the computational box. Figure 6.33 shows the projection of these vortex lines along with the constant pressure surface. Figure 6.33a shows only the structures in the upper stream. Figure 6.33b shows the structures between $x = \frac{1}{4}L_x$ and $x = \frac{3}{4}L_x$. We notice that the vorticity in these structures are mostly in the spanwise direction.

In the next three figures, Figs. 6.34, 6.35, and 6.36, more vortex lines are shown. The vortex lines in Fig. 6.34 originate from the $y-z$ plane at $x = \frac{1}{2}L_x$. The starting points of these vortex lines are evenly distributed in a rectangle from $z = \frac{1}{2}L_z$ to L_z and $y = -1.5$ to 1.5. A lot of these vortex lines pass the remaining streamwise

vortex tubes. The second set of vortex lines, shown in Fig. 6.35, originate from the $x-y$ plane at $z=\frac{5}{8}L_z$ in the rectangle from $x=\frac{7}{24}L_x$ to $\frac{17}{24}L_x$ and $y=-1.125$ to 1.125. The vortex lines in Fig. 6.36 originate from the $x-y$ plane at $z=\frac{3}{4}L_z$ in the same rectangle as Fig. 6.35. The $x-y$ plane at $z=\frac{3}{4}L_z$ is one of the $x-y$ planes where the connection of vortex lines are expected to happen (the other three are at $z=0$, $\frac{1}{4}L_z$, and $\frac{1}{2}L_z$). A few closed vortex lines appear in this plot.

The flow field at $t=98.9$ is discussed next. Fig. 6.37 shows the spanwise vorticity contours in two $x-y$ plane at $z=\frac{1}{8}L_z$ and $\frac{1}{4}L_z$. The flow field is filled with small-scale structures. The projection of constant pressure surface in Fig. 6.38 also shows that no organized motion exists in the pairing region.

The evolution of energy existing in the small-scale motions is shown in Fig 6.39. Very fast growth is observed from $t=40$ to $t=60$ followed by a period with lower rate. The period with higher growth rate matches the time when the streamwise vortex tubes grow by the vortex stretching. The growth rate in case A in the same period (from 40 to 60) is about 30% lower. Therefore, this high growth rate is associated with the high strain rate before the pairing, while the second stage ($t=61$ to $t=89$) represents the continuous production of small-scale motions following the breaking of the large structures.

For reference, some turbulence quantities at $t=108.4$ are shown in Fig.6.40 as functions of transverse coordinate, y. The values, u', and $\overline{u'v'}$ are defined by

$$u'=\sqrt{\overline{(u'-U(y))^2}} \tag{6.1}$$

$$\overline{u'v'}=\overline{(u'-U(y))(v'-V(y))} \tag{6.2}$$

where $U(y)$ is the mean streamwise velocity averaged over the $x-z$ plane and overline represents averaging over the $x-z$ plane. $v', w', \overline{u'w'}, \overline{v'w'}$ are defined similarly. These quantities,however, should not be interpreted as the turbulence intensity and Reynolds stress measured in experiments. The values obtained in experiments are generally the average of a much higher number of samples, which may involve thousands of passing primary vortices.

6.4 Case C

In this case, a divergence-free random velocity field is used to initialize the simulation. The evolution of modal energy for selected modes are shown in Fig. 6.41

In Fig. 6.42, the projection of a surface of constant spanwise vorticity at $t = 46.8$ is depicted. There are basically two spanwise vortex tubes but with non-uniform strength along the span. Between the spanwise vortex tubes, there exist a few streamwise vortex tubes with low strength (not shown). The development of these streamwise vorticity disturbances is shown in Fig. 6.43, which shows the projection of ω_{xy} at two different times, $t = 56$ and $t = 64.7$. We notice that the streamwise streaks between the spanwise vortex tubes grow stronger and more elongated with time. This growth is due to the strain field created by the neighboring K-H vortex tubes. Similar to those observed in case A, these streamwise streaks are also inclined in the mean flow direction (Fig. 6.43c). Also at $t = 64.7$, we find a region with direct interaction between the two K-H vortex tubes. This can be seen from the projection of spanwise vorticity surface (Fig. 6.44a). At the cross section marked by A-A, we notice a region of high spanwise vorticity across the two K-H vortex tubes. A two-D spanwise vorticity contours on A-A (Fig. 6.44b) show a structure very similar to 2-D pairing. However, the pairing happens in a small portion along the span. The contours of ω_z at $z = \frac{1}{2}L_z$ (Fig 6.44c) show two separate spanwise vortices. This pairing region is also the area where irregular small-scale motions first appear. As the simulation continues, we notice another region of interaction between the two K-H vortex tubes. The process can be described by the projection of constant pressure surface on $x - z$ plane at $t = 89.7$ and 98.9 shown in Fig. 6.45. We see that the K-H vortex tubes move towards each other on the plot until the two overlap. Although these vortices overlap in the horizontal plane, they are separated in the transverse direction. The spanwise vorticity contours in the plane cut through this region (B-B) (Fig. 6.46b) show that these two vortex centers are separated in the transverse direction. Their movements in the $x - z$ plane appear to be due to the free stream velocity. Therefore, this process fits the description of the early stage of helical pairing of Pierrehumbert and Widnall (1982), in which two neighboring K-H vortex tubes move up and down respectively into the free streams and then convect

in opposite directions with the free-stream. However, no sign of pairing appears, the two vortex cores are far away from each other in the transverse direction. At the same time, in the region of 2-D pairing observed at $t = 64.7$, we see production of small-scale motions, (Fig. 6.46a). The time history of energy level of small scale motions (Fig. 6.47) show a lower growth rate than case A and case B.

6.5 Chapter Summary

This chapter is concerned with the numerical study of the 3-D secondary structures in a subsonic mixing layer. The results presented in this chapter confirm the importance of the streamwise vortex structures. It is found that the growth of the streamwise vortex tubes always accompanies the distortion of the primary structures, the K-H vortex tubes. The simulation of the instability mode with streamwise vorticity disturbances but no perturbations leading the undulations of the K-H vortex tubes shows almost no growth (chapter 5).

The most important mechanism in the secondary motions is the vortex interaction between the streamwise vorticity components existing in the streamwise vortex tubes and the distorted K-H vortex tubes. The efficiency of the pairing process in generating the small-scale motions can be attributed to the enhanced vortex interaction due to the relative motions of the two pairing K-H vortex tubes. This vortex interaction proves to be the major mechanism leading to the small-scale motions in the early stage of pairing. The simulations also show that, with the existence of streamwise vortex tubes, the dominant 2-D structures (the K-H vortex tubes) are not able to maintain their organized flows after sustaining substantial distortions.

7. COMPARISON OF NUMERICAL SCHEMES

In this chapter, different numerical schemes with different turbulence models are compared. For the comparison of finite-difference schemes, the simulations are initialized by the same perturbations as those in case A in chapter 6, which include a (2, 0) mode to generate the K-H vortices and a (2, 2) mode to generate the secondary streamwise vortex tubes, and a (1, 2) mode. In the comparison involving the pseudo-spectral method, the data sets obtained in chapter 6 for case A are used as the initial conditions. These data sets are obtained using the MacCormack scheme with LCM.

7.1 Comparison of Finite-difference Schemes

First, results obtained by using different finite difference schemes and turbulence models are compared. The numerical methods used in the simulations include the MacCormack (2, 4) scheme, and the three-stage second-order Runge-Kutta scheme using fourth-order central difference or third-order flux splitting for the convection terms. Other details, including the finite difference form of viscous terms (turbulence model), are discussed in chapter 3. Two models, the Smagorinsky model and the linear combination model (LCM), are tested. Three values of C_R, turbulence model constant, are used. These simulations use the initial conditions of case A. The evolution of modal energy for selected modes and 1-D energy spectra at two different times are compared. The results are shown in Figs. 7.1 and 7.2. The conclusions

are summarized as follows:

1. As expected, the flux-difference-splitting scheme produces most dissipation, followed by the fourth-order MacCormack scheme.
2. The linear combination model in general provides more dissipation than the Smagorinsky model for small-scale motions. But it has also significant influence on the large-scale motions.
3. The Smagorinsky model, even with increased model constant, is not able to dissipate the aliasing errors of the RK/central-difference scheme. Either laminar viscous terms or explicit artificial damping is needed for this scheme.
4. The spectra of schemes using different model constants show significant difference even at low wavenumber range.

In these simulations, the MacCormack scheme gives reasonably good performance. It is much faster than the RK scheme with central difference and offers enough but not excessive dissipation at the high-wavenumber region.

7.2 Comparison of MacCormack Scheme and Pseudo-spectral Scheme

Removal of aliasing errors

There have been arguments about the necessity of dealiasing for the pseudo-spectral method. The general conclusion is that, as long as the grid is fine enough, dealiasing may not be needed in direct numerical simulation. For DNS, to say that the grid is fine enough is equivalent to saying that the Reynolds number is low enough for the grid system or the smallest scale of fluid motions is large enough for the grid system to resolve. Therefore, in DNS, we may rely on the laminar viscosity to dissipate the continuous generation of small-scale motions. In LES, however, the turbulence model supplies dissipation only where there is a mean velocity gradient. In regions without mean velocity gradient, the fluid motions with smaller and smaller scales will continue to appear and exceed the resolution of the grid system. Therefore, dealiasing is much more important in LES.

As mentioned in chapter 3, the 3/2 rule used to eliminate aliasing errors in the quadratic nonlinear terms is not enough to remove all aliasing errors in the cubic nonlinear terms. If a similar dealiasing scheme is applied to a cubic nonlinear term, each of its components must be removed of one-half of the Fourier modes to guarantee that one-half of the product's Fourier modes are free of aliasing errors. This kind of elimination of the Fourier modes will considerably offset the advantage of the pseudo-spectral method. One alternative is to divide the calculation of a cubic nonlinear term into two steps. In the first step, the product of two of the three components are computed and dealiasing (eliminating one-third Fourier modes) is applied to this product. In the second step, the product of the dealiased product and the third component is obtained and dealiasing is applied again. After these two steps, all the aliasing errors are confined to the higher one third modes and the lower two thirds of the final product's Fourier modes are free of aliasing errors.

The typical cubic term for compressible flows has the form of $\rho u_i u_j$. At low Mach number, distribution of density tends to be very smooth and the higher Fourier modes have very low value and the cubic nonlinear term's behavior will be similar to a quadratic one. Therefore, the one-step 3/2 rule used for incompressible flow may be enough to remove most of aliasing errors.

The extension of dealiasing to 2-D or 3-D problem is straightforward. For the 2-D case, the dealiasing can be performed by removing modes outside a rectangle of $\frac{2}{3}\pi/\Delta x$ by $\frac{2}{3}\pi/\Delta y$ in the Fourier space. Another variation (Erlebacher *et al.* 1990) is obtained by decreasing this area to the largest circle that the rectangle can accommodate. This scheme eliminates more Fourier modes and provides more dissipation.

With the above discussions, we come up with four different dealiasing schemes: Dealiasing can be applied in one or two steps, and the area in the Fourier space for the 2-D case can be a rectangle or a circle. These four different versions will be tested using LES with the Smagorinsky model. In the transverse direction, the sixth-order compact scheme is used with a sixth-order artificial damping. The coefficients of the damping terms are $0.08\Delta y^6$ for the momentum equations and energy equation, and $0.125\Delta y^6$ for the continuity equation. A grid with (73*129*73) points is used. The

test runs use one of the data set at $t = 64.73$ of case A in chapter 6, which is obtained using the MacCormack scheme with LCM, as initial conditions. The simulations stop at $t = 92.8$. The 1-D energy spectra for the four different variations of the dealiasing scheme are shown in Fig. 7.3. We notice that the difference between the one-step and two-step versions is very small. This should be due to the smooth distribution of density. For highly compressible flow, the difference might be more evident. The choice of area in the Fourier space shows difference at the tail of the spectra.

The pseudo-spectral method without any dealiasing treatment is also tested using the same initial conditions. It diverges after a short period at $t \simeq 68$.

Next, the comparison between the pseudo-spectral method and the MacCormack method is presented. The dealiasing scheme is the two-step one and removes modes outside a rectangle in the Fourier space. The data set of case A at $t = 32.7$ obtained using the MacCormack scheme with LCM is used as the initial conditions for the simulations. Only the Smagorinsky model is used for both methods. The time advancement of the pseudo-spectral method uses a third-order low-storage RK scheme described in chapter 3. The compact scheme in the transverse direction uses the sixth-order artificial damping with coefficients of 0.125 and 0.08 (see above). The energy spectra are compared at $t = 71$ and $t = 99$ in Figs. 7.4 and 7.5. Also shown in these figures are the spectra for the case using the MacCormack scheme with LCM. The spectra of pseudo-spectral method and MacCormack scheme show good agreement in the low-wavenumber range at $t = 71$. Their difference with the MacCormack scheme with LCM is much more evident. This fact once verifies that the LCM has significant effect on the large-scale motions. At $t = 99$, the two methods with the same model (Smagorinsky model) show discernible difference even at low-wavenumber range. Apparently, the different behaviors of the two methods at high-wavenumber range begin to influence the large-scale motions after a long period of time.

Basically, the pseudo-spectral method produces very good results. The spectra show little aliasing errors, which always appear in the form of abrupt rise at the tail of the spectra.

8. CONCLUSIONS

This work has been concerned with the numerical study of the low-Mach-number mixing layer. One objective is to study the combined effect of numerical dissipation and turbulence model on the energy spectra in the high-wavenumber range. Another objective in this work is the investigation of the transition process of large-scale vortex structures to small scales.

Next, the important results are summarized.

- In three-dimensional simulations, the eigenfunctions obtained by linear stability analysis prove to be valuable in initializing numerical simulations so that the desired vortex structures are obtained.

- Numerical simulations initialized by different eigenfunctions with various phases show that the most important 3-D structure is the 3-D fundamental mode, which leads to the formation of streamwise vortex tubes and the bending of the spanwise (K-H) vortex tubes.

- The 3-D subharmonic modes are found to be much less efficient than the 3-D fundamental ones in producing energetic vortex flows, which is vital for enhancing mixing at the molecular level. The helical pairing mode, which involves substantial bending of the K-H vortex tubes, is not found to cause any direct interaction of the K-H vortex tubes, while the second 3-D subharmonic mode,

the one with high streamwise vorticity perturbations at the saddle points, shows almost no growth after the formation of the K-H vortex tubes. It is found that this mode weakens the organized structure of the primary (K-H) vortex tubes by breaking them into discrete regions of vorticity concentration. The disintegration of the primary structures in turn prohibits the growth of the secondary structures such as the streamwise vortex tubes. A further study of this mechanism can be very helpful for one who aims to suppress the growth of vortex structures in free shear flows.

- In the evolution of large structures in a temporal layer, the vortex interaction between the streamwise vorticity components existing in the distorted K-H and streamwise vortex tubes play a dominant role. It induces the dislocation of the streamwise vortex tubes and creates the Λ-shaped structure and later triggers the reconnection mechanism. For the K-H vortex tubes, this vortex interaction causes substantial distortion and makes the K-H vortex tubes unable to maintain uniform strength along the span. The generation of small-scale motions in the pairing process is also found to be closely related to this vortex interaction, since the strength of the streamwise vortex tubes will be significantly increased by the amplified strain rate field when the two pairing vortices approach each other.

- In the pairing case, the computational box is chosen to accommodate only two K-H vortex tubes, therefore only one pairing is observed. During the pairing process, the streamwise vortex tubes in the second braid region do not show the dislocation that leads the formation of Λ-shaped structure. This might be due to the fact that the effective shape of the merged K-H vortices show no spanwise undulations. Therefore, the second pairing process is expected to be very different from the first one. This is a subject worth further study.

- In this work, different numerical schemes are tested. For this kind of transitional flow with mean velocity gradient continuously supplying energy to small-scale motions, the Runge-Kutta/central-differencing scheme can not produce acceptable results without artificial dissipation or molecular viscosity. In addition,

the different behaviors of numerical schemes and turbulence model at the high-wavenumber range is found to influence the large-scale motions after a long period of time when all of major orginized vortex structures break down into small-scale motions.

BIBLIOGRAPHY

Bardina, J., Ferziger, J. H., and Reynolds, W. C., (1983) "Improved subgrid-scale models based on large-eddy simulation of homogeneous, incompressible, turbulent flows," Dept. of Mechanical Engr., Stanford University, Report No. **TF 19**.

Bayliss, A., Maestrello, L., Parikh, P. and Turkel, E. (1986) "Numerical simulation of boundary-layer excitation by surface heating and cooling," AIAA Journal **24**(7), 1095.

Bernal, L. P. and Roshko, A. (1986) "Streamwise vortex structures in plane mixing layers," J. Fluid Mech. **179**, 499.

Bogdanoff, D. W. (1983) "Compressibility effects in turbulent shear layers," AIAA Journal **21**, 926.

Breidenthal, R. (1980) "Response of plane shear layers and wakes to strong three-dimensional disturbances," Phys. Fluids **23**(10), 1929.

Brown, G. L. and Roshko, A. (1974) "On density effects and large structure in turbulent mixing layers," J. Fluid Mech. **64**, 775.

Canuto, C., Hussaini, M. Y., Quarteroni, A., and Zang, T. A. (1988) "Spectral methods in fluid dynamics,", Springer-Verlag.

Corcos, G. M. and Sherman, R. S. (1984) "The mixing layer: deterministic models of a turbulent flow. Part 1. Introduction and the two-dimensional flow," J. Fluid Mech. **139**, 29.

Deardorff, J. W. (1970) "A numerical study of three-dimensional turbulent channel flow at large Reynolds numbers," J. Fluid Mech. **41**, 453.

Deardorff, J. W. (1973) "The use of subgrid transport equations in a three-dimensional model of atmospheric tubbulence," J. Fluids Engr. **95**, 429.

Erlabacher, G., Hussaini, M. Y., Speziale, C. G., and Zang, T. A. (1990) "Toward the large-eddy simulation of compressible turbulent flows," ICASE Report **87**-20.

Erlabacher, G., Hussaini, M. Y., Speziale, C. G., and Zang, T. A. (1992) "Toward the large-eddy simulation of compressible turbulent flows," J. Fluid Mech. **238**, 155.

Ferziger, J. H. (1977) "Large eddy simulation of turbulent flows," AIAA Journal **15**(9), 1261.

Germano, M., Piomelli, U., Moin, P., and Cabot, W. (1991) "A dynamic subgrid-scale eddy viscosity model," Phys. Fluids A **3**(7), 1760.

Gottlieb, D. and Turkel, E. (1976) "Dissipative two-four methods for time-dependent problems," Math. Compt. **30**(136), 703.

Herring, J. R. and McWilliams, J. C. (1985) "Comparison of direct numerical simulation of two-dimensional turbulence with two-point closure: the effects of intermittency," J. Fluid Mech. **153**, 229.

Hirsch, C. (1990) "Numerical computation of internal and external flows," Wiley, NY.

Ho, C.-M. and Huang, L. S. (1982) "Subharmonics and vortex merging in mixing layers," J. Fluid Mech. **119**, 443.

Ho, C.-M. and Huerre, P. (1984) "Perturbed free shear layers," Annu. Rev. Fluid Mech. **16**, 365.

Kim, J., Moin, P., and Moser, R. D. (1987) "Turbulence statistics in fully-developed channel flow at low Reynolds number," J. Fluid Mech. **177**, 133.

Lasheras, J. S., Cho, J. S., and Maxworthy, T. (1986) "On the origin and evolution of streamwise vortical structures in plane, free shear layer," J. Fluid Mech. **172**, 231.

Lasheras, J. S. and Choi, H. (1988) "Three-dimensional instability of a plane free shear: an experimental study of the formation and evolution of streamwise vortices," J. Fluid Mech. **189**, 53.

Lele, S. K. (1989) "Direct numerical simulation of compressible free shear flows," AIAA paper 89-0374.

Leonard, A. (1974) "Energy cascade in large-eddy simulations of turbulent fluid flows," Advs. Geophysics **18**, 237.

Lesieur, M., Staquet, C., le Roy, P., and Comte, P. (1988) "The mixing layer and its coherence examined from the point of view of two-dimensional turbulence," J.

Fluid Mech. **192**, 511.

Lessen, M., Fox, J. A., and Zien, H. M. (1965) "On the inviscid stability of the laminar mixing of two parallel streams of a compressible fluid," J. Fluid Mech. **23**, 355.

Lessen, M., Fox, J. A., and Zien, H. M. (1966) "Stability of the laminar mixing of two parallel streams with respect to supersonic disturbances," J. Fluid Mech. **25**, 737.

Maruyama, Y. (1988) "A numerical simulation of plane turbulent shear layer," Trans. Japan Soc. Aero. Space Sci. **31**-92, 79.

Melander, M. V. and Hussain, F. (1989) "Cross-linking of two antiparallel vortex tubes," Phys. Fluids A **1**(4), 633.

Metcalfe, R. W., Orszag, S. A., Brachet, M. E., Menon, S., and Riley, J. J. (1987) "Secondary instability of a temporally growing mixing layer," J. Fluid Mech. **184**, 207.

Michalke, A. (1965a) "On the inviscid instability of the hyperbolic tangent velocity profile," J. Fluid Mech. **19**, 543.

Michalke, A. (1965b) "On spatially growing disturbances in an inviscid shear layer," J. Fluid Mech. **23**, 521.

Monkewitz, P. A. and Huerre, P. (1982) "Influence of the velocity ratio on spatial instability of mixing layers," Phys. Fluids **25**, 1137.

Moser, M. M. and Rogers, R. D. (1991) "Mixing transition and the cascade to small scales in a plane mixing layer," Phys. Fluids A **3**(5), 1128.

Nygaard, K. J. and Glezer, A. (1991) "Evolution of streamwise vortices and generation of of small-scale motions in a plane mixing layer," J. Fluid Mech. **231**, 257.

Orszag, S. A. and Patterson, G. S. (1972) "Numerical simulation of three-dimensional homogeneous isotropic turbulence," Phys. Rev. Lett. **38**, 76.

Papamoschou, D. and Roshko, A. (1988) "The compressible turbulent shear layer: an experimental study," J. Fluid Mech. **197**, 453.

Papamoschou, D. and Roshko, A. (1986) "Observations of supersonic free shear layers," AIAA paper **86**-0162.

Pierrehumbert, R. T. and Widnall, S. E. (1982) "The two- and three-dimensional instabilities of a spatially periodic shear layer," J. Fluid Mech. **114**, 59.

Ragab, S. A., Sheen, S., and Sreedhar, M. (1992) "An investigation of finite-difference methods of large-eddy simulation of a mixing layer," AIAA paper 92-0554.

Ragab, S. A. and Wu, J. L. (1988) "Instabilities in the free shear layer formed by two supersonic streams," AIAA paper 88-0038.

Ragab, S. A. and Wu, J. L. (1989) "Linear subharmonic instabilities of periodic compressible mixing layers," AIAA paper 89-0039.

Ragab, S. A. and Wu, J. L. (1990) "Instabilities of supersonic shear flows," AIAA paper 90-0712.

Rai, M. M. and Moin, P. (1989) "Direct simulations of turbulent flow using finite-difference schemes," AIAA paper 89-0369.

Reynolds, W. C. (1990) "The potential and limitations of direct and large eddy simulations," in "Whither turbulence", Springer-Verlag.

Riley, J. J. and Metcalfe, R. W. (1980) "Direct numerical simulation of a perturbed, turbulent mixing layer," AIAA paper 80-0274.

Roe, P. L. (1981) "Approximate Reimann solvers, parameter vectors, and difference schemes," J. Comput. Phys. **43**, 357.

Sandham, N. D. and Reynolds, W. C. (1989) "A numerical investigation of the compressible mixing layer," Dept. of Mechanical Engr., Stanford University, Report No. **TF-45**.

Sandham, N. D. and Reynolds, W. C. (1991) "Three-dimensional simulations of large eddies in the compressible mixing layer," J. Fluid Mech. **224**, 133.

Schlichting, H. (1979) "Boundary-layer theory," 7th edition, McGraw-Hill, New York.

Smagorinsky, J., (1963) "General circulation experiments with the primitive

equations. I. The basic experiments," Monthly Weather Review **91**, 61.

Spalart, P. R. (1988) "Direct numerical simulation of a turbulent boundary layer up to R_θ =1410," J. Fluid Mech. **187**, 61.

Strang, G. (1968) "On the construction and comparison of difference schemes, SIAM J. Num. Anal. **5**(3), 506.

Stuart, J. T. (1967) "On finite amplitude oscillations in laminar mixing layers," J. Fluid Mech. **29**, 417.

Thompson, K. W. (1987) "Time dependent boundary conditions for hyperbolic systems," J. Comput. Phys. **68**, 1.

Winant, C. D. and Browand, F. K. (1974) "Vortex pairing, the mechanism of turbulent mixing layer growth at moderate Reynolds number," J. Fluid Mech. **63**, 237.

Wray, A. A. (1986) "Very low storage time-advancement shemes," Internal Report, NASA-Ames Research Center.

Wu, J. L. (1989) "Instabilities of a compressible mixing layer," Ph.D dissertation, Virginia Polytechnic Institute and State University, November.

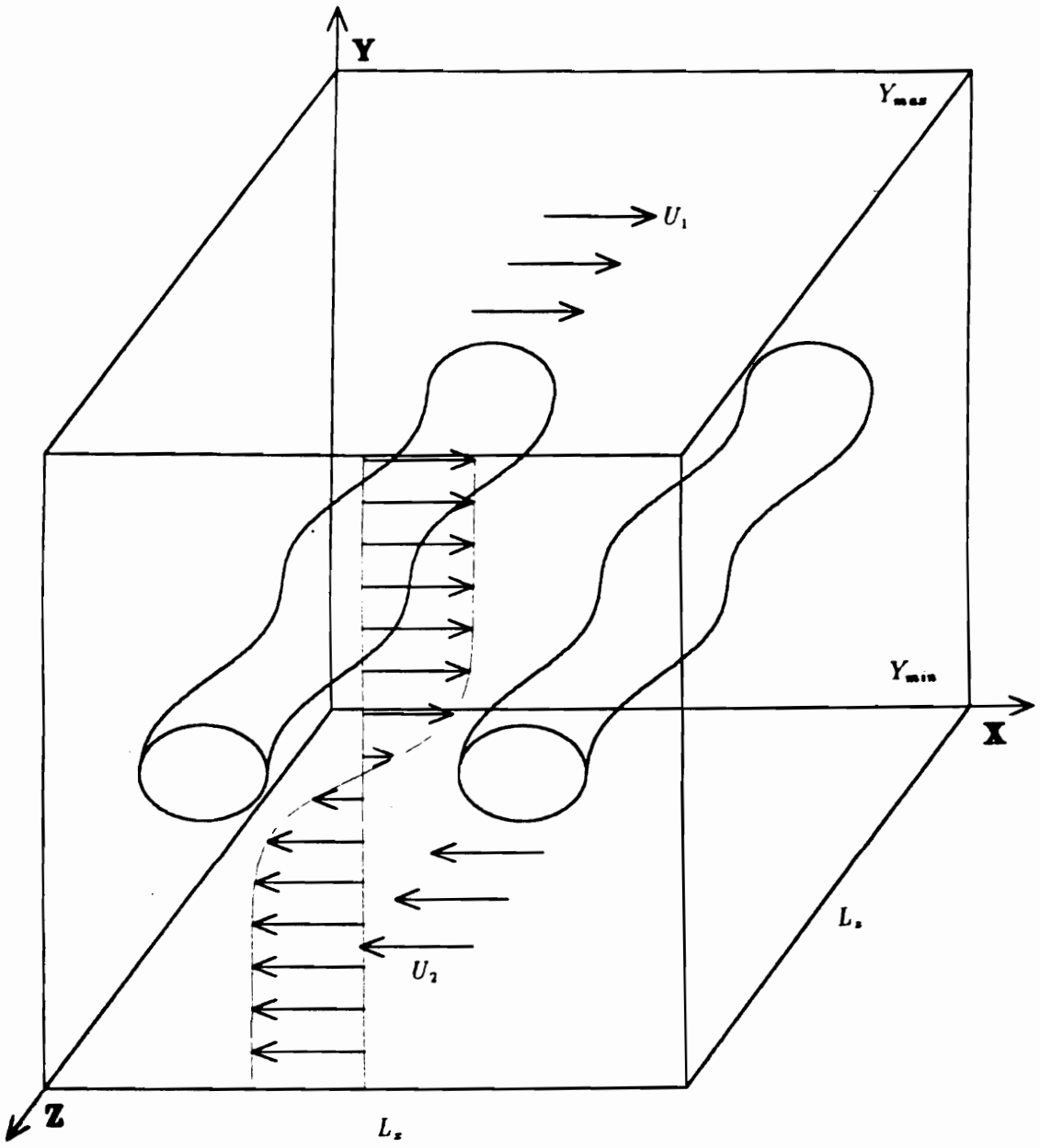

Fig. 3.1 Computational box for a temporally developing mixing layer.

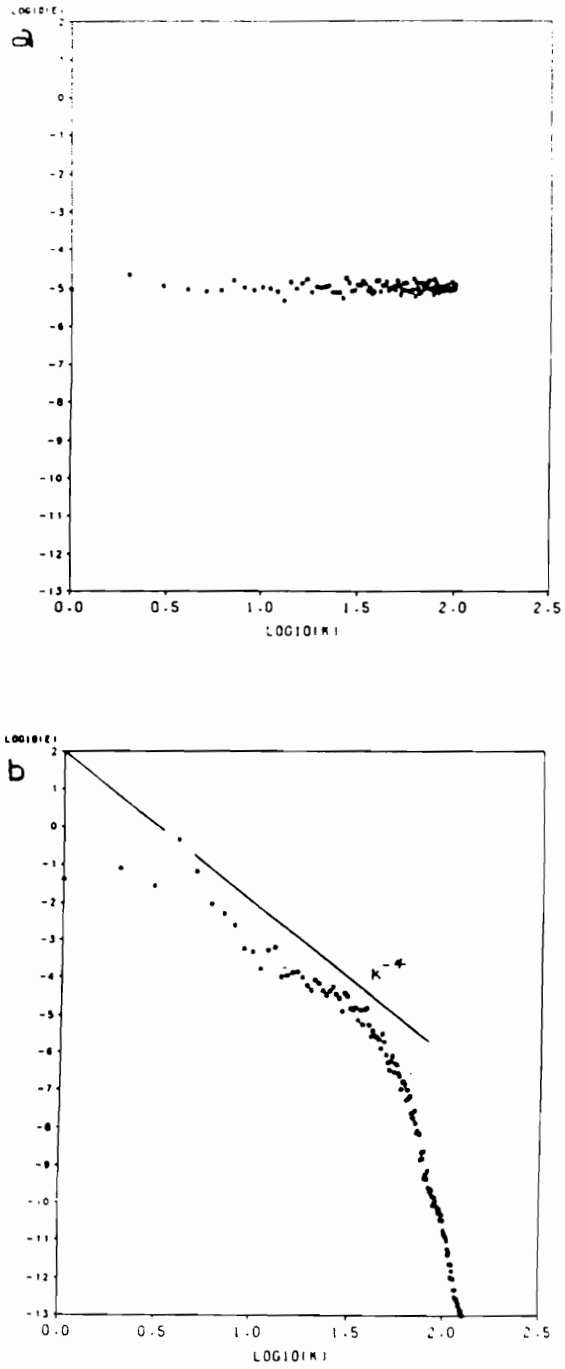

Fig. 4.1 One-dimensional energy spectra of a 2-D mixing layer, $M^+ = 0.4$, T_2/T_1=1; (a) time = 0, (b) time = 51.2, (c) time = 83.2, (d) time = 128.

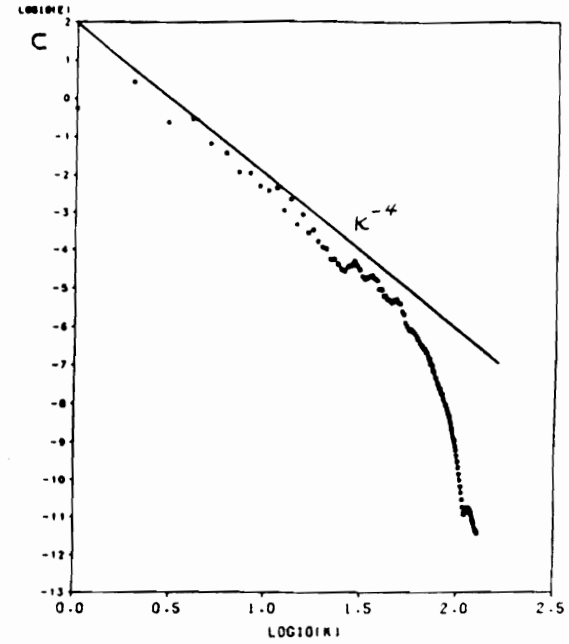

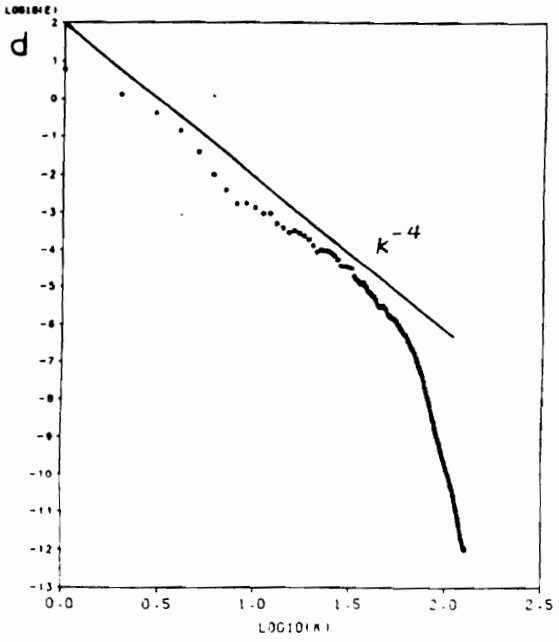

Fig. 4.1 (continued)

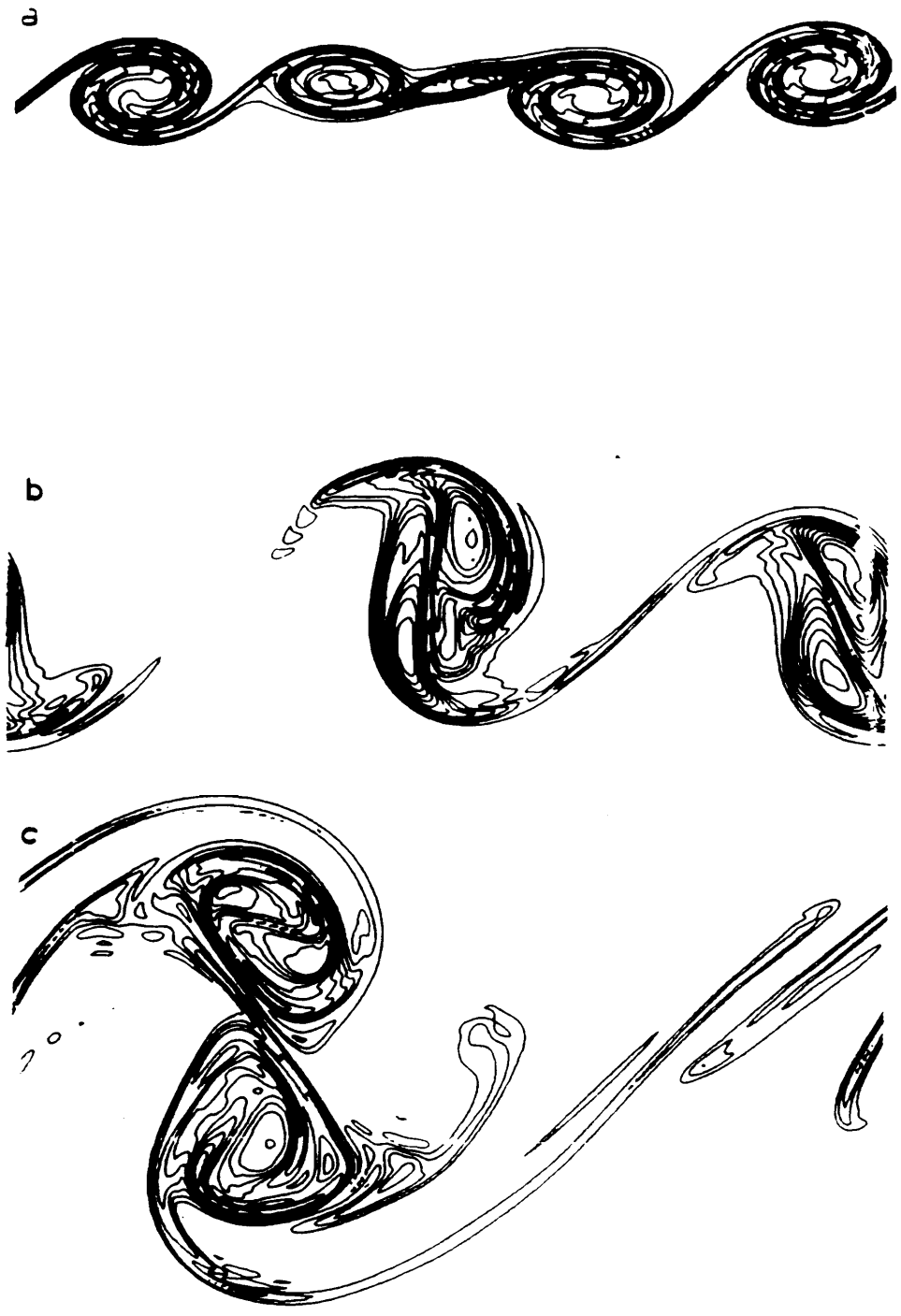

Fig. 4.2 Vorticity contours, (a) time = 51.2, (b) time = 83.2, (c) time = 128.

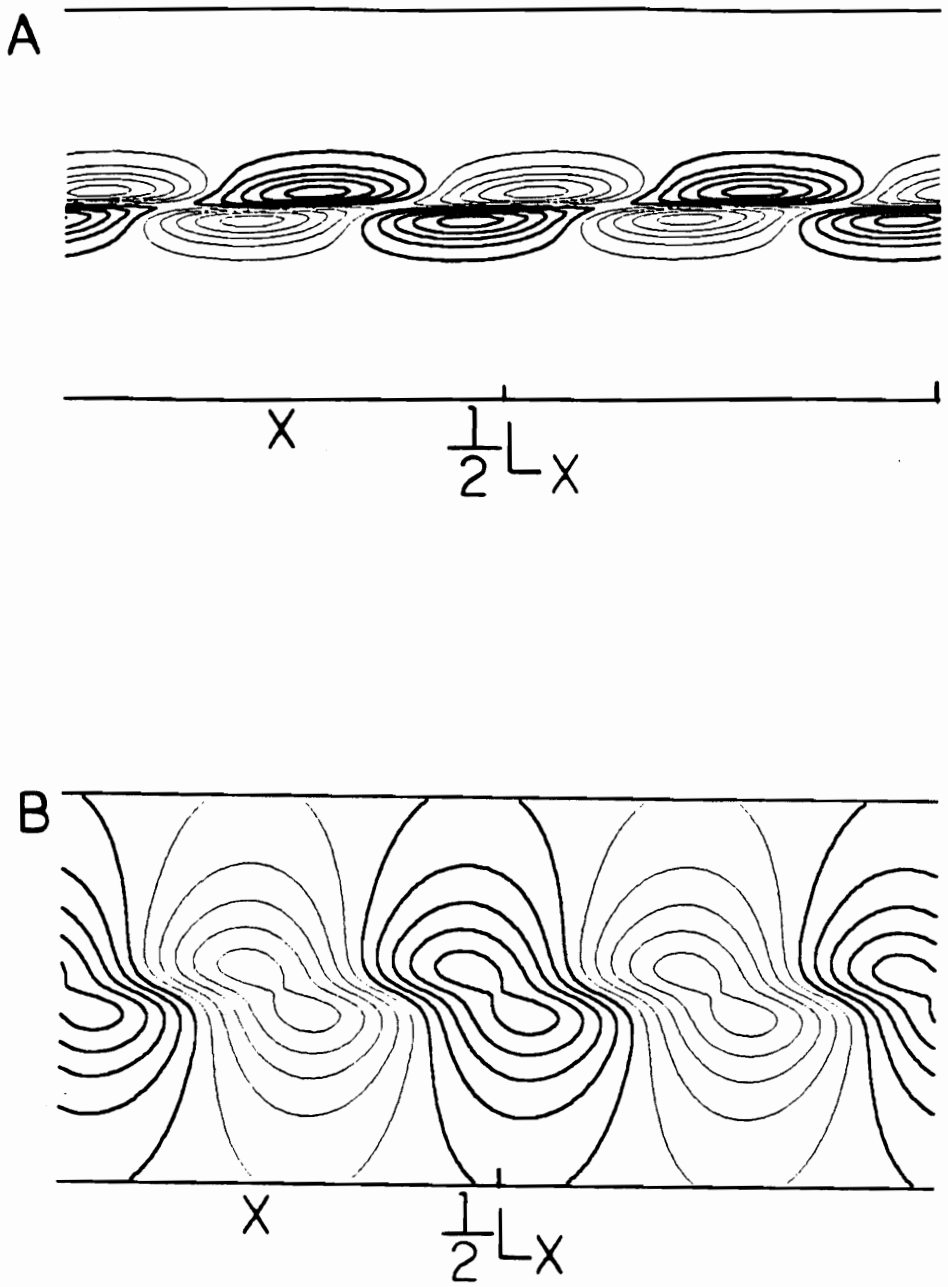

Fig. 5.1 (A) Spanwise vorticity (ω_z), and (B) transverse velocity (v), contours of the (2, 0) mode in the $x-y$ plane. Negative values are shown by thick lines.

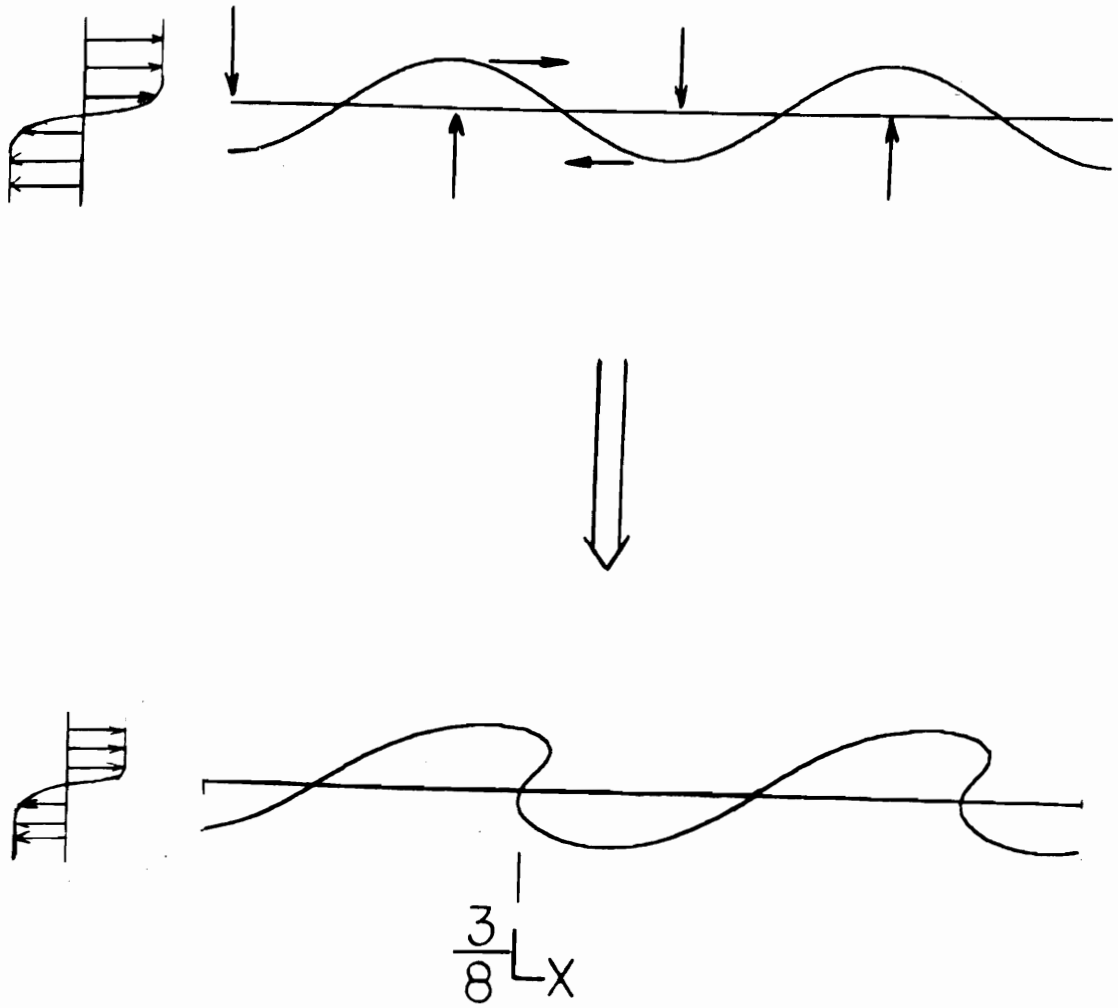

Fig. 5.2 The formation of the K-H vortices by the v-perturbations of the (2, 0) mode.

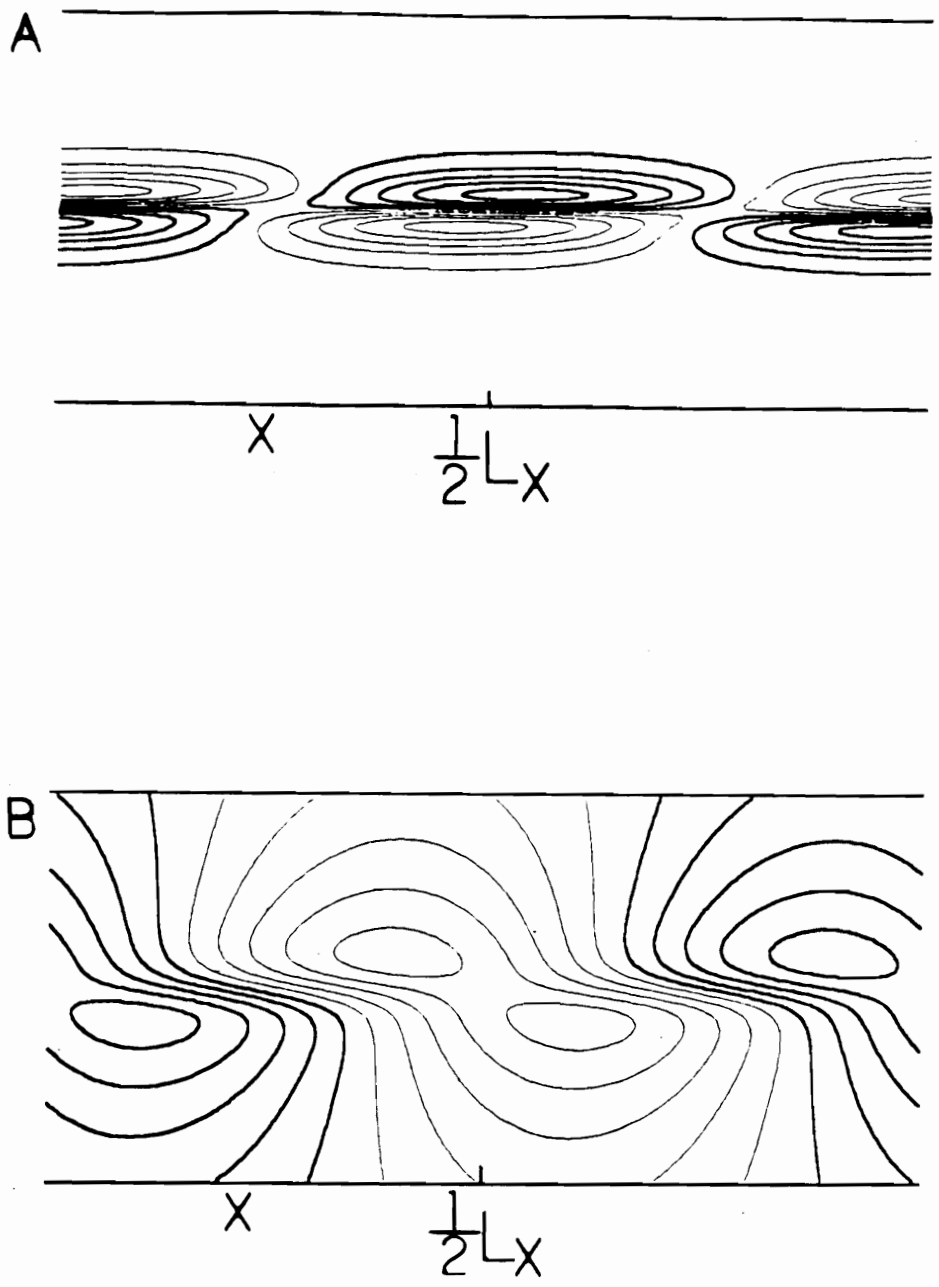

Fig. 5.3 (A) ω_z, and (B) v contours of the (1, 0) mode in the $x-y$ plane. Negative values are shown by thick lines, (C) locations of K-H vortices and saddle points of the (1,0) and (2,0) modes, phase difference = $\pi/2$.

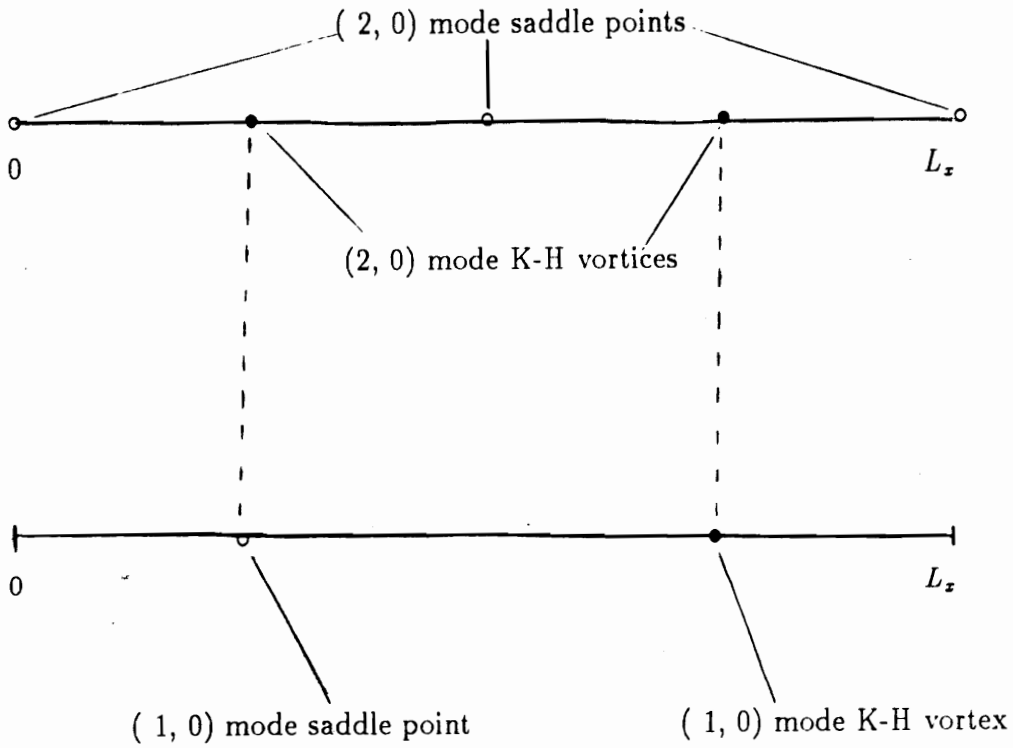

C

Fig. 5.3 (continued)

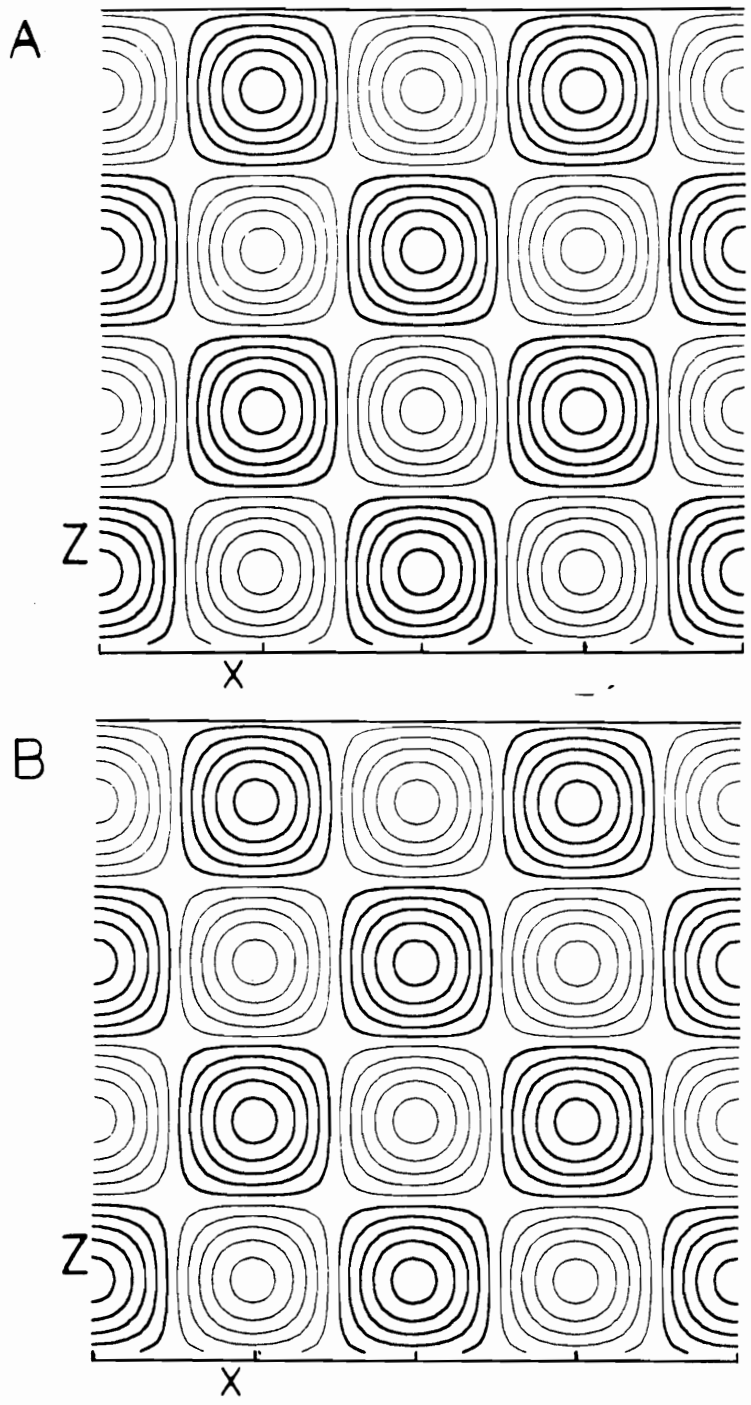

Fig. 5.4 (A) ω_x, and (B) ω_y contours of the (2, 2) mode in the interface $x-z$ plane. Negative values are shown by thick lines.

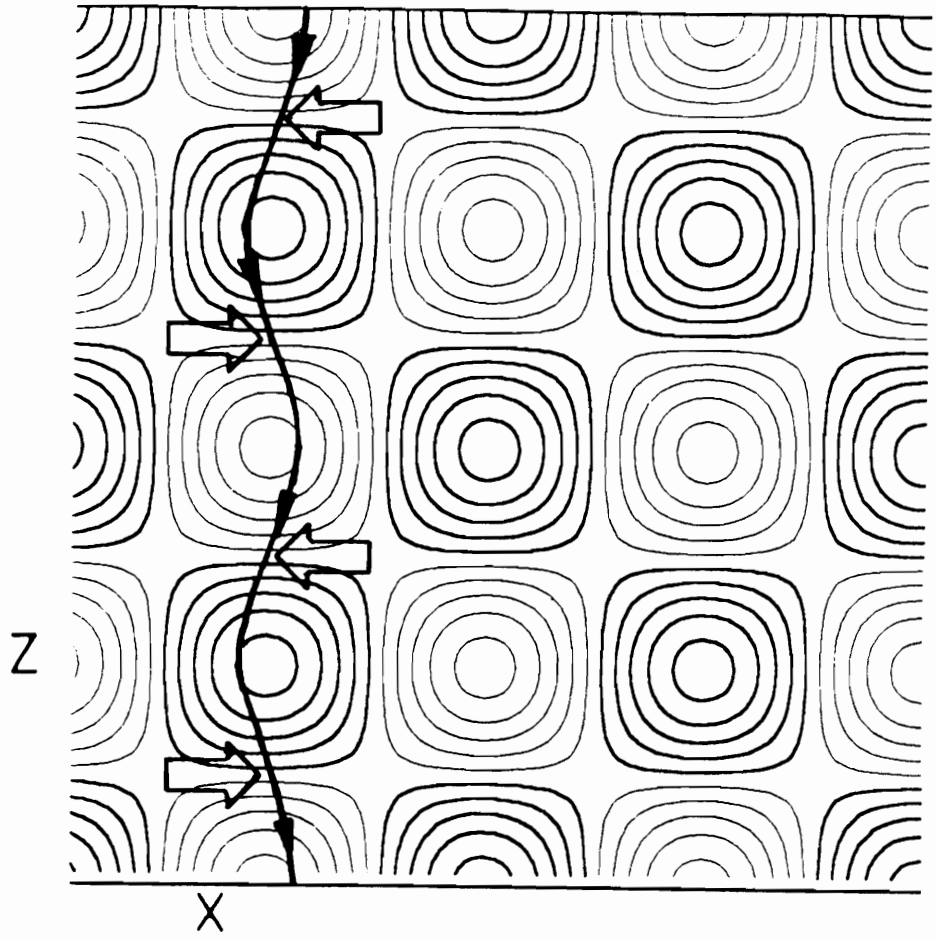

Fig. 5.5 Contours of the v-perturbations of the (2, 2) mode on the interface and the predicted undulation of the vortex line at $x = 1/4L_x$. Negative values are shown by thick lines.

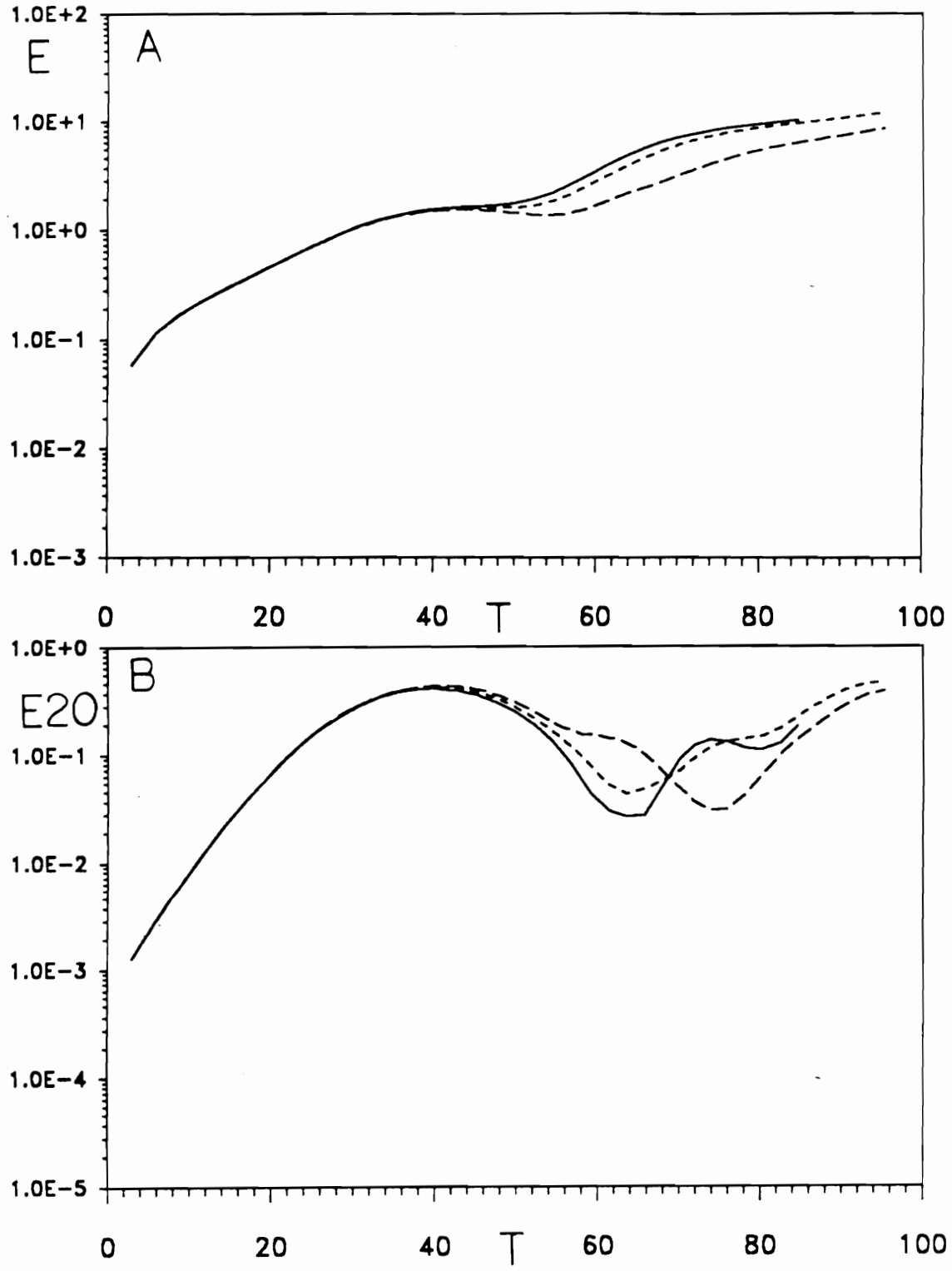

Fig. 5.6 Growth of modal energy. (A) $E^{\circ}_{00} - E_{00}$, (B) E_{20}, (C) E_{02}, (D) E_{22}. $A_{20} = 0.02, A_{22} = 0.02$. $\phi_{22} = 0$, — ; $\phi_{22} = \pi/4$, - - - ; $\phi_{22} = \pi/2$, – – –.

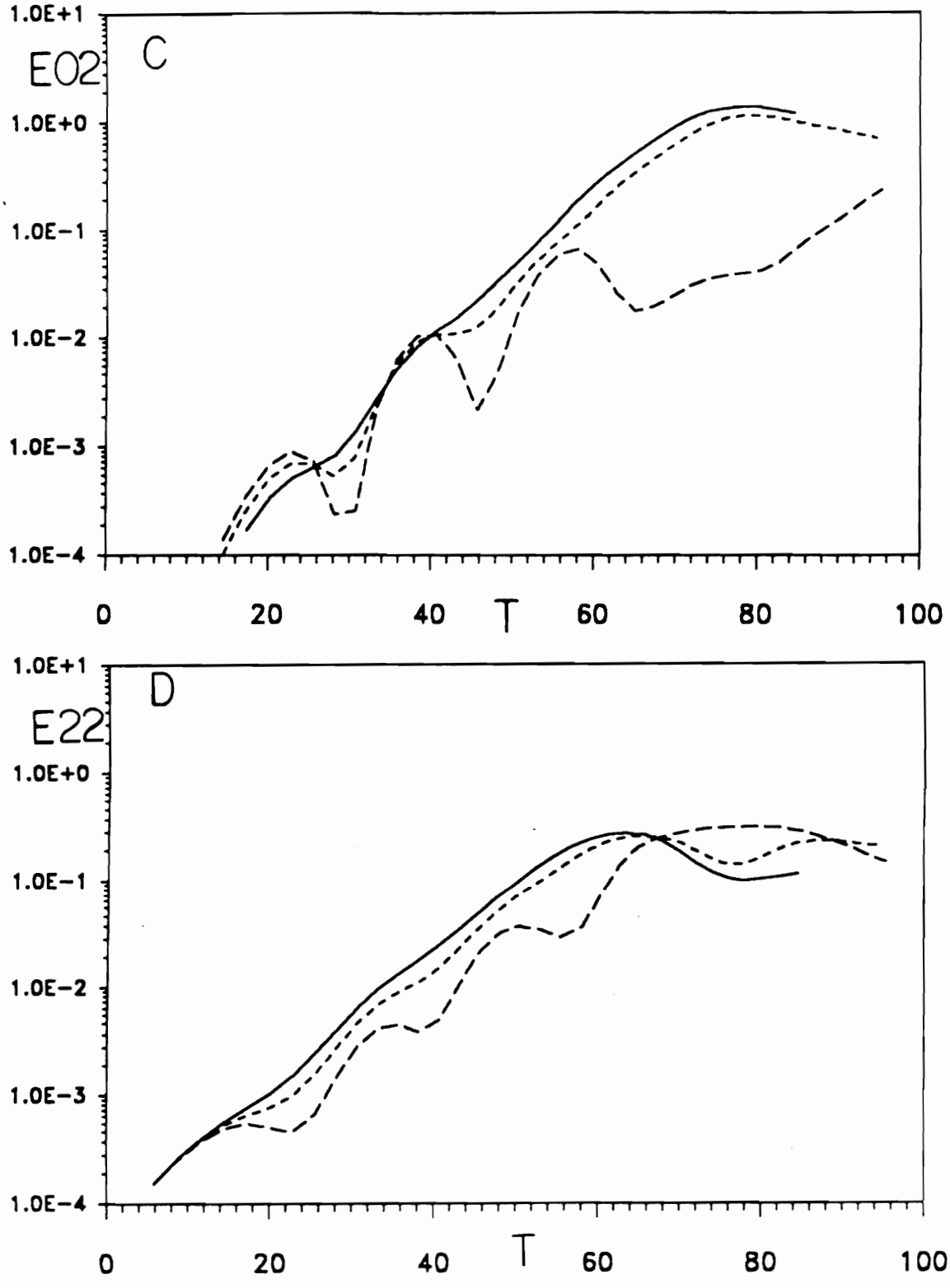

Fig. 5.6 (continued)

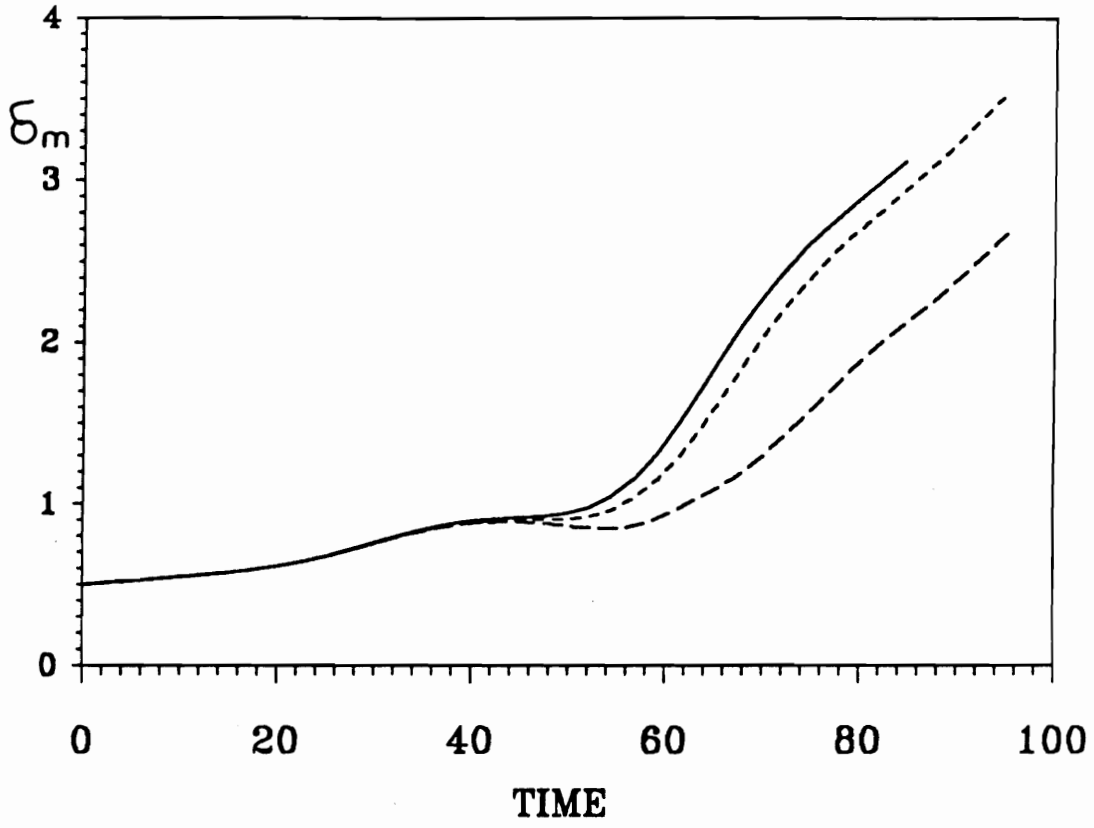

Fig. 5.7 Growth of momentum thickness. $A_{20} = 0.02, A_{22} = 0.02$. $\phi_{22} = 0$, — ; $\phi_{22} = \pi/4$, - - - ; $\phi_{22} = \pi/2$, – – –.

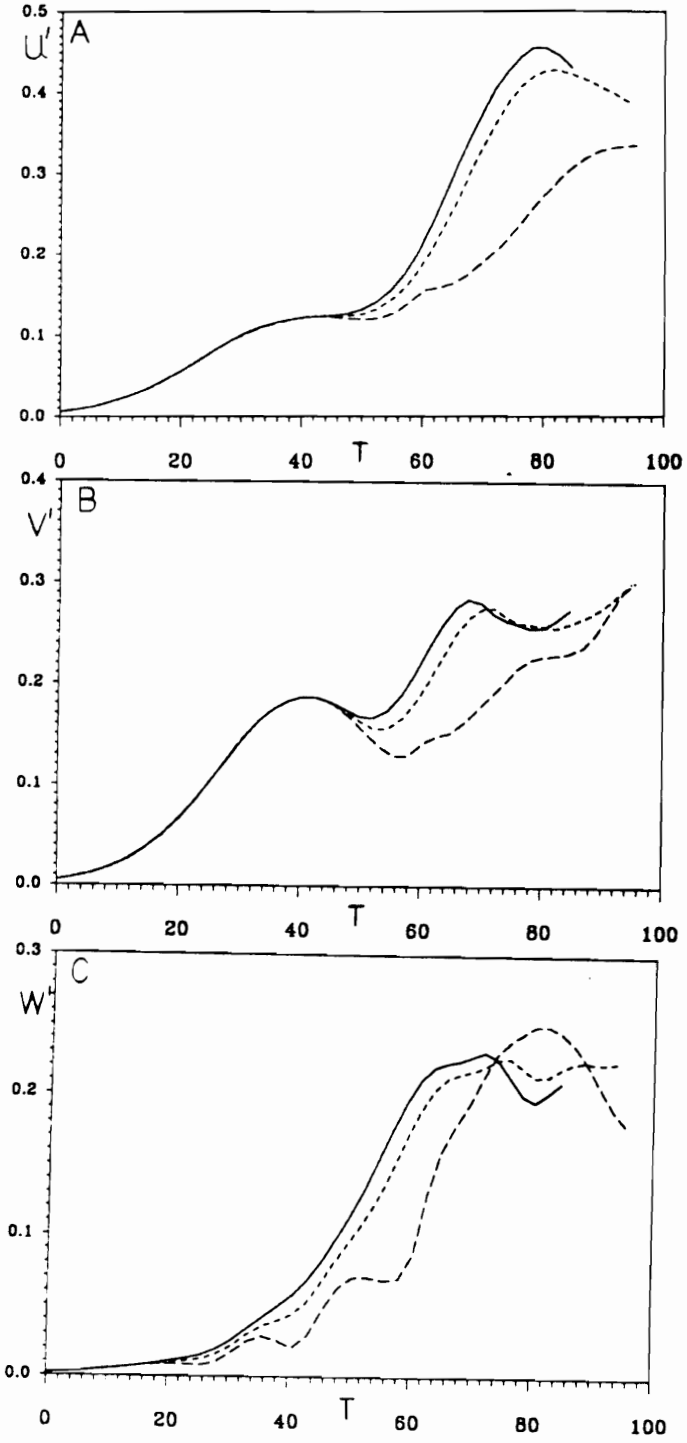

Fig. 5.8 Growth of (A) u', (B) v', and (C) w'. $A_{20} = 0.02, A_{22} = 0.02$. $\phi_{22} = 0$, — ; $\phi_{22} = \pi/4$, - - - ; $\phi_{22} = \pi/2$, – – –.

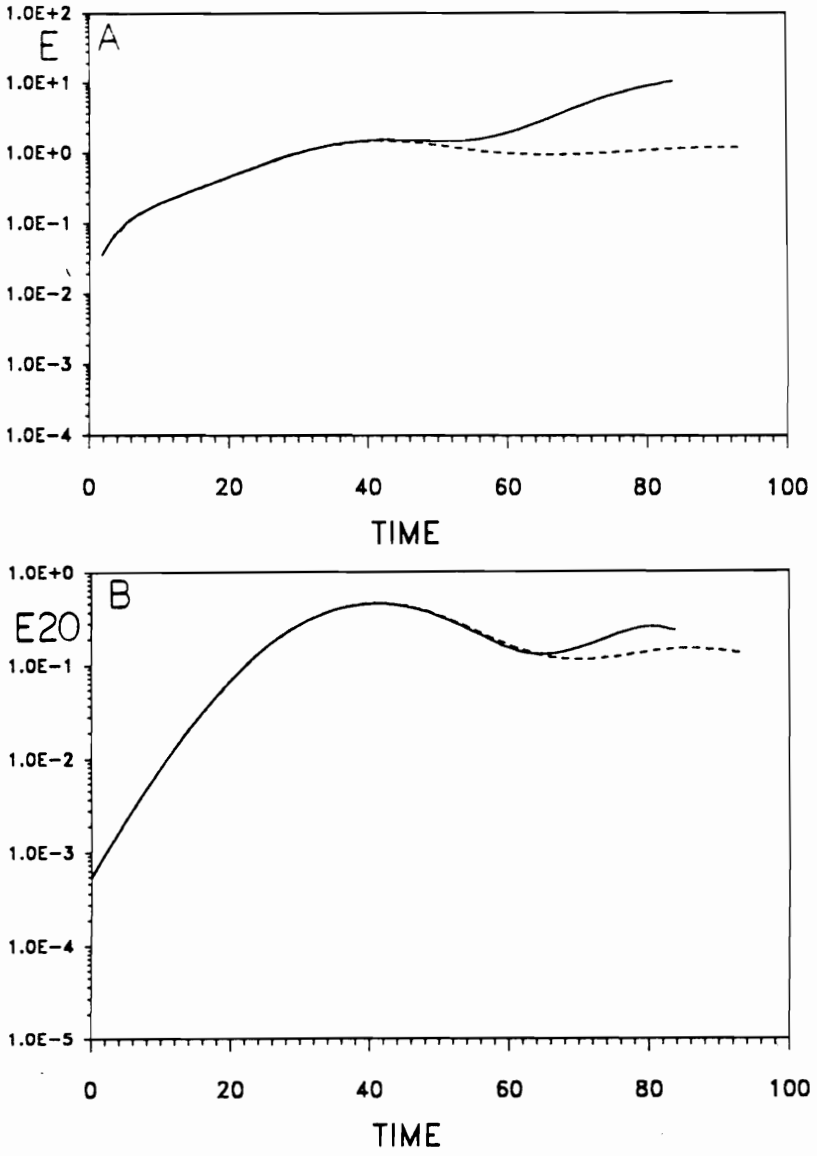

Fig. 5.9 Growth of modal energy. (A) $E^{\circ}_{00} - E_{00}$; (B) E_{20}; (C) E_{11}; (D) E_{02}. $A_{20} = 0.02, A_{11} = 0.005$. $\phi_{11} = \pi/2$, — ; $\phi_{11} = \pi$, - - -.

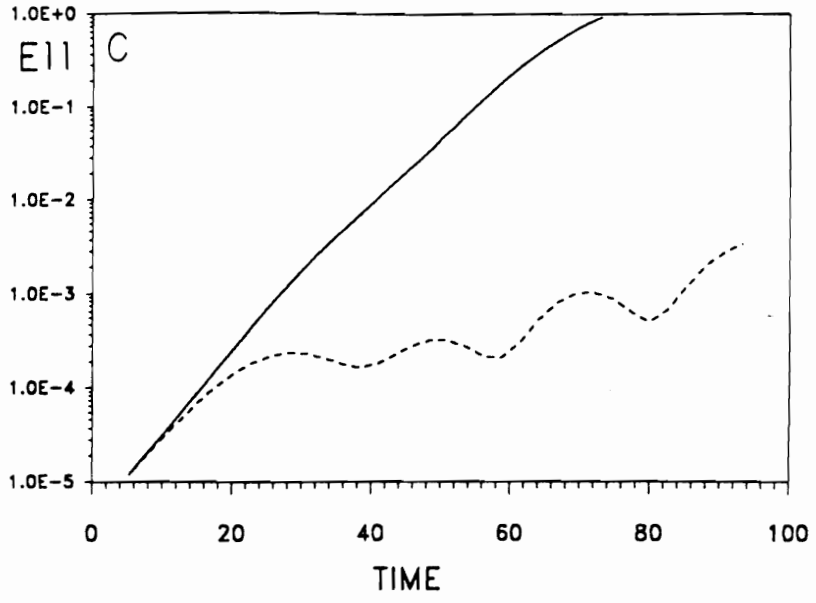

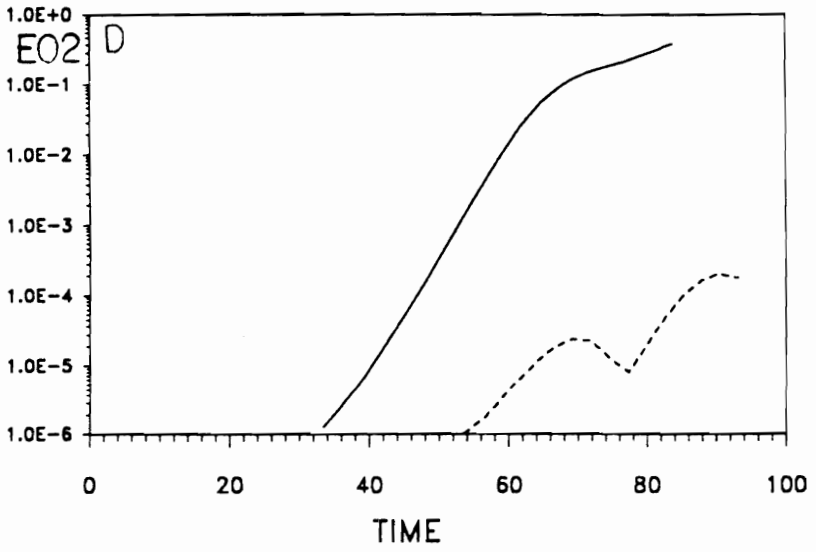

Fig. 5.9 (continued)

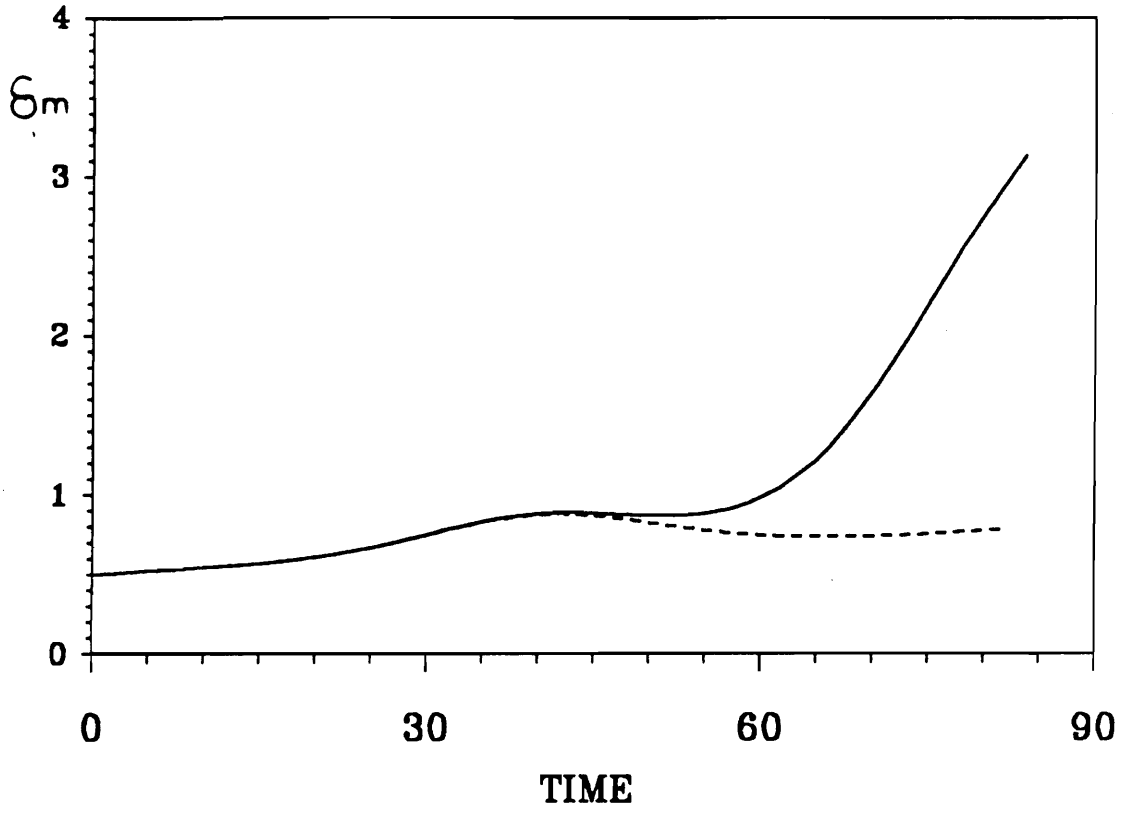

Fig. 5.10 Growth of momentum thickness. $A_{20} = 0.02, A_{11} = 0.005$. $\phi_{11} = \pi/2$, —; $\phi_{11} = \pi$, - - -.

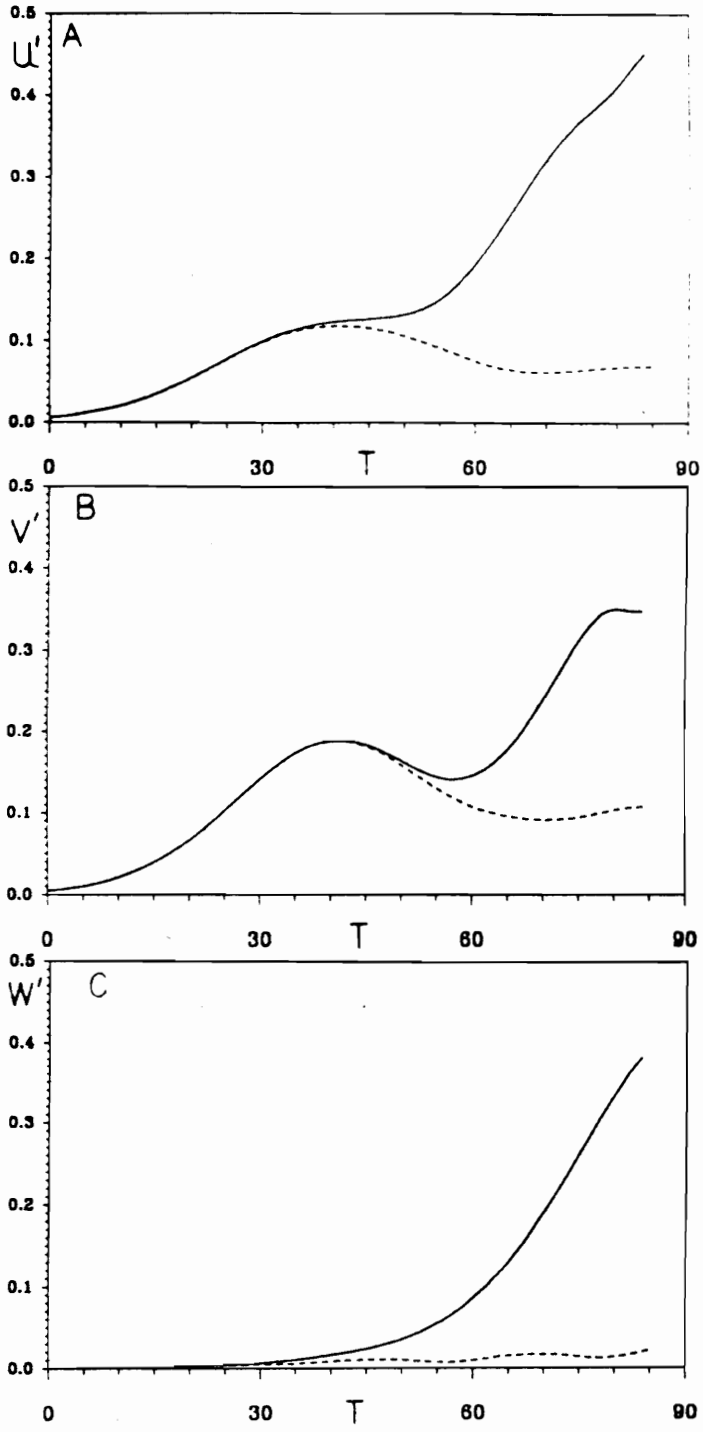

Fig. 5.11 Growth of (A) u', (B) v', and (C) w'. $A_{20} = 0.02, A_{11} = 0.005$. $\phi_{11} = \pi/2$, —; $\phi_{11} = \pi$, - - -.

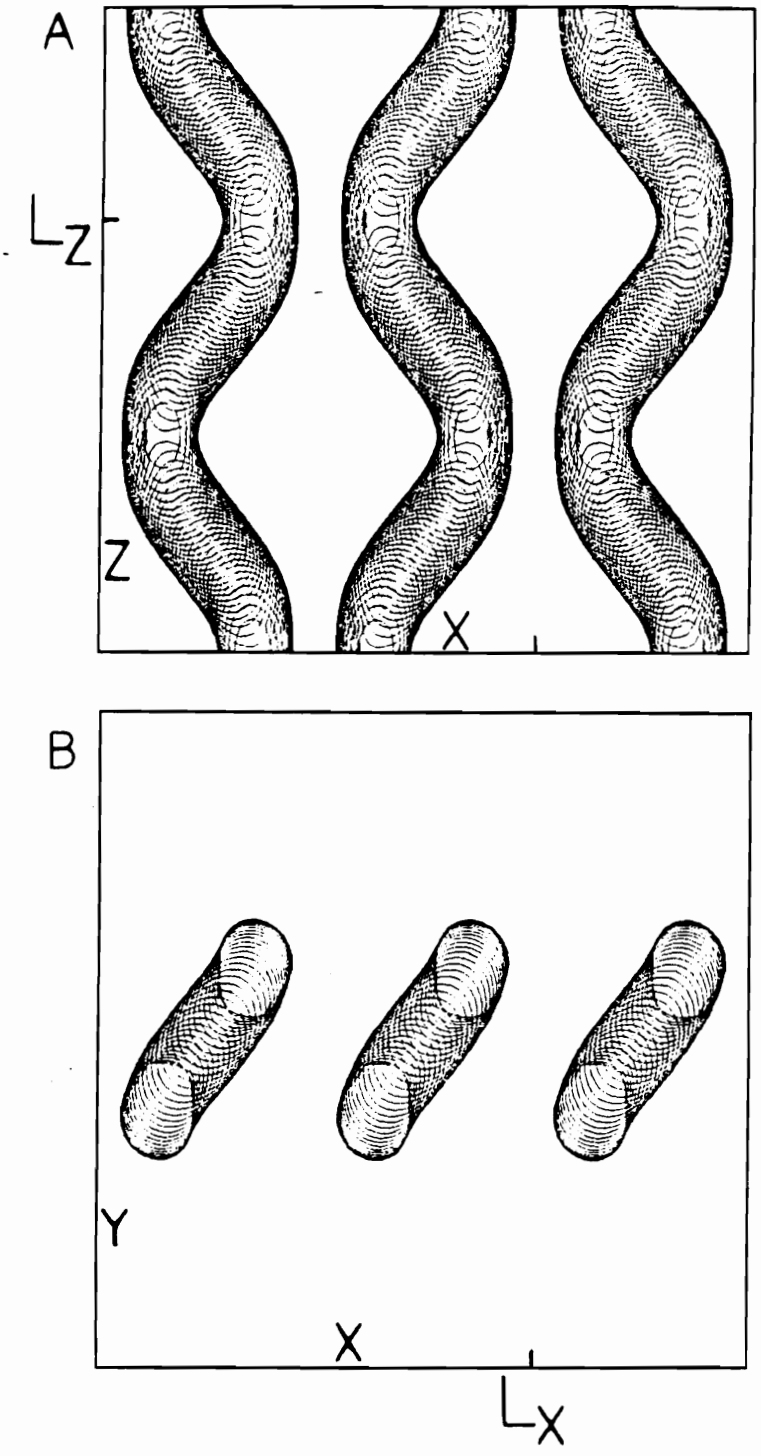

Fig. 5.12 Projections of low-pressure region in the simulation of helical pairing mode.

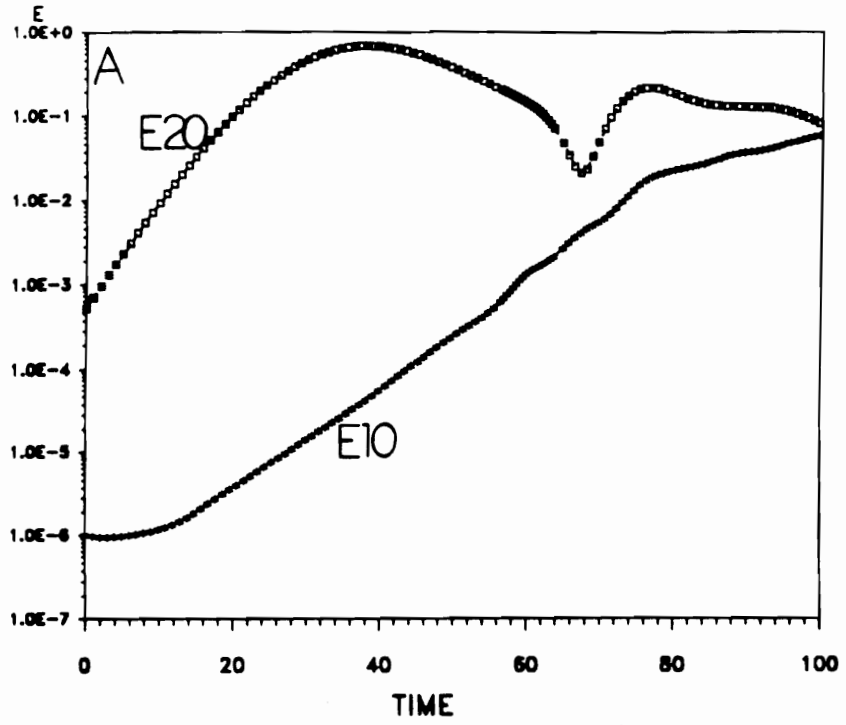

Fig. 6.1 Growth of modal energy; case A.

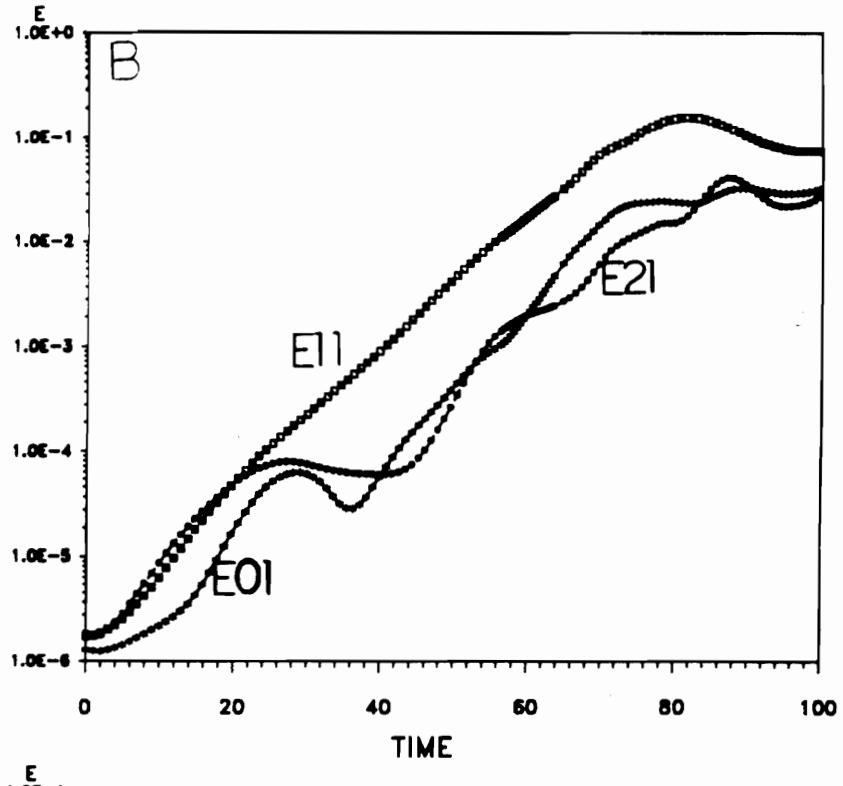

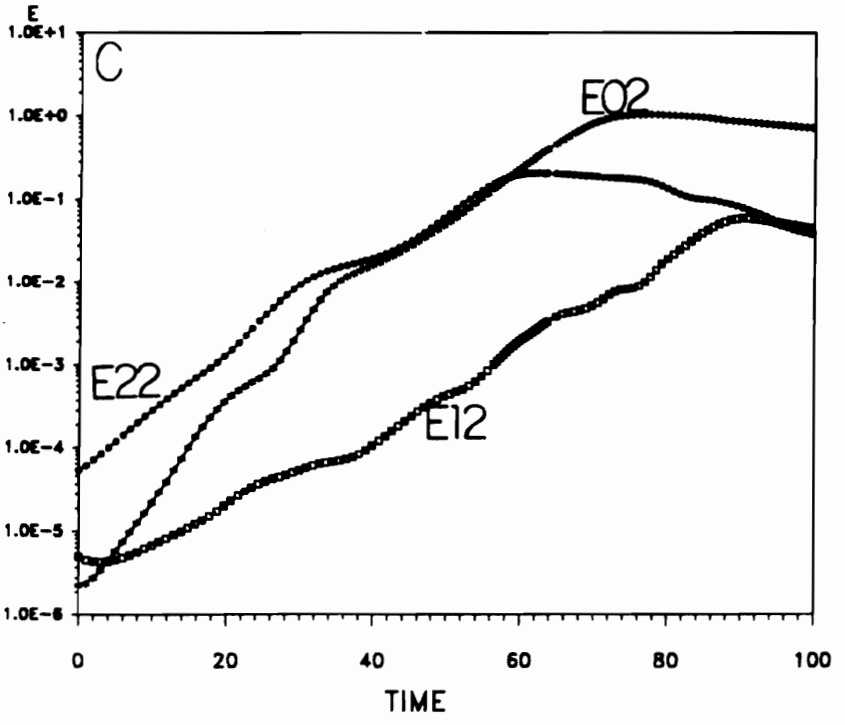

Fig. 6.1 (continued)

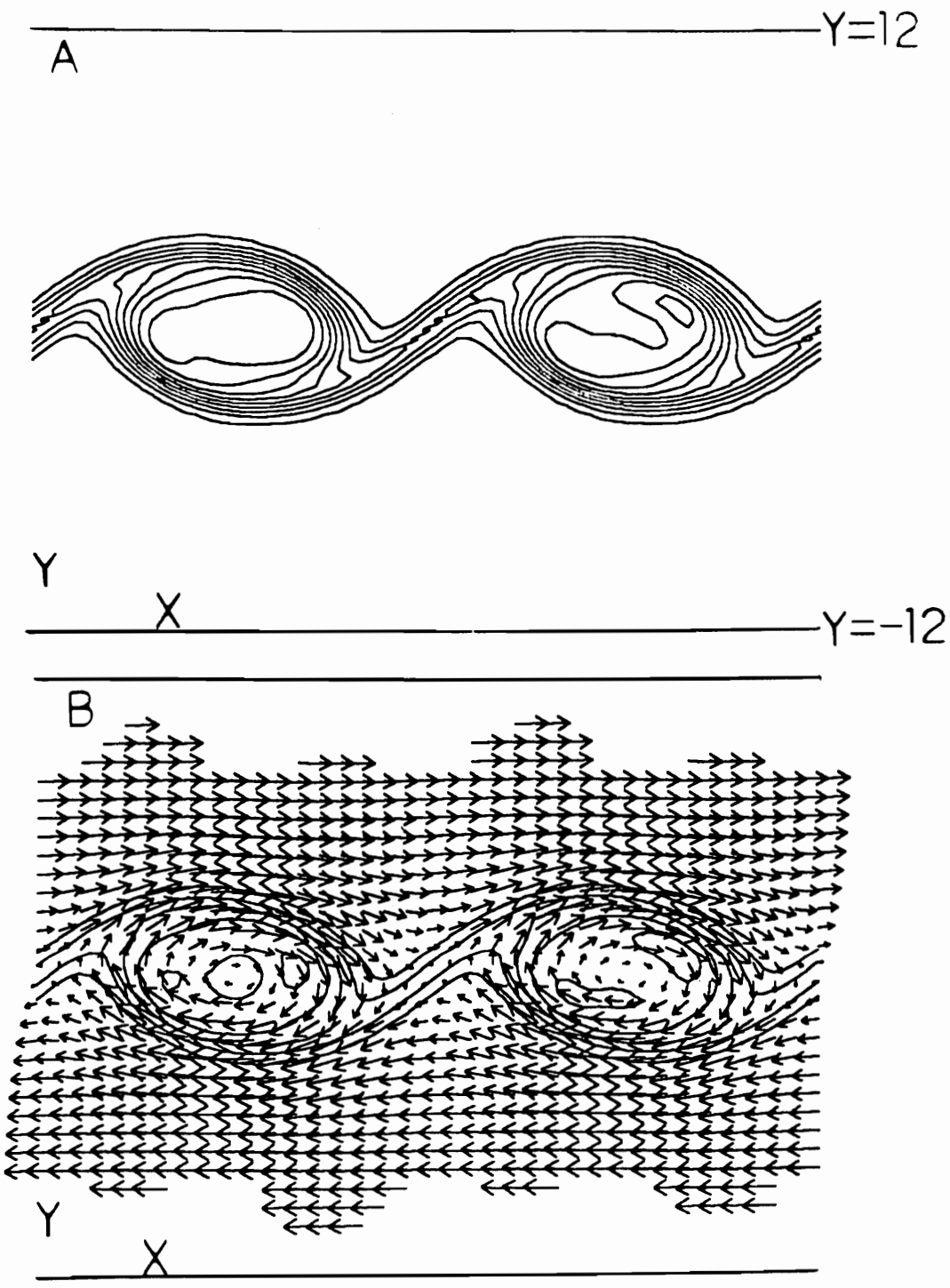

Fig. 6.2 (A) Contours of spanwise vorticity; $\omega_{max} = -0.039, \omega_{min} = -0.732, \Delta\omega = 0.077$, (B) velocity vectors. Case A, $t = 32.7$; $x - y$ plane, $z = 1/8L_z$.

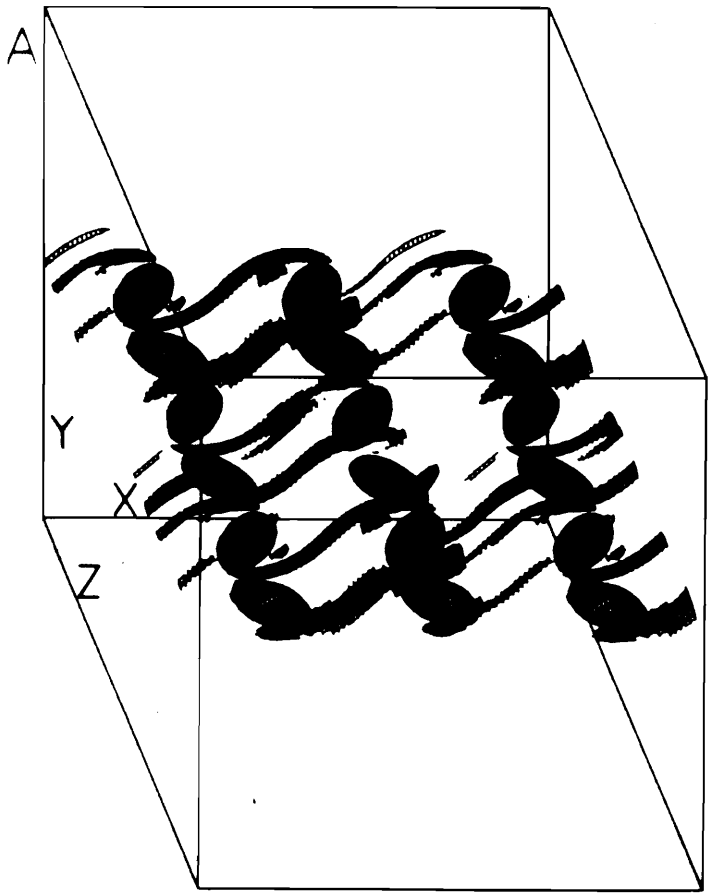

Fig. 6.3 Surface with constant $\omega_{xy}, \sqrt{\omega_x^2 + \omega_y^2}$; case A, $t = 40.8$; (A) perspective view, $\omega_{xy} = 0.25$, (B) projection on the $x - z$ plane, $\omega_{xy} = 0.22$, (C) projection on the $x - y$ plane, $\omega_{xy} = 0.22$.

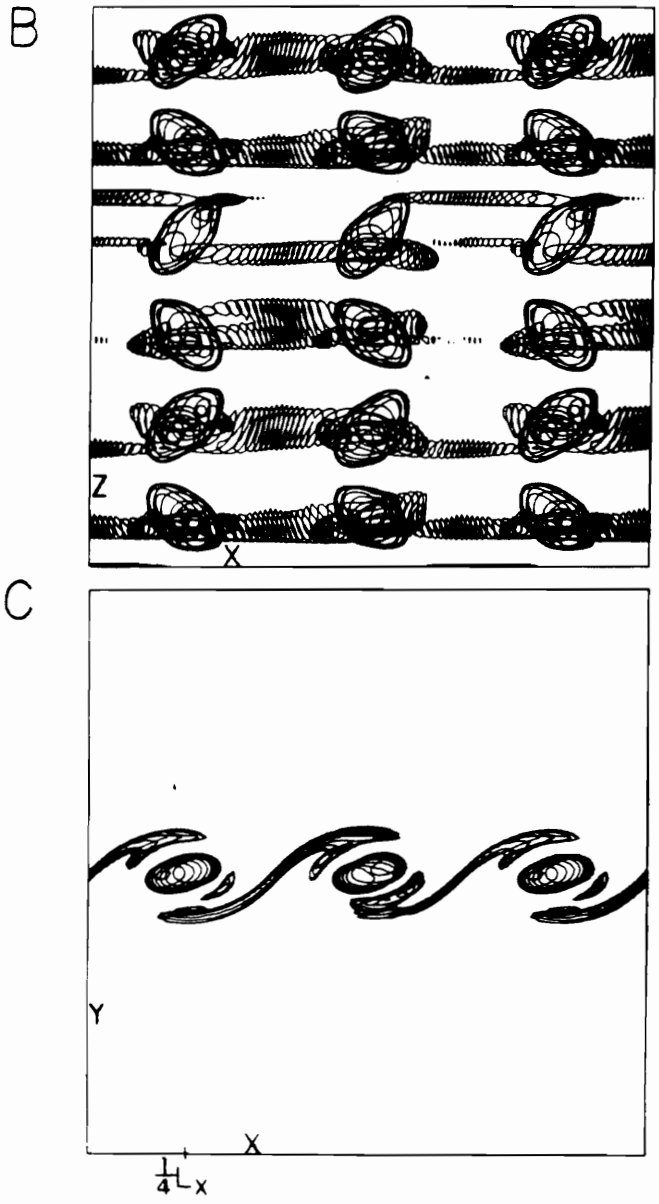

Fig. 6.3 (continued)

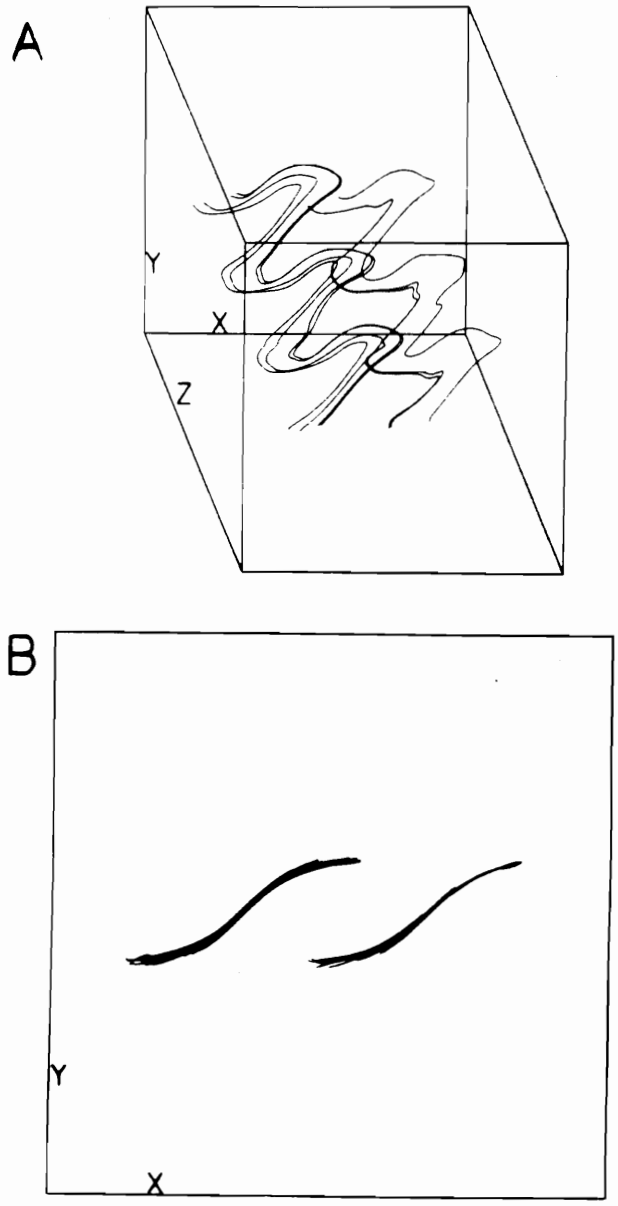

Fig. 6.4 Vortex lines through the streamwise vortex tubes; case A, $t = 40.8$; (A) perspective view, (B) projection on the $x - y$ plane.

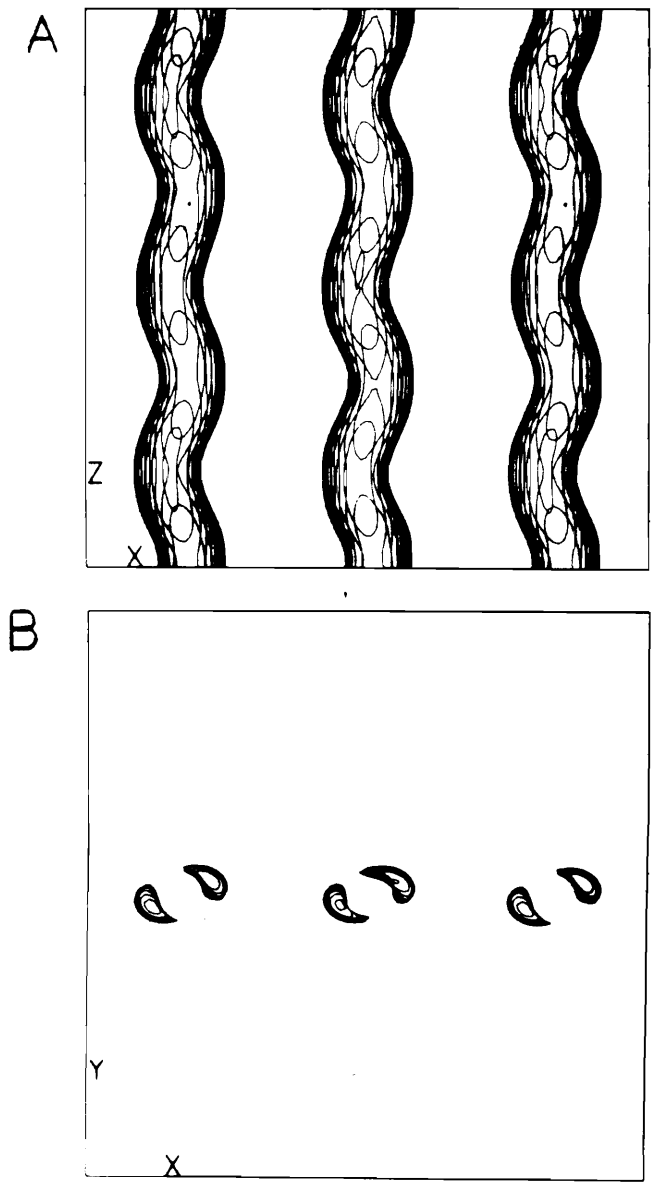

Fig. 6.5 Surface with constant (A) pressure, $P/(\rho_1 RT_1) = 0.9$, projection on the $x - z$ plane, (B) spanwise vorticity, $\omega_z = -0.85$, projection on the $x - y$ plane; case A, $t = 40.8$.

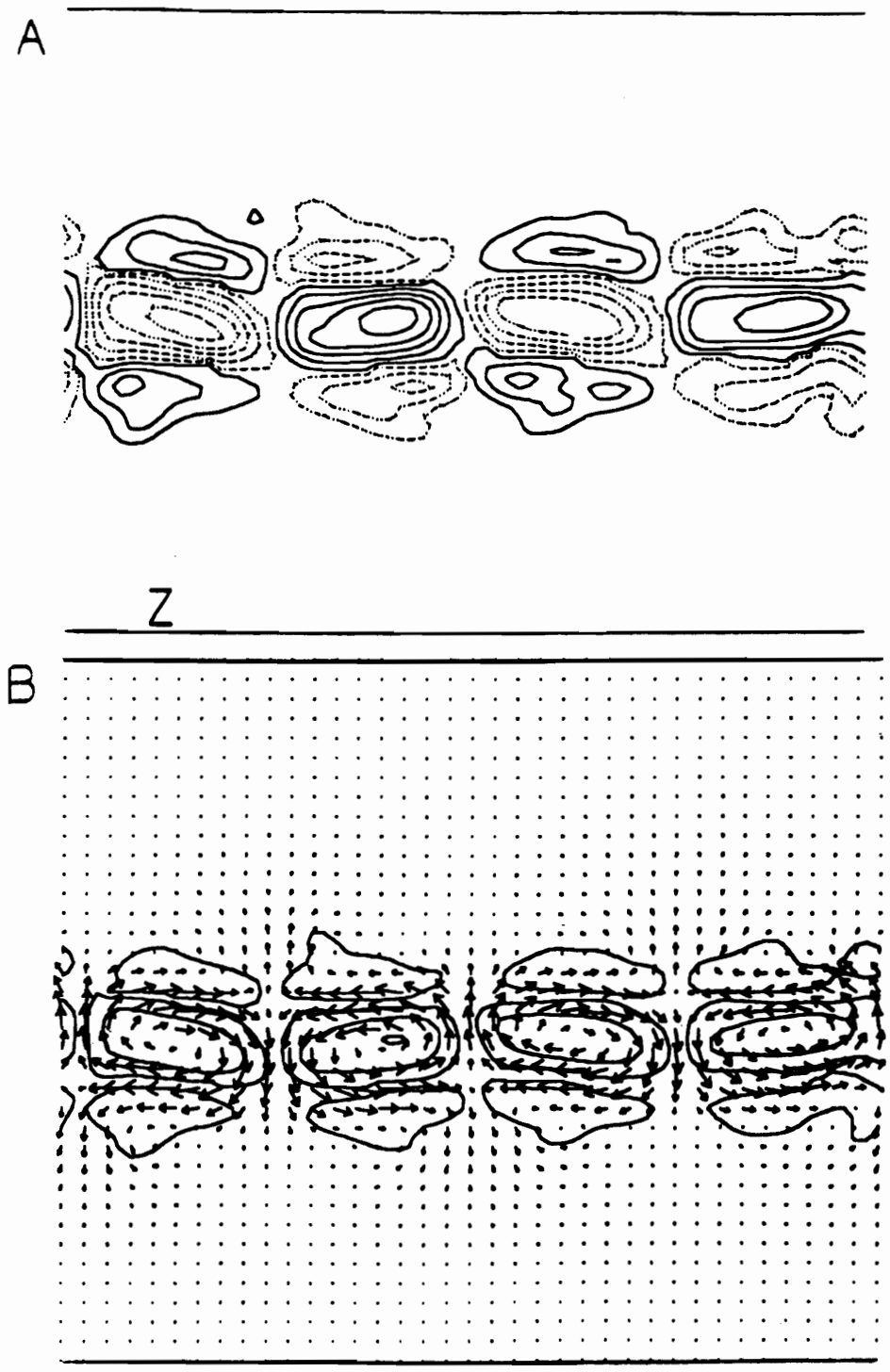

Fig. 6.6 (A) contours of ω_{xy} with the sign of ω_z, $\omega_{max} = 0.689$, $\omega_{min} = -0.689$, negative values are shown by solid lines, (B) velocity vectors; case A, $t = 48.7$; $z - y$ plane, $x = 1/4L_x$; plots are truncated at $y = \pm 12$.

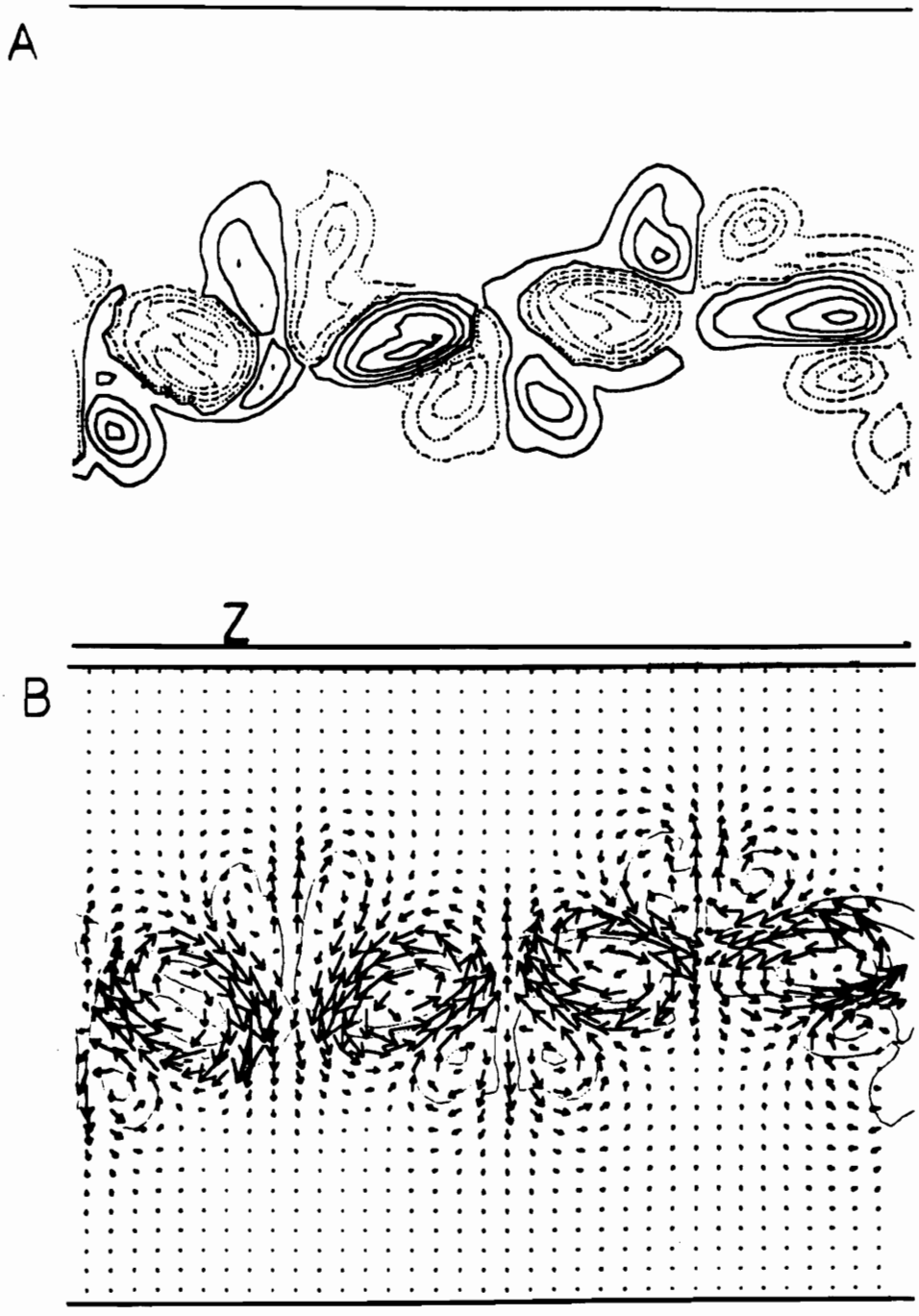

Fig. 6.7 (A) contours of ω_{xy} with the sign of ω_x, $\omega_{max} = 1.418$, $\omega_{min} = -1.418$, negative values are shown by solid lines, (B) velocity vectors; case A, $t = 64.0$; $z - y$ plane, $x = 1/4L_x$; plots are truncated at $y = \pm 12$.

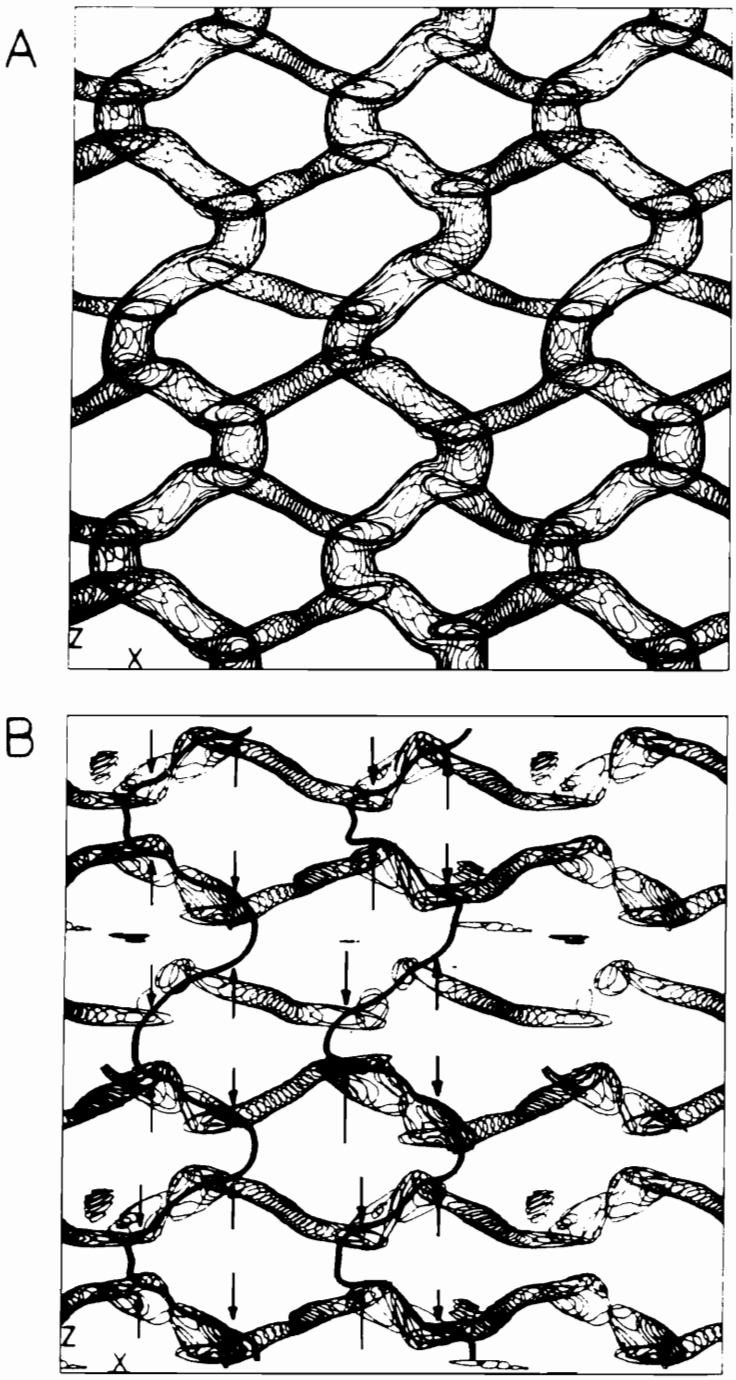

Fig. 6.8 Projections of vortex structures on the $x - z$ plane; $t = 64.0$, case A; (A) $P/(\rho_1 RT_1) = 0.91$, (B) $\omega_{xy} = 1.250$.

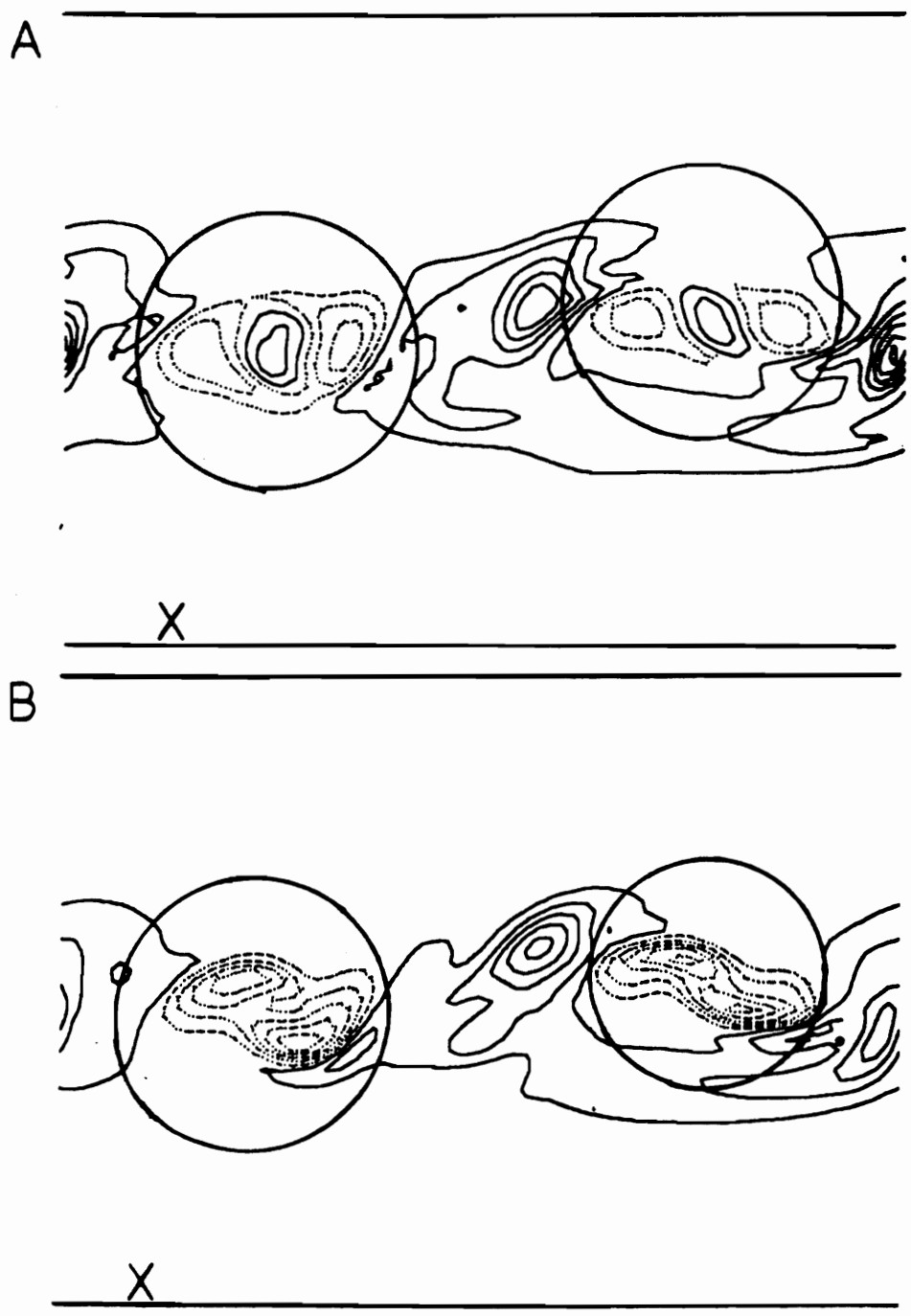

Fig. 6.9 (A) Contours of ω_y; $\omega_{max} = 0.873$, $\omega_{min} = -2.269$, (B) Contours of ω_z; $\omega_{max} = 1.517$, $\omega_{min} = -1.517$; in the $x - y$ plane at $z = 1/8L_z$; negative values are shown by solid lines, plots are truncated at $y = \pm 12$. (C) projection of K-H vortex tube vortex lines on the $x - y$ plane; $t = 64.0$, case A.

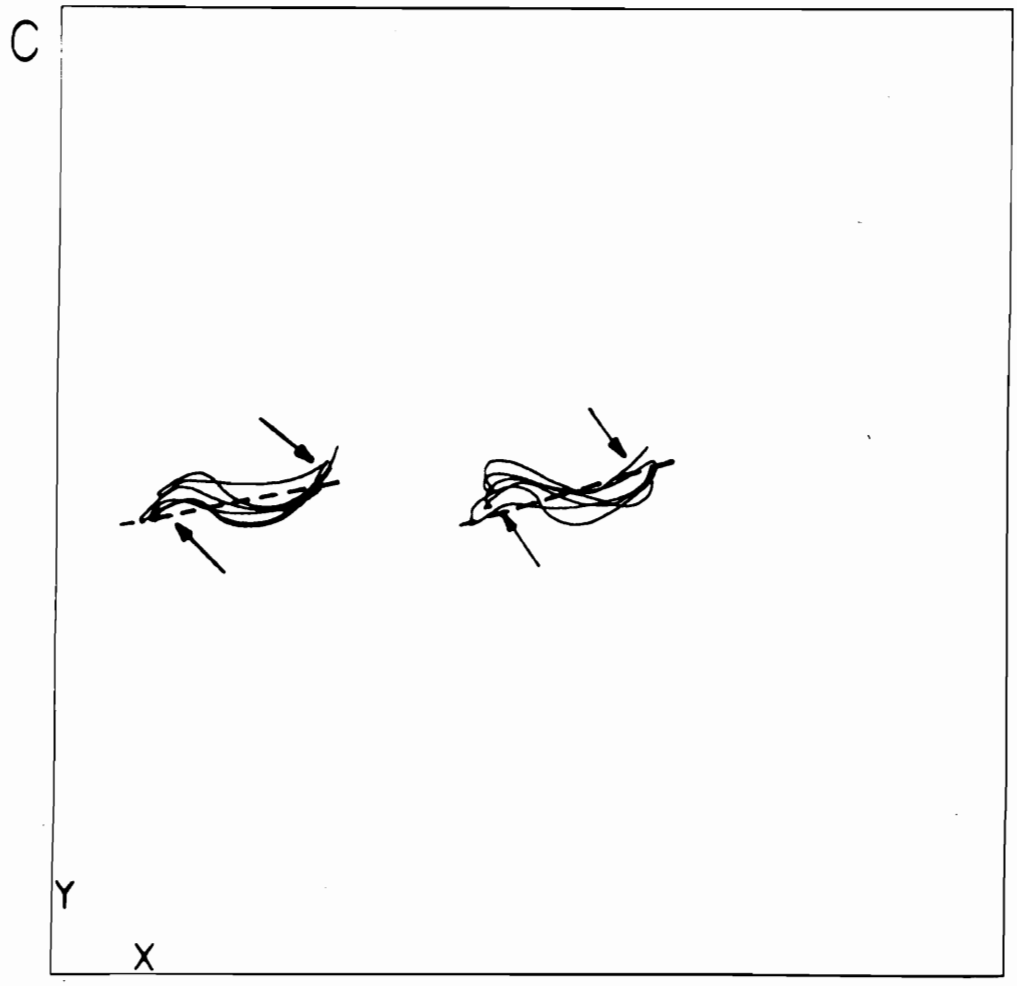

Fig. 6.9 (continued)

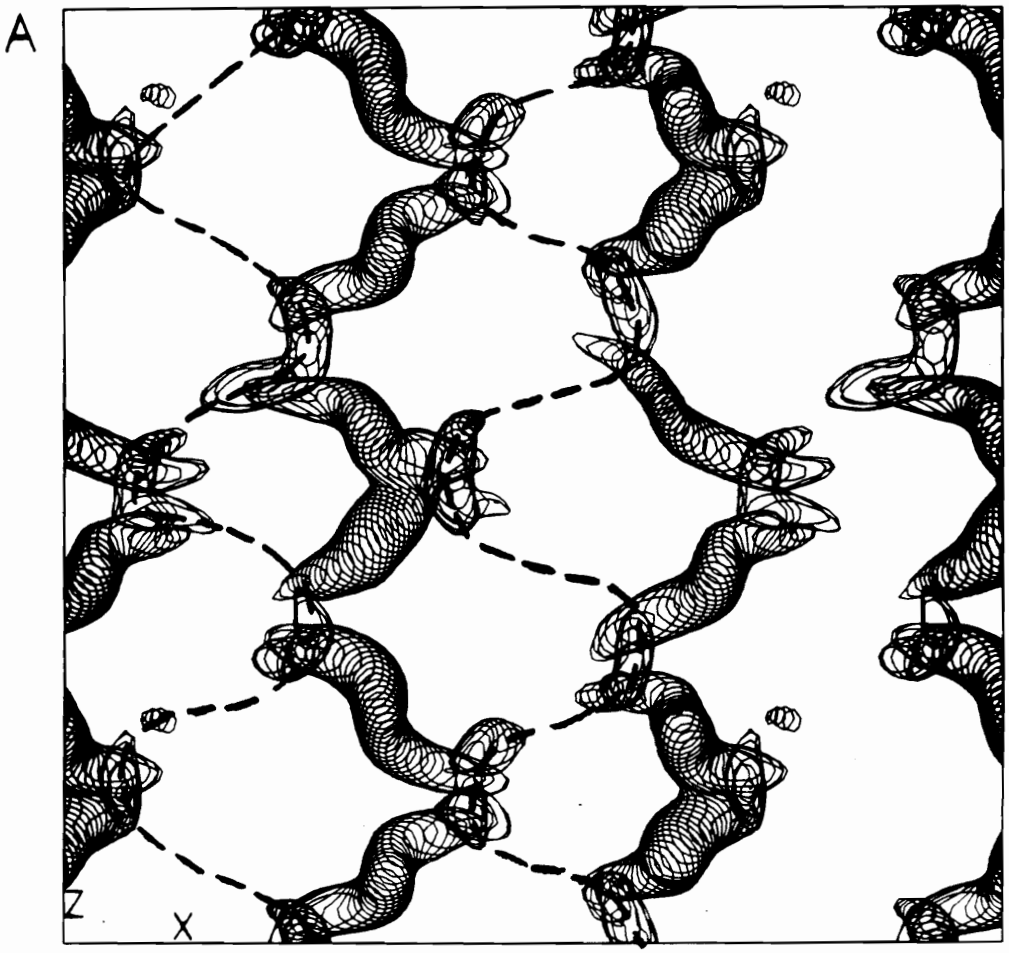

Fig. 6.10 Projections of large structures on the $x - z$ plane; case A, $t = 71.3$; (A) $P/(\rho_1 RT_1) = 0.88$, (B) $\omega_{xy} = 1.35$, (C) $\omega_z = -1.2$.

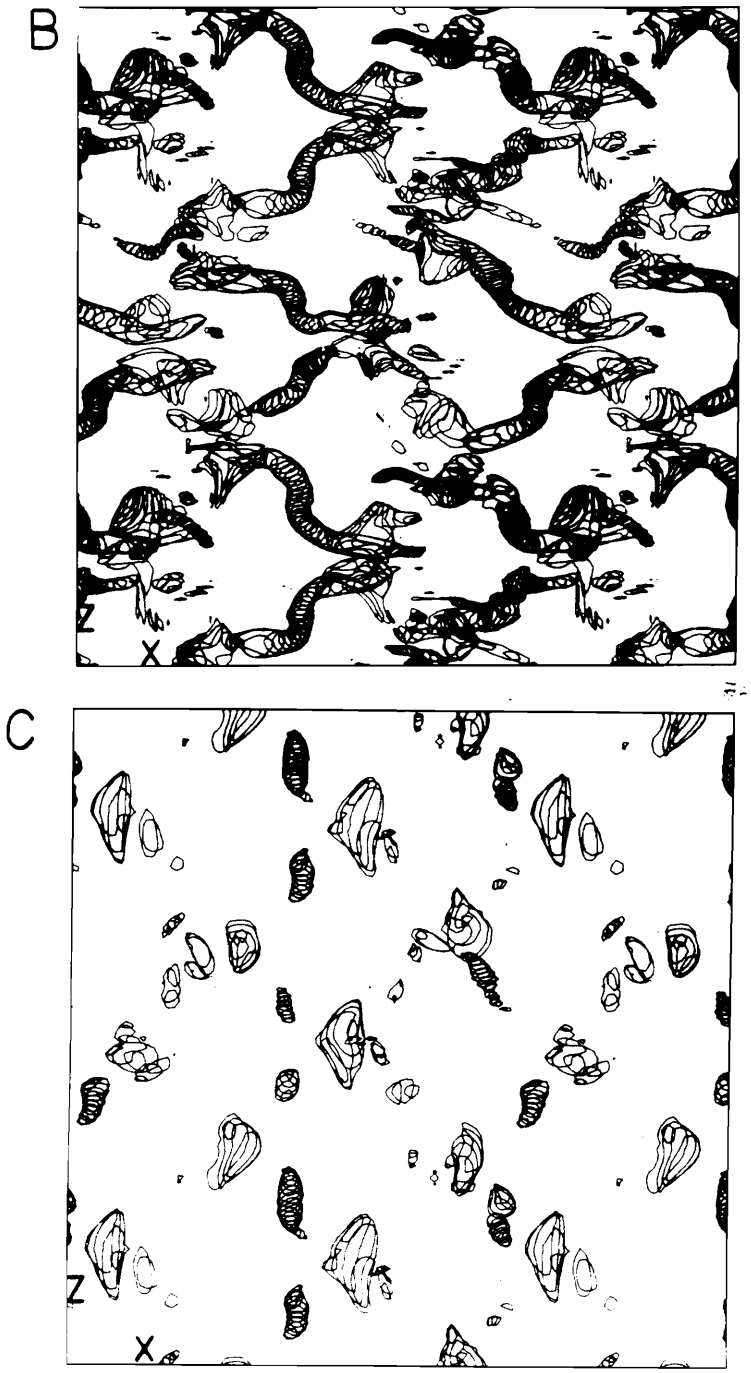

Fig. 6.10 (continued)

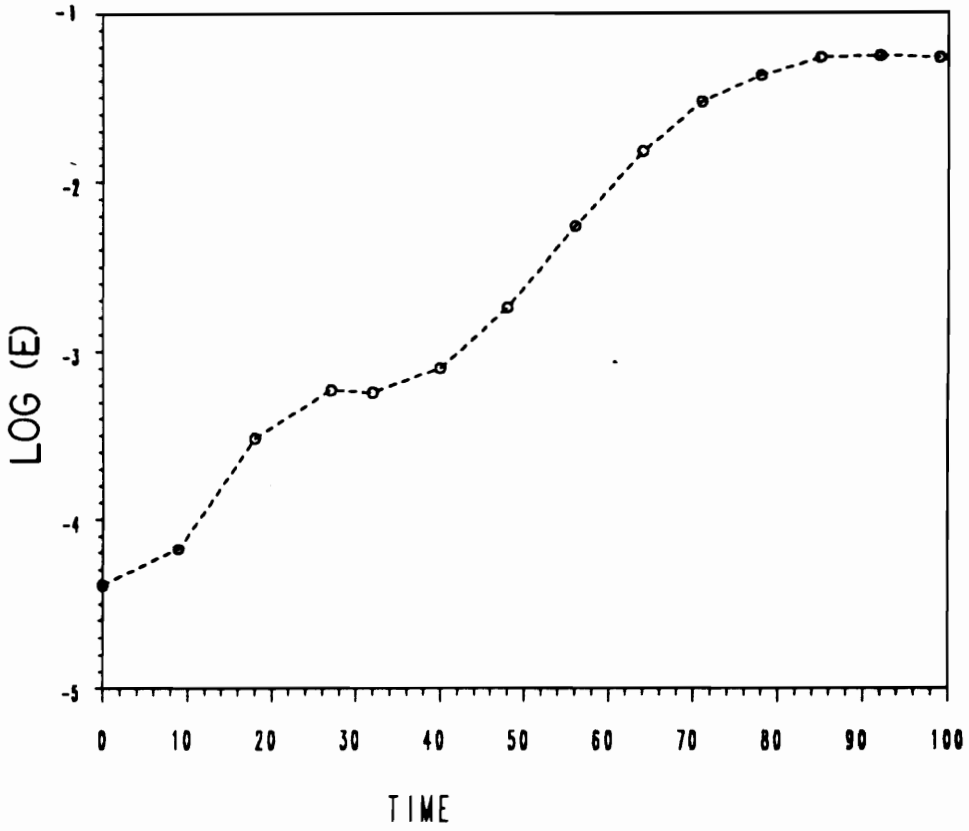

Fig. 6.11 Growth of kinematic energy for small-scale motions with wavenumber higher than 4α (1.6); case A.

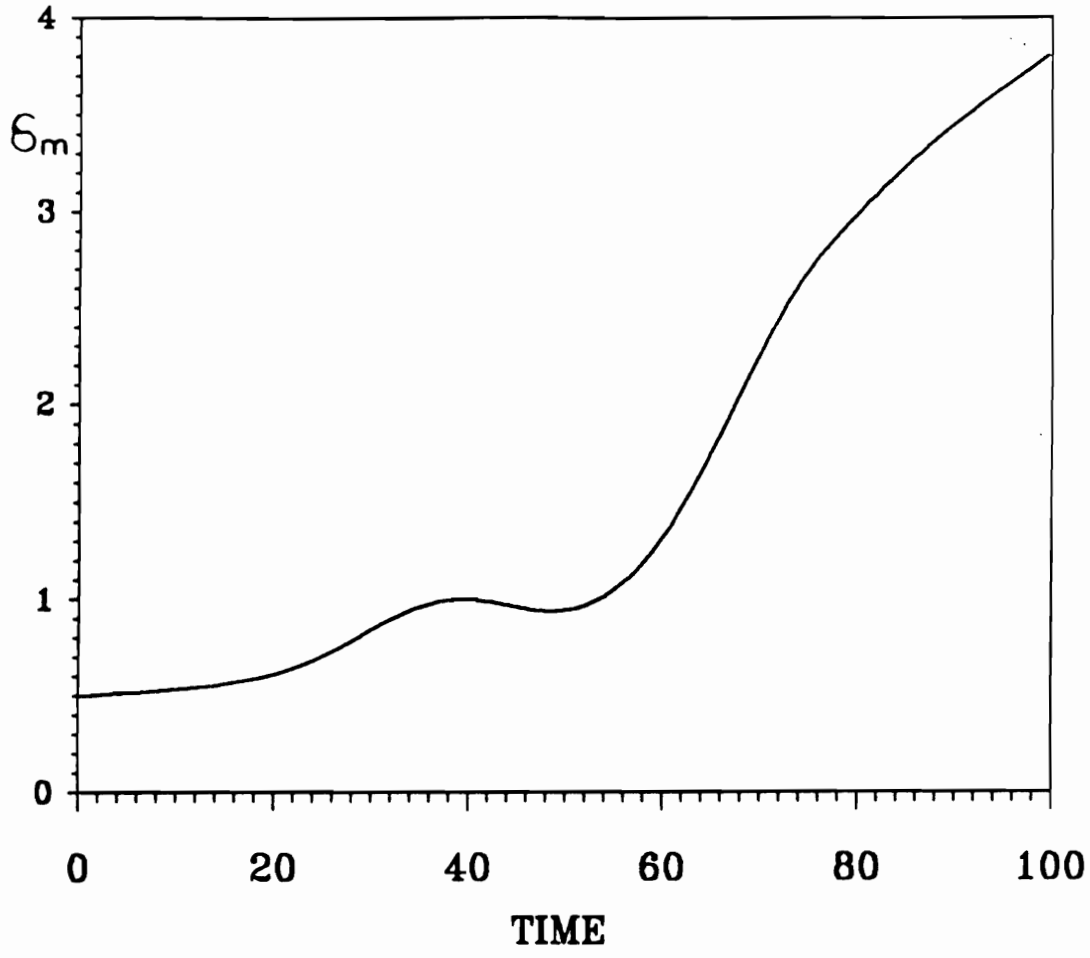

Fig. 6.12 Growth of momentum thickness; case A.

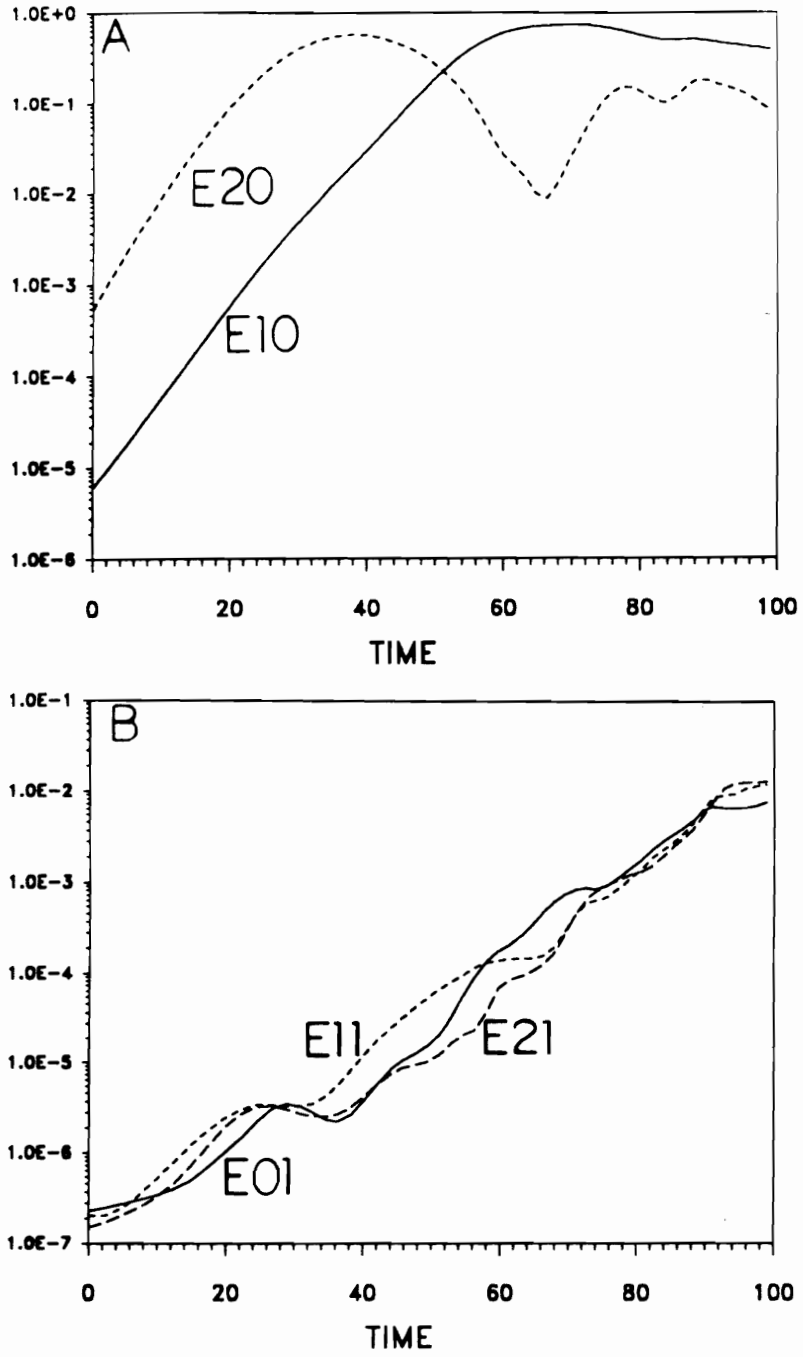

Fig. 6.13 Growth of modal energy; case B.

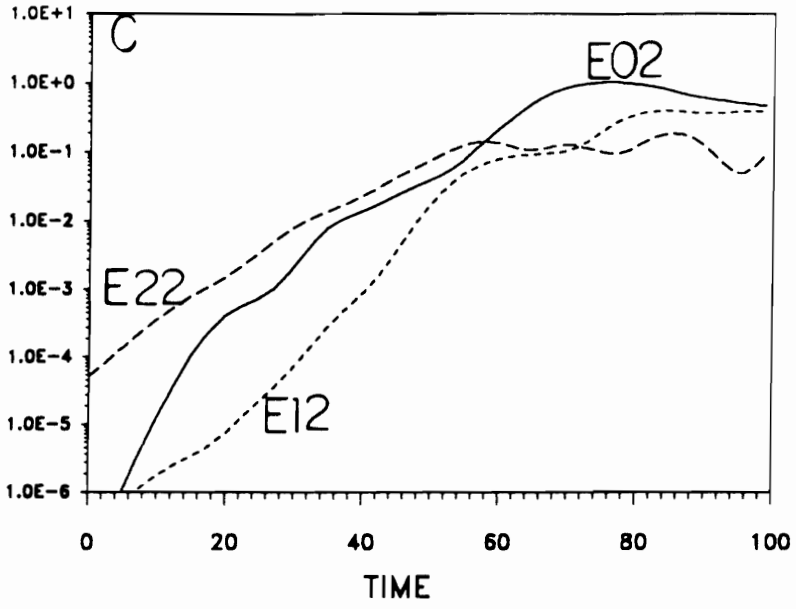

Fig. 6.13 (continued)

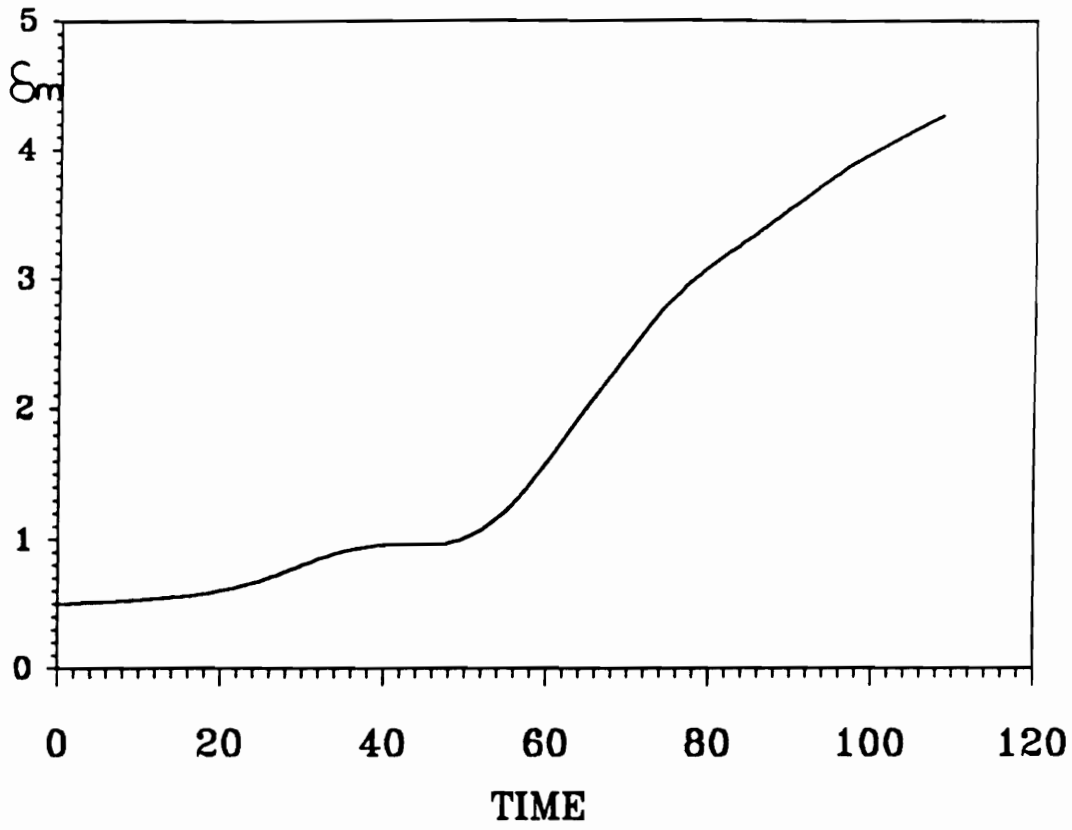

Fig. 6.14 Growth of momentum thickness; case B.

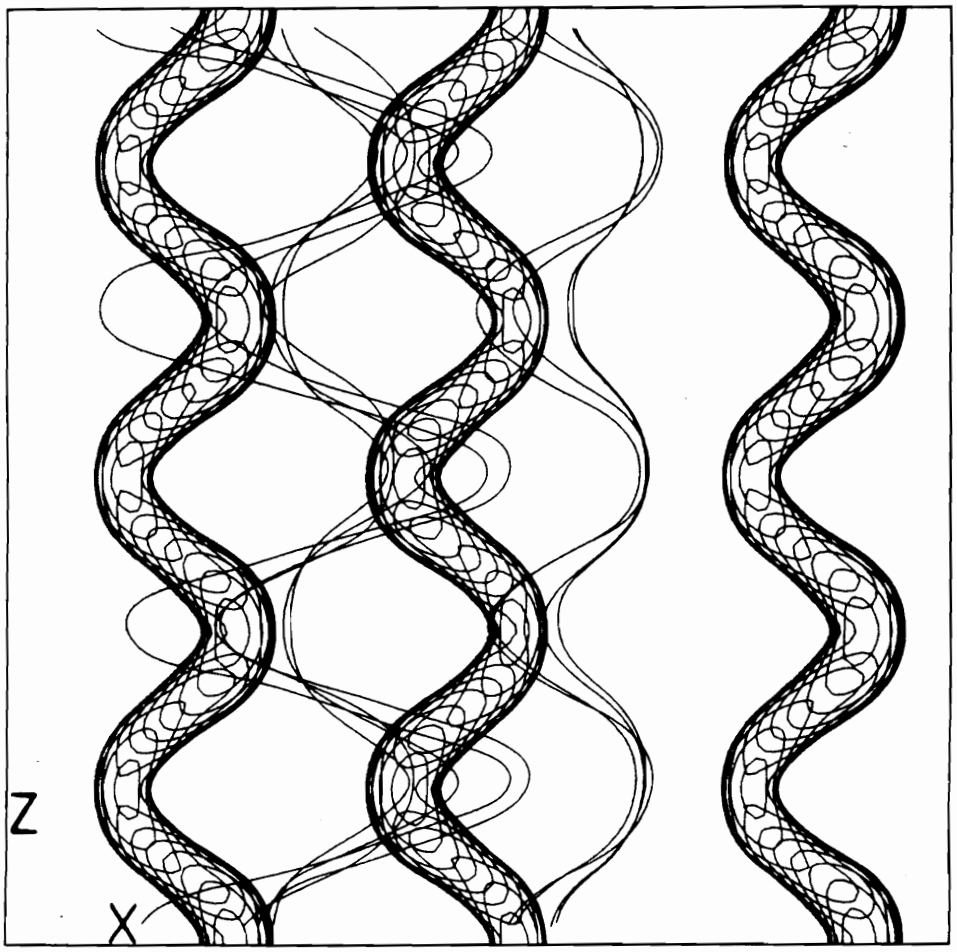

Fig. 6.15 Projection of constant pressure surface and vortex lines on the $x-z$ plane, $P/(\rho_1 RT_1) = 0.89$; $t = 51.2$, case B.

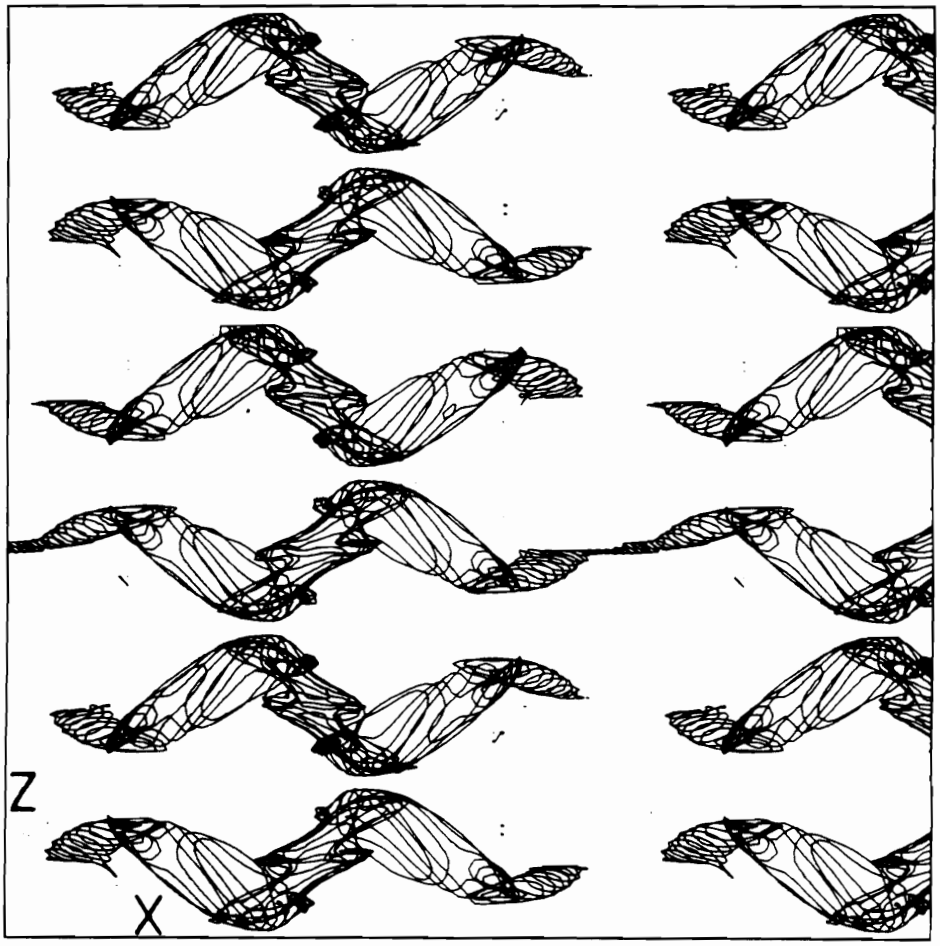

Fig. 6.16 Projection of constant ω_{xy} surface on the $x-z$ plane, $\omega_{xy} = 1.1$; $t = 61.4$, case B.

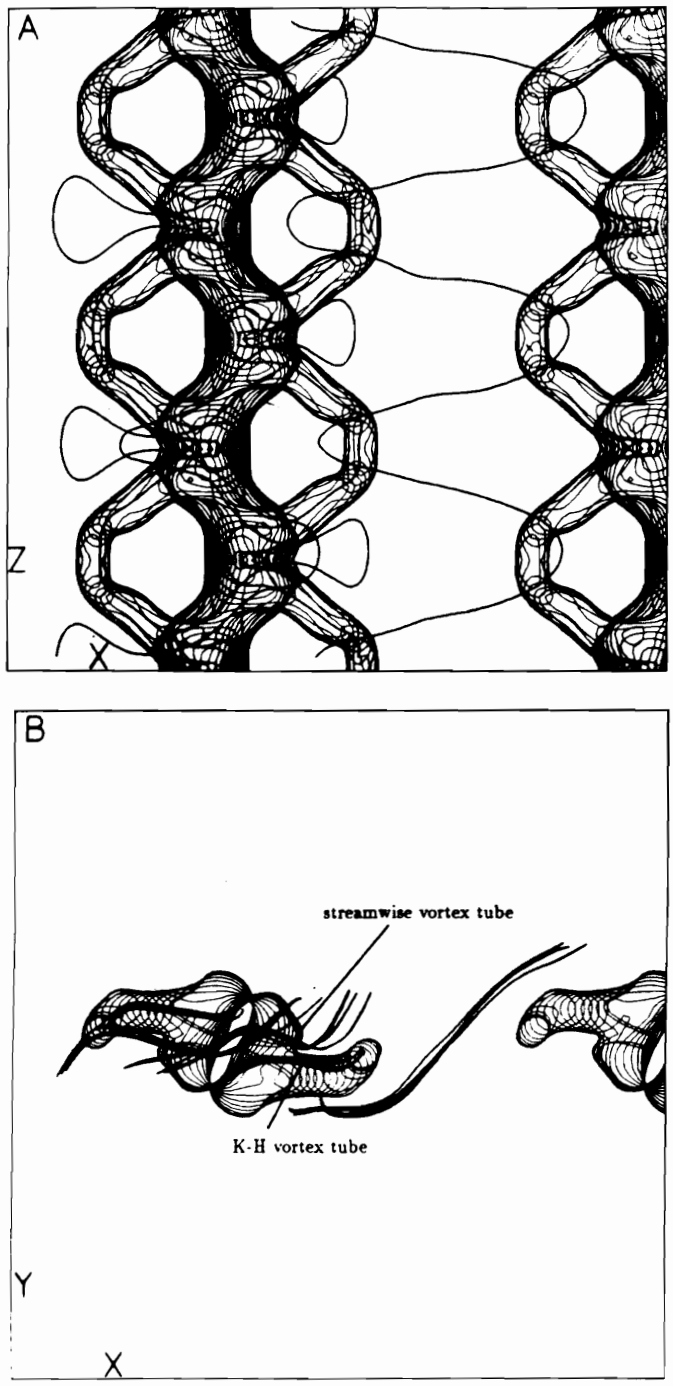

Fig. 6.17 Projections of constant pressure surface and vortex lines; (A) on the $x-z$ plane, (B) on the $x-y$ plane, only structures between $z=0$ and $z=1/4L_z$ are shown; $P/(\rho_1 RT_1)=0.89$; $t=61.4$, case B.

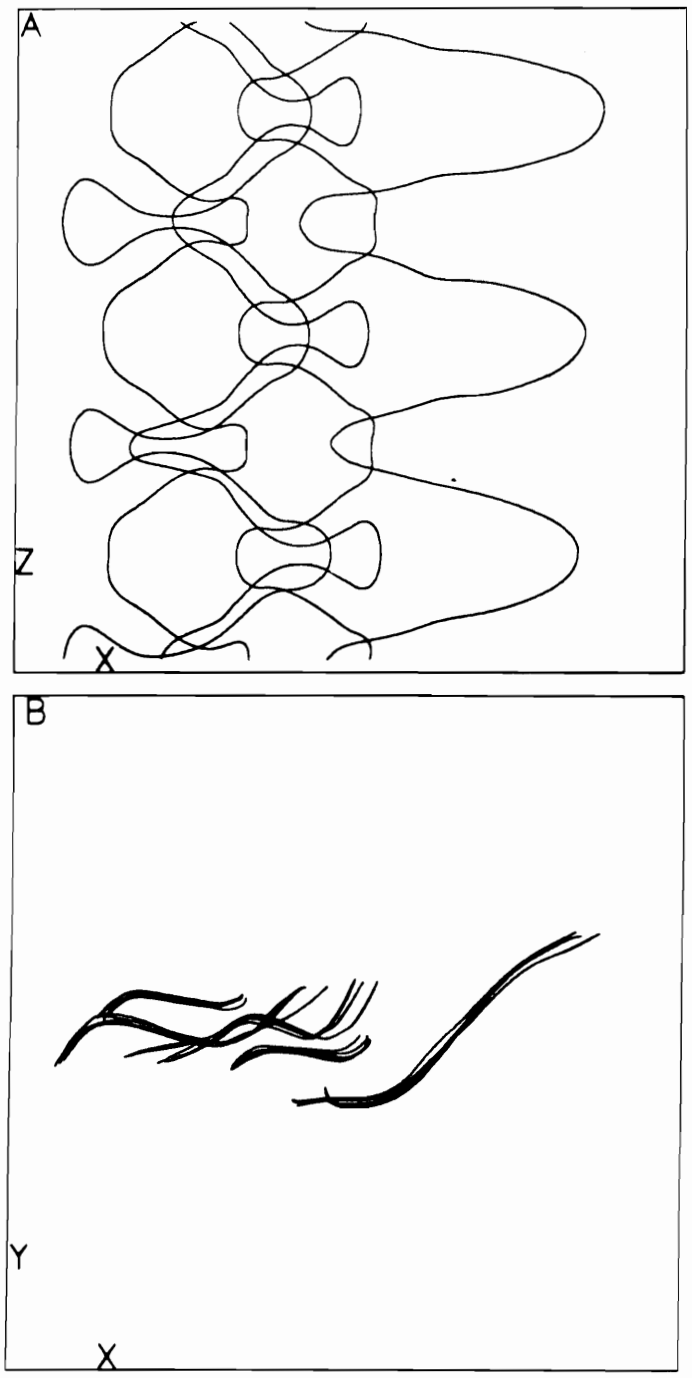

Fig. 6.18 Projections of vortex lines in Fig. 6.17; (A) on $x - z$ plane, (B) on $x - y$ plane; $t = 61.4$; case B.

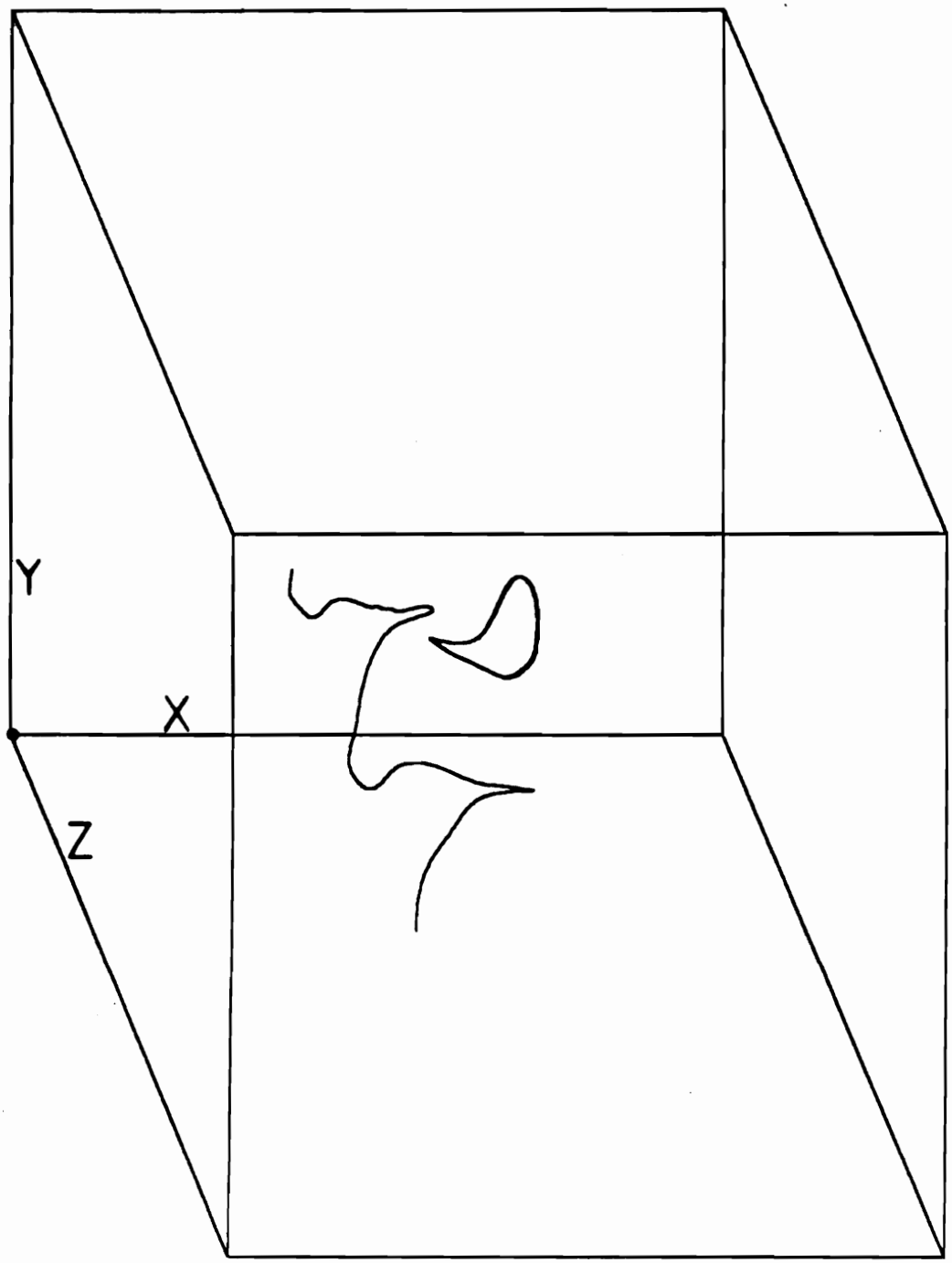

Fig. 6.19 Perspective view of vortex lines resulting from the reconnection mechanism; $t = 61.4$; case B.

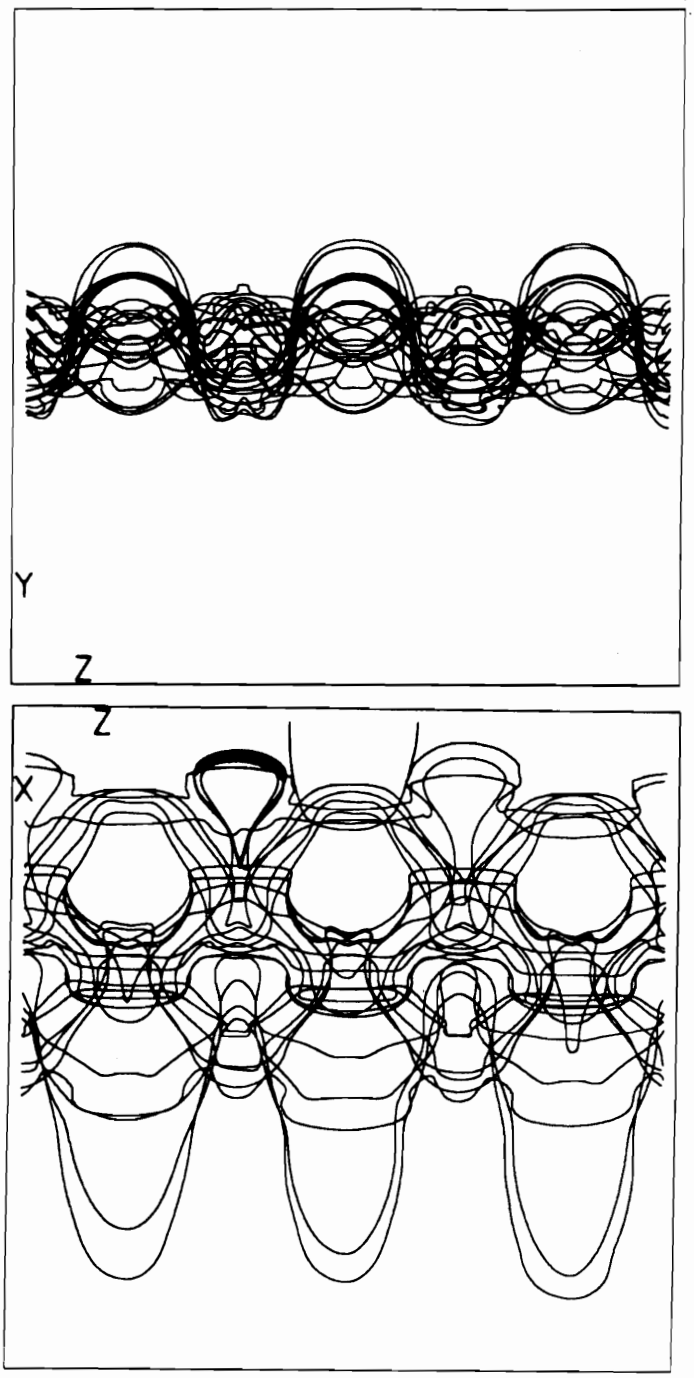

Fig. 6.20 Projections of vortex lines on the $x - z$ and $z - y$ planes; $t = 61.4$; case B.

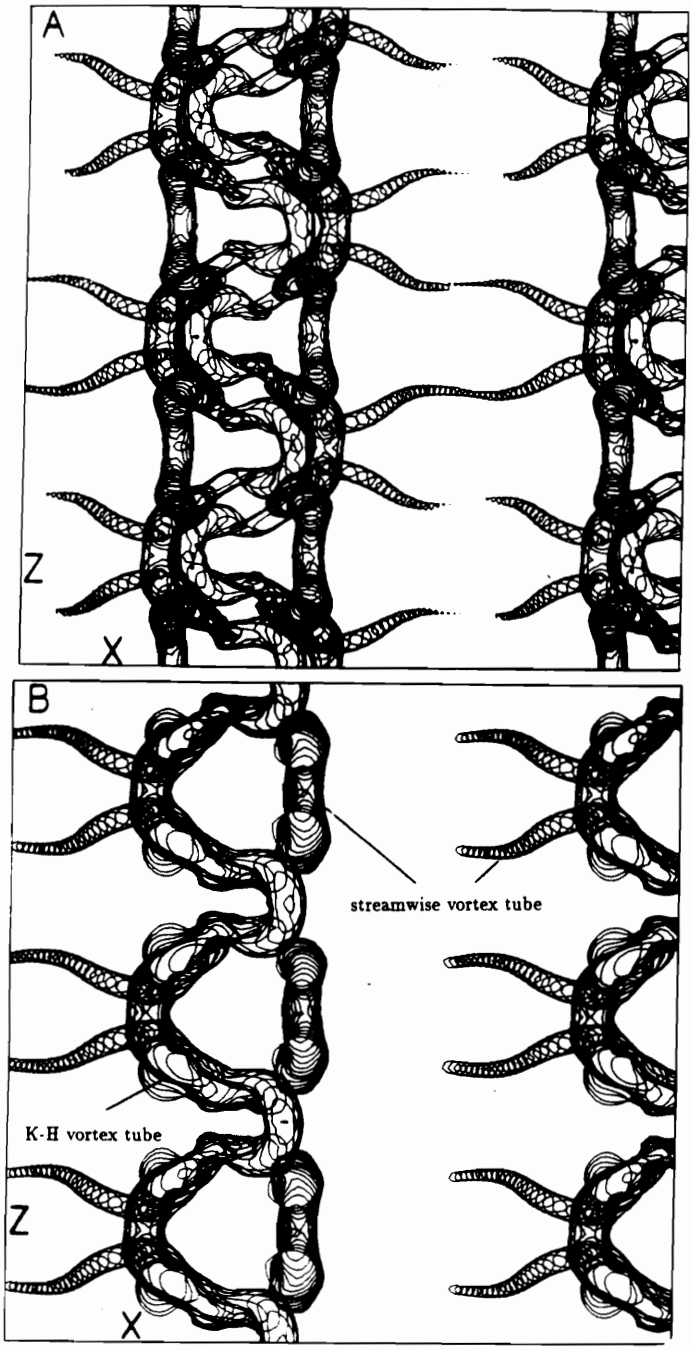

Fig. 6.21 Projections of constant pressure surface; $t = 71.1$, case B; (A) $x-z$ plane, $P/(\rho_1 RT_1) = 0.86$, complete structures, (B) $x - z$ plane, $P/(\rho_1 RT_1) = 0.88$, upper-stream structures, (C) $x - z$ plane, $P/(\rho_1 RT_1) = 0.88$, lower-stream structures, (D) $z - y$ plane, $P/(\rho_1 RT_1) = 0.88$, structures between $x = 1/4L_x$ and $x = 1/2L_x$.

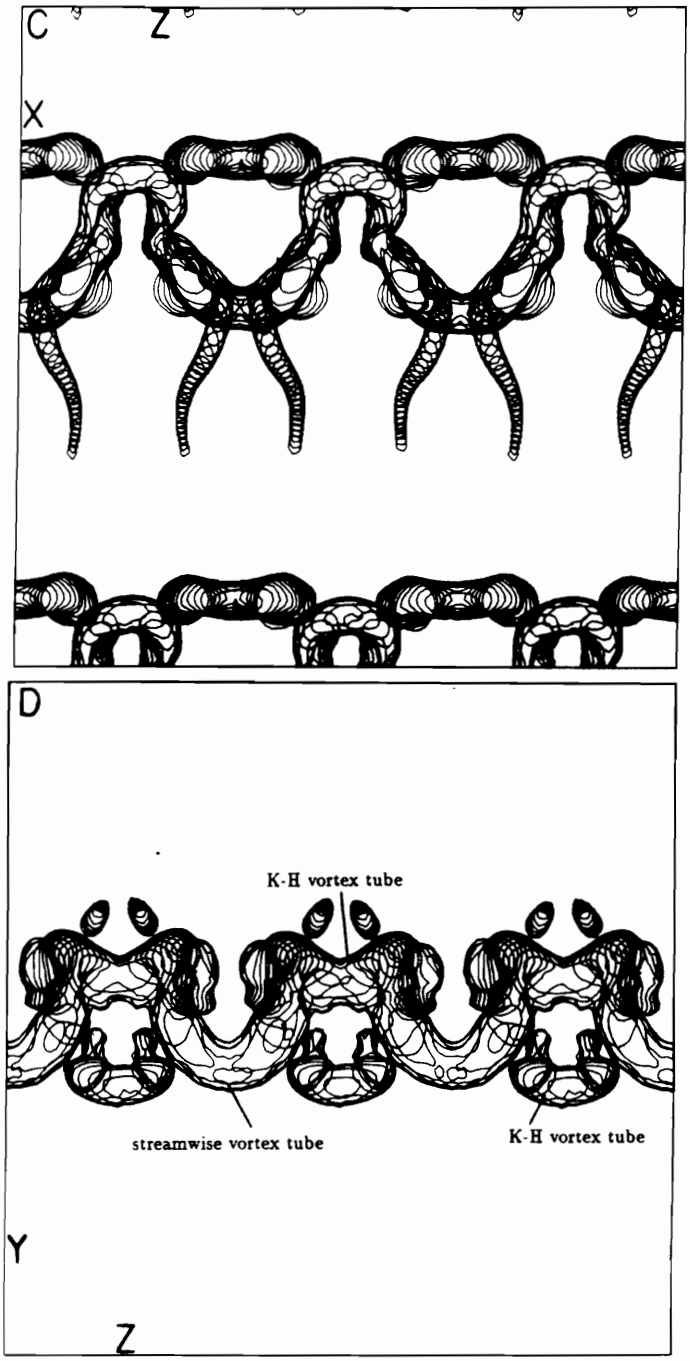

Fig. 6.21 (continued)

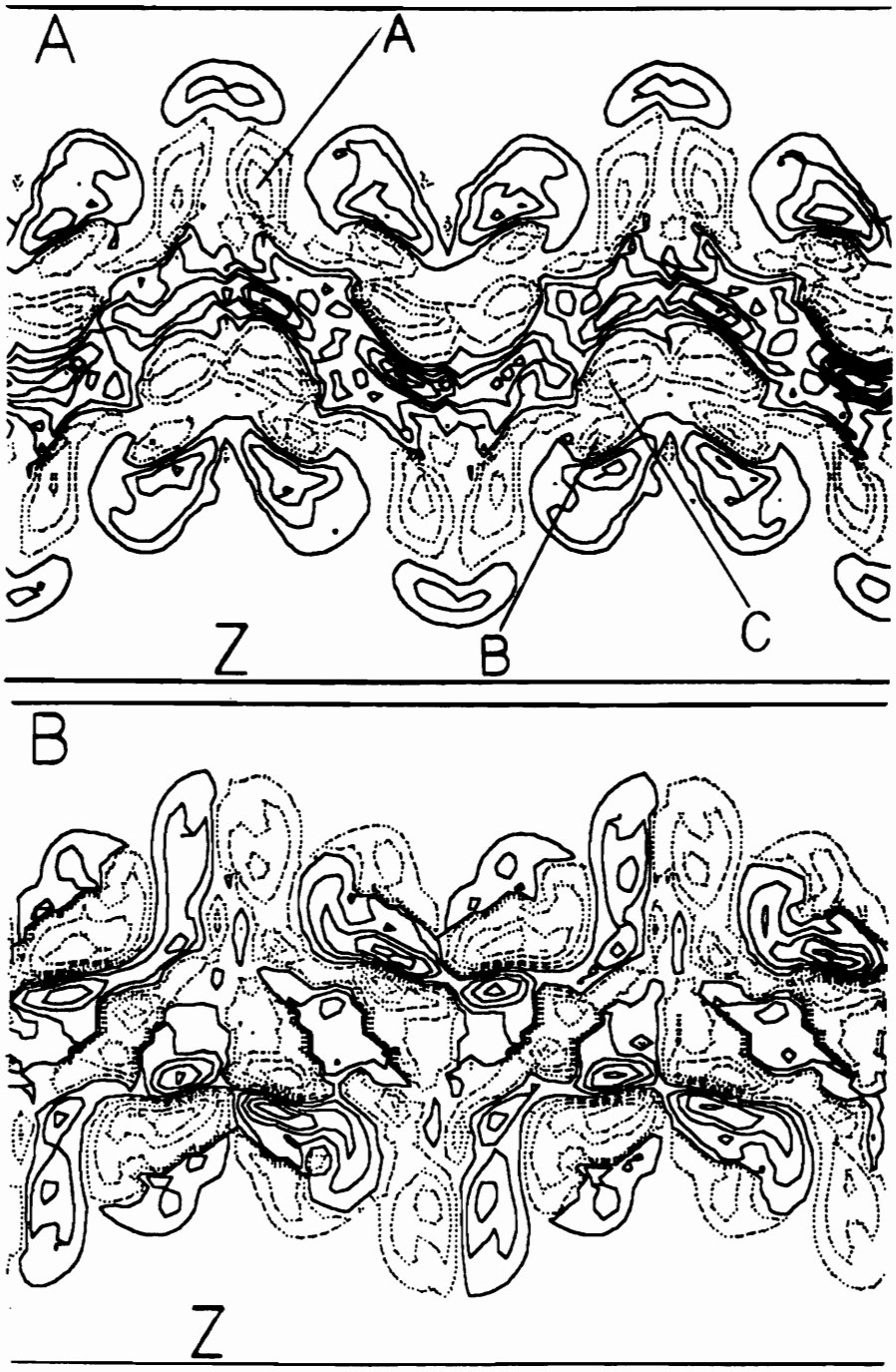

Fig. 6.22 Contours in the $z - y$ plane at $x = 1/2L_x$; $t = 71.1$; case B; (A) ω_x; $\omega_{max} = 0.673$, $\omega_{min} = -1.749$, (B) ω_{xy} with the sign of ω_x; $\omega_{max} = 1.755$, $\omega_{min} = -1.755$; negative values are shown by solid lines, plots are truncated at $y = \pm 12$.

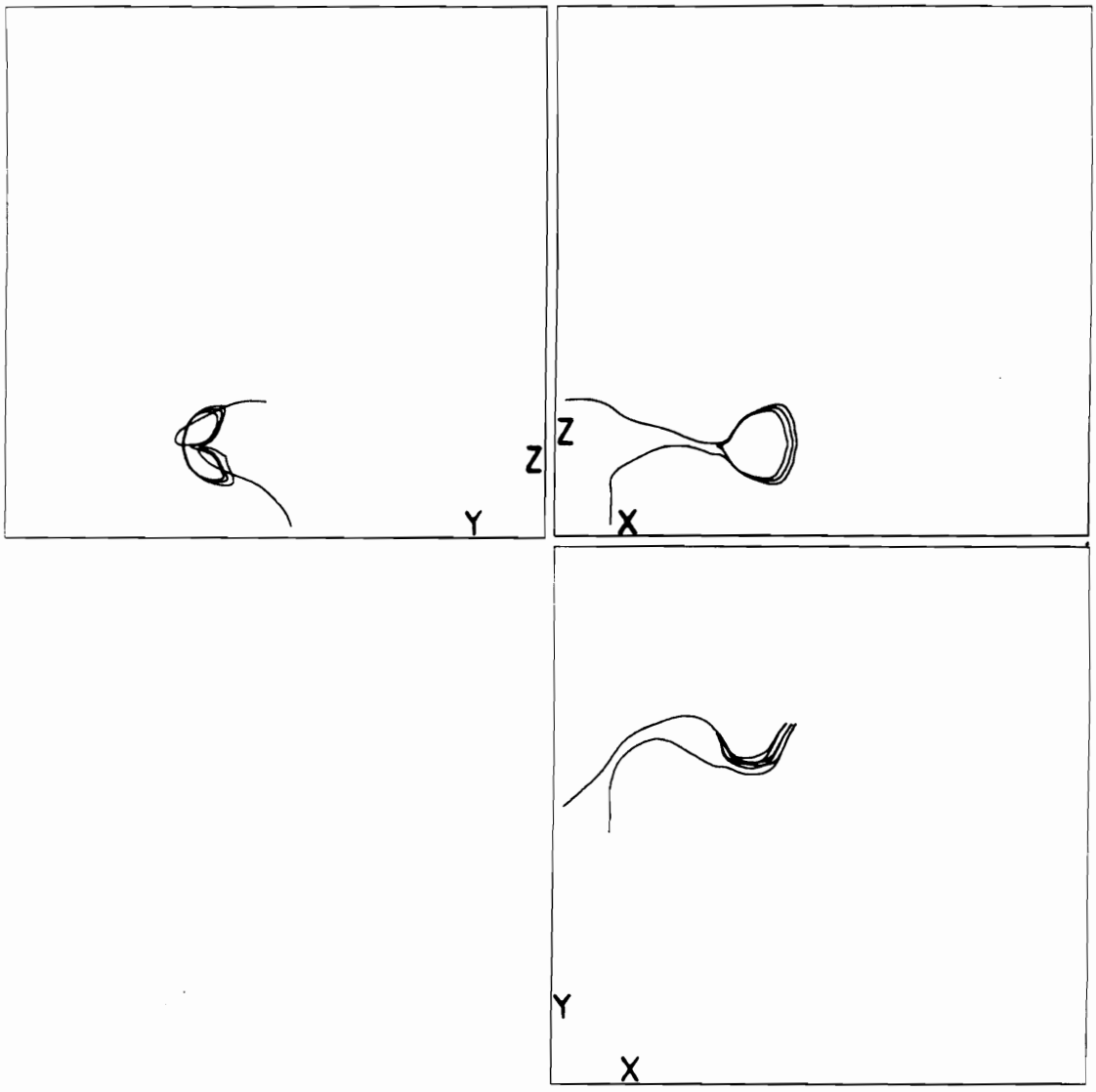

Fig. 6.23 Projections of the vortex line through point A in Fig. 6.22; $t = 71.1$, case B.

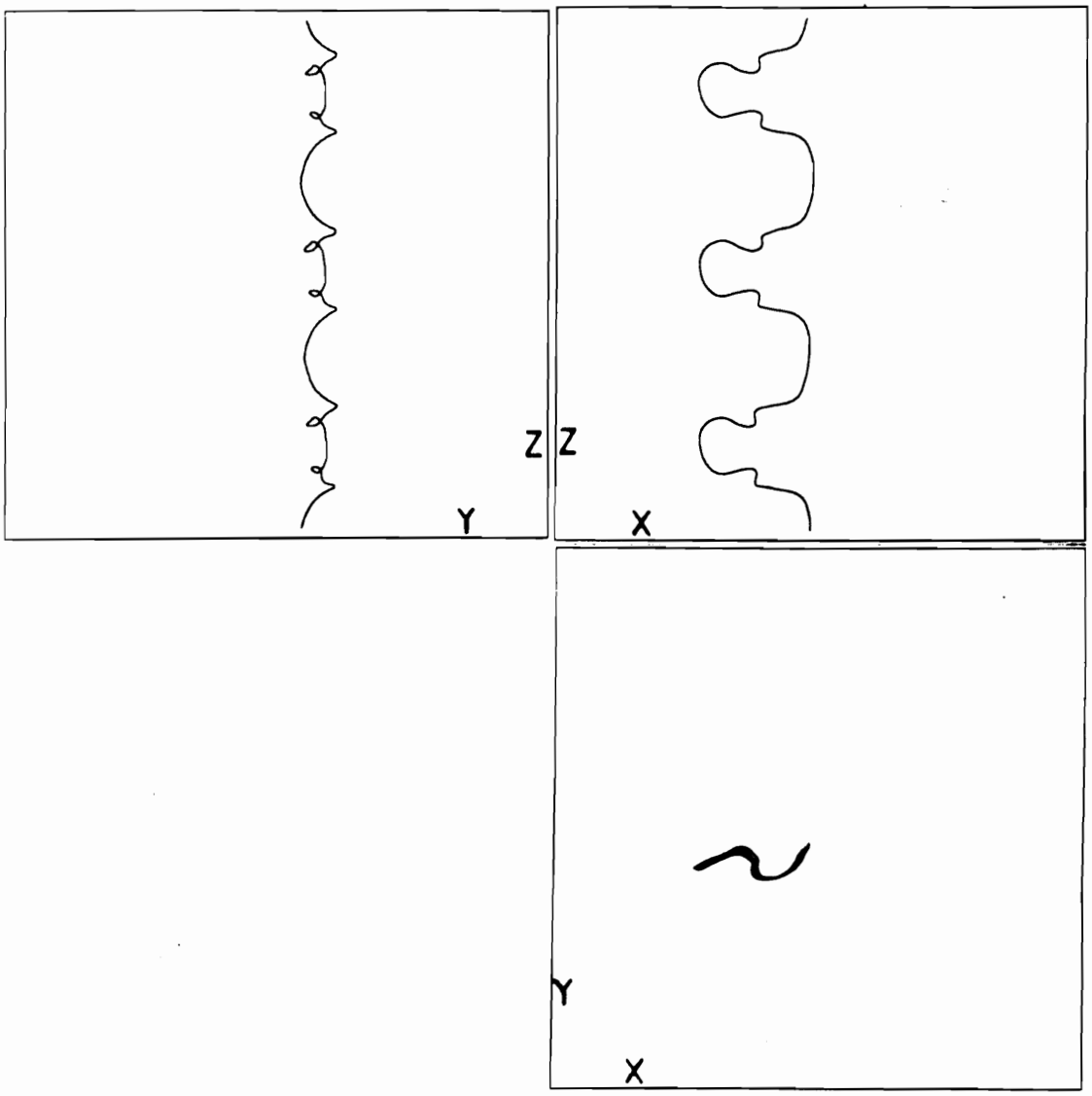

Fig. 6.24 Projections of the vortex line through point B in Fig. 6.22; $t = 71.1$, case B.

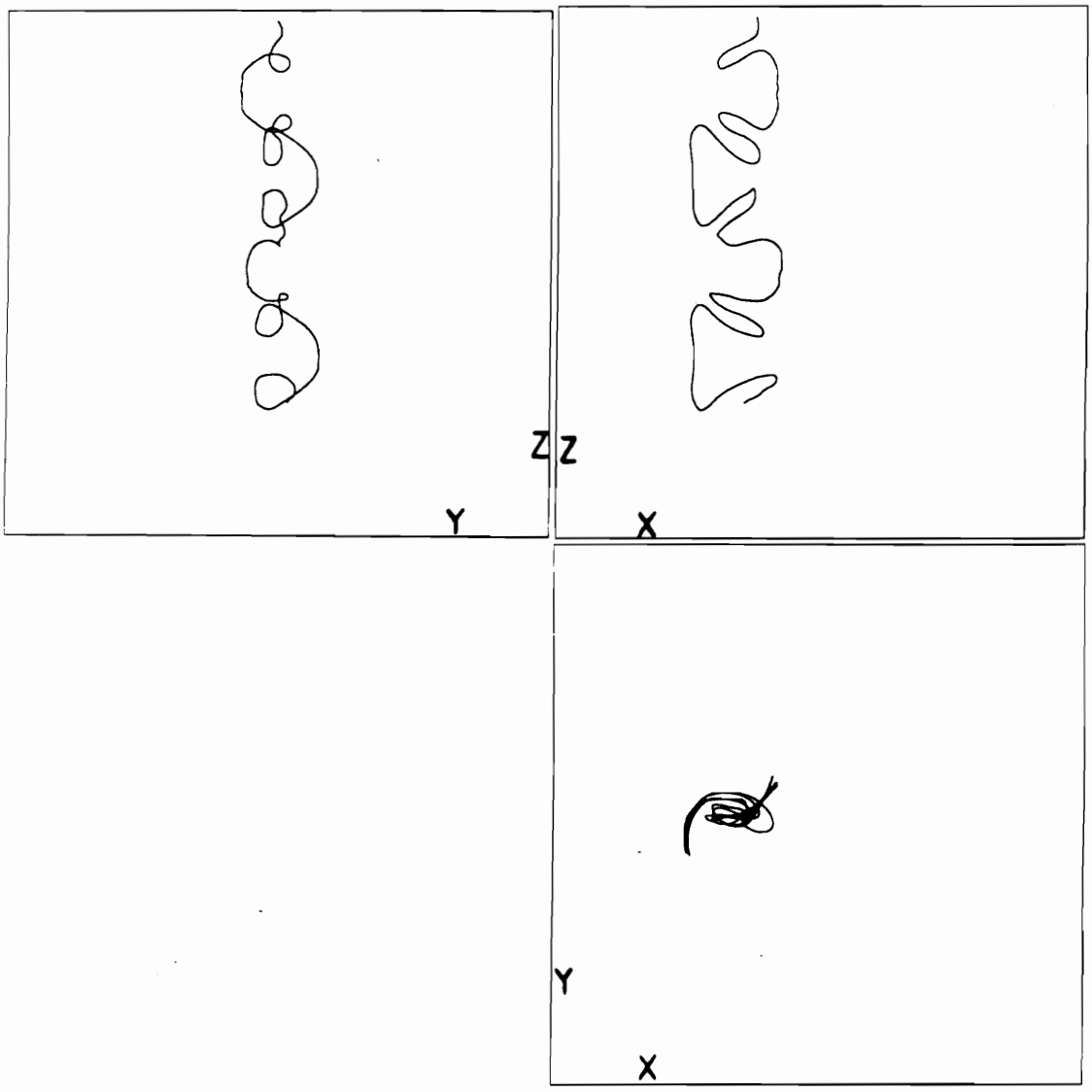

Fig. 6.25 Projections of the vortex line through point C in Fig. 6.22; $t = 71.1$, case B.

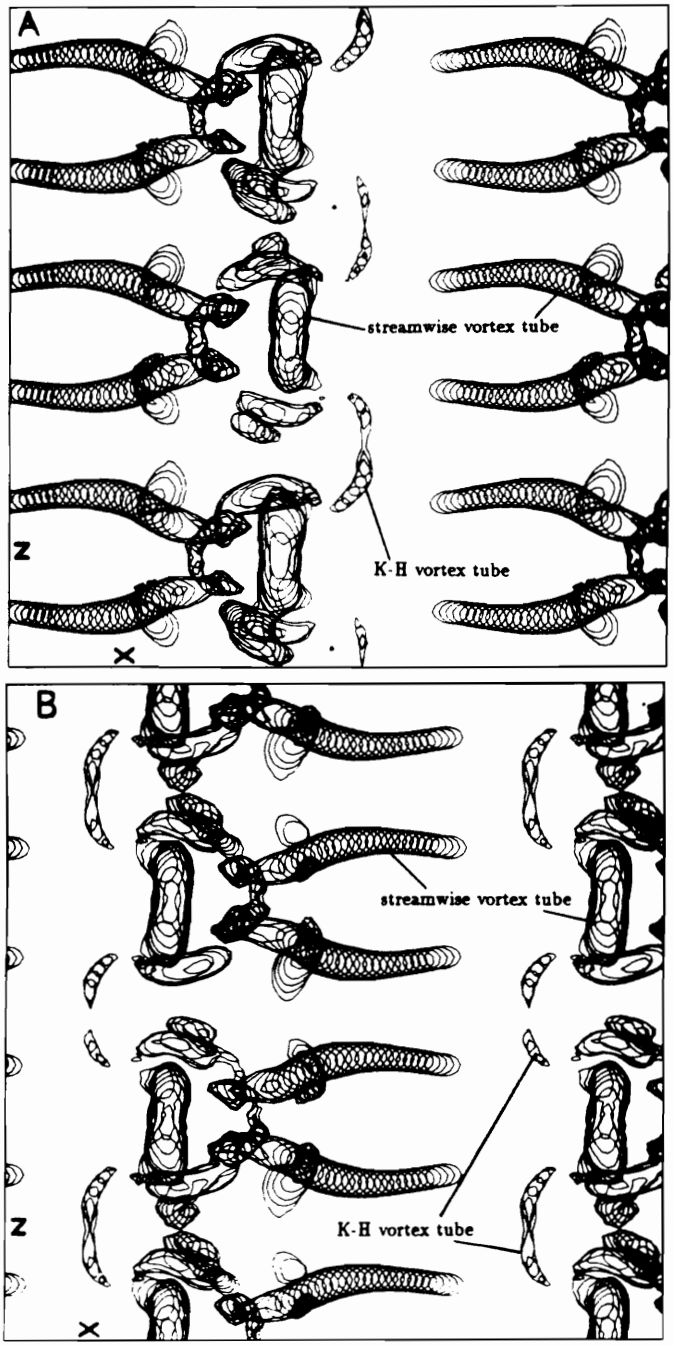

Fig. 6.26 Projections of constant pressure surface on the $x - z$ plane; $t = 80.6$, case B, $P/(\rho_1 RT_1) = 0.87$; (A) upper-stream structures, (B) lower-stream structures.

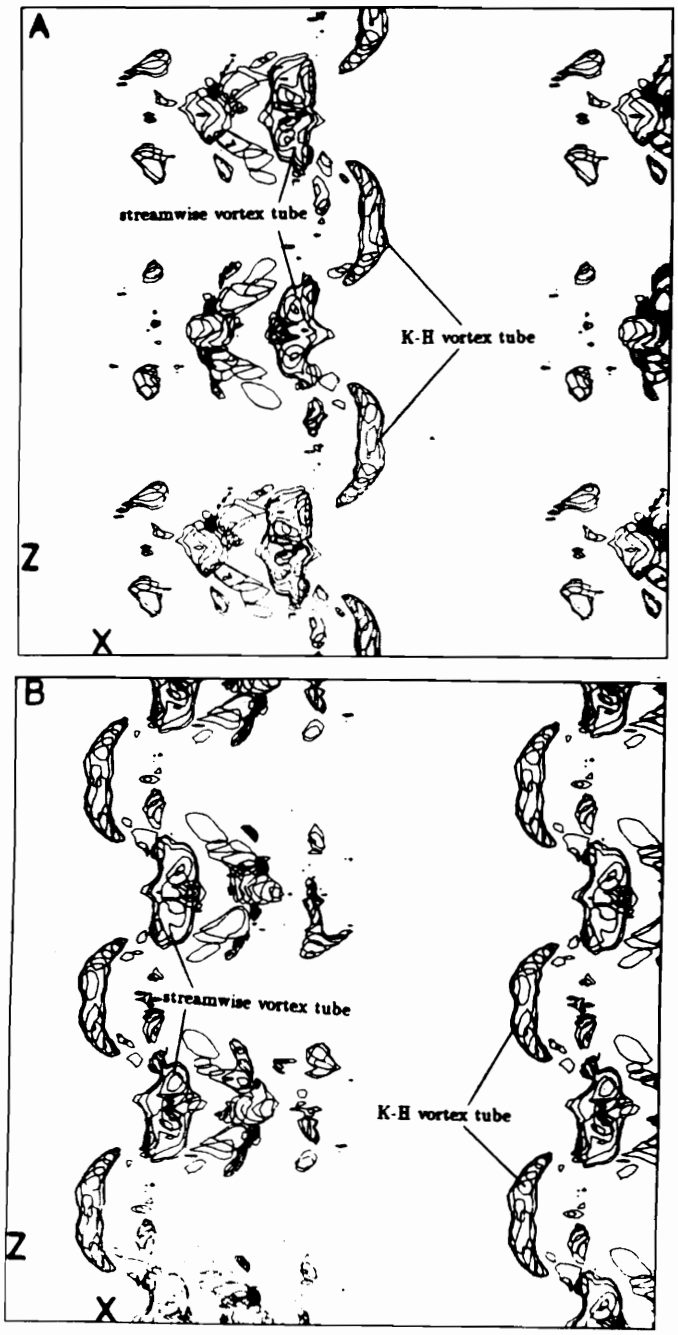

Fig. 6.27 Projections of constant ω_z surface on the $x - z$ plane; $t = 80.6$; case B, $\omega_z = -1.1$; (A) upper-stream structures, (B) lower-stream structures.

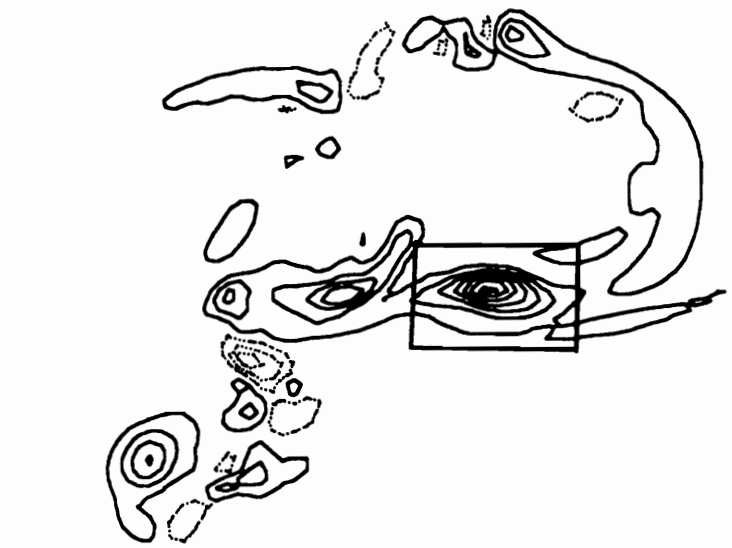

Fig. 6.28 Contours of ω_z at $z = 1/4L_z$; $t = 80.6$; case B; $\omega_{max} = 1.243$, $\omega_{min} = -3.231$; negative values are shown by solid lines.

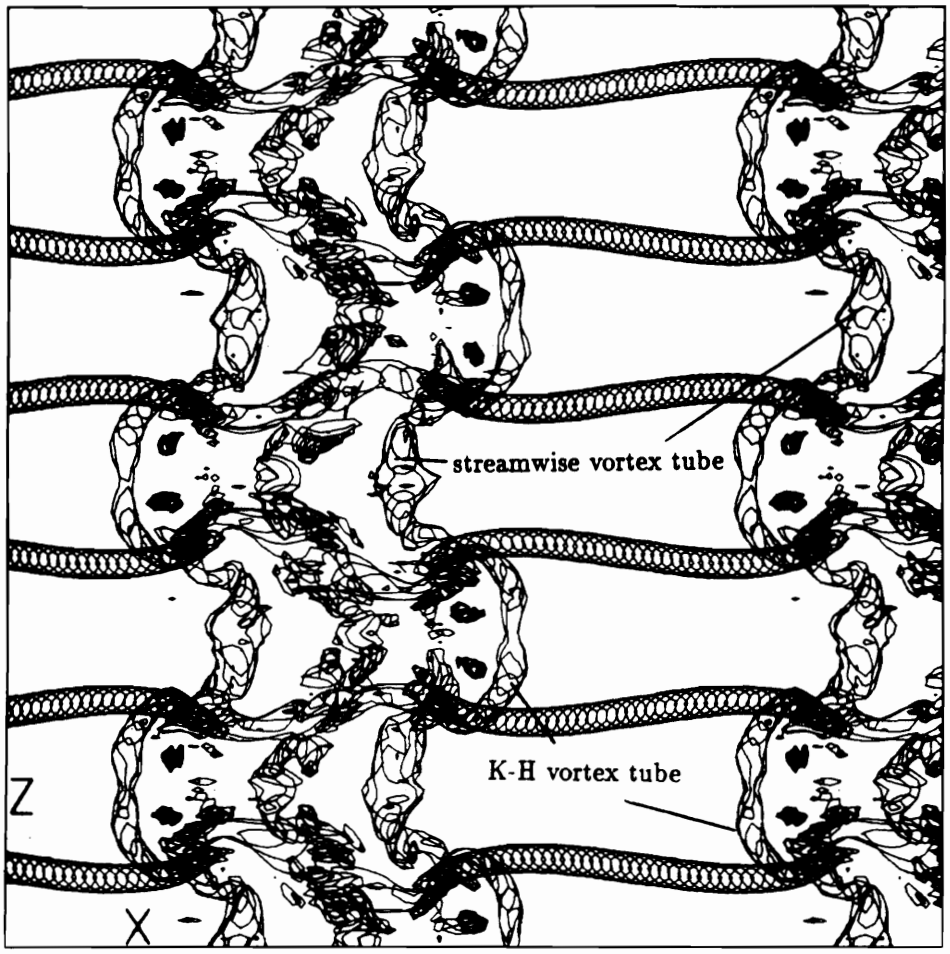

Fig. 6.29 Projection of surface with constant vorticity magnitude, $\omega = 1.6$; $t = 80.6$, case B.

Fig. 6.30 Contours of ω_z at $z = 1/8L_z$; $t = 80.6$, case B; $\omega_{max} = 1.688$, $\omega_{min} = -1.688$.

Fig. 6.31 Contours of ω_z at $z = 1/4L_z$; $\omega_{max} = 1.188$, $\omega_{min} = -3.088$; $t = 80.8$, case B without random disturbance.

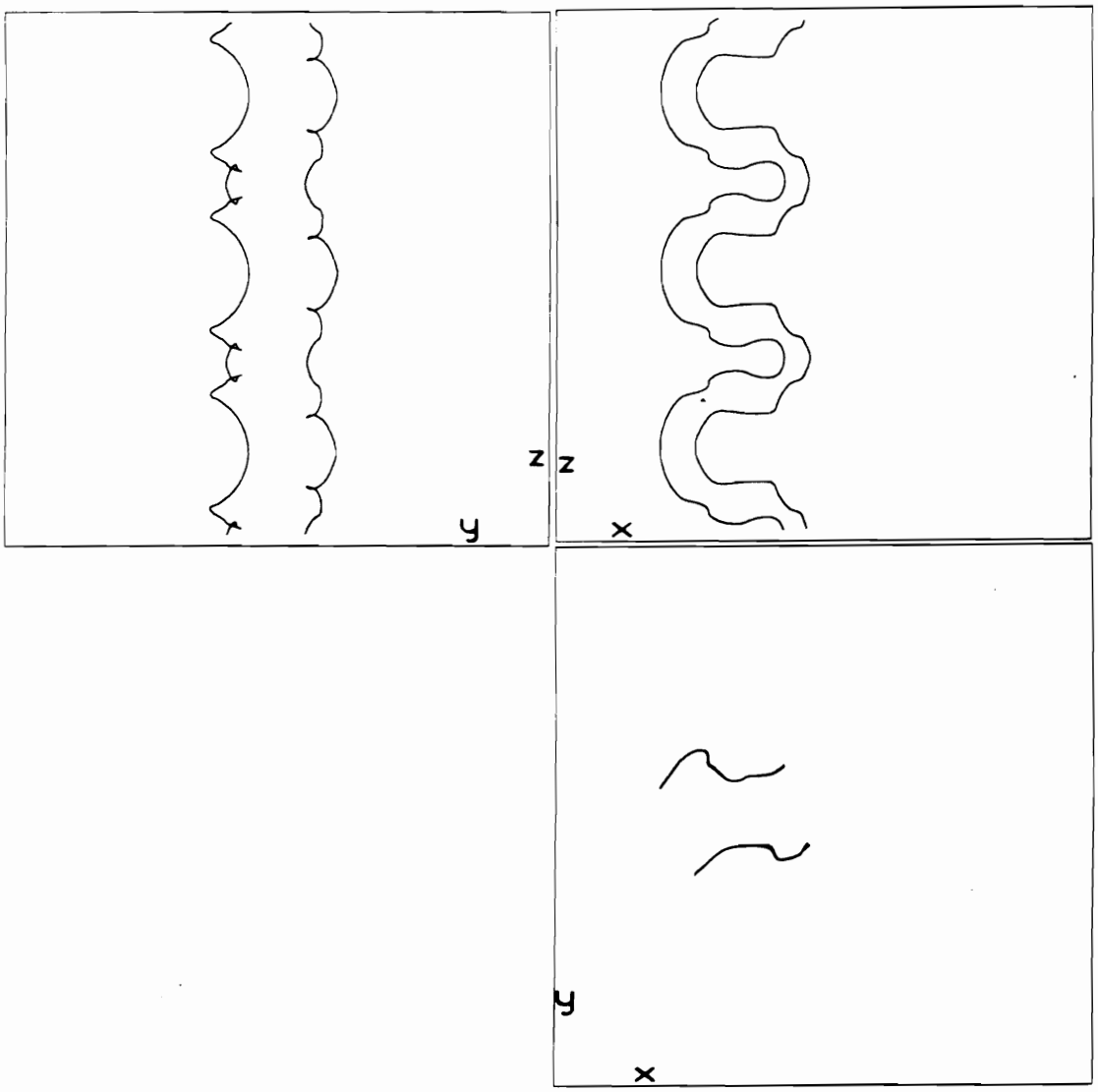

Fig. 6.32 Projections of vortex lines through the K-H vortex tubes; $t = 71.2$; case B without random disturbance.

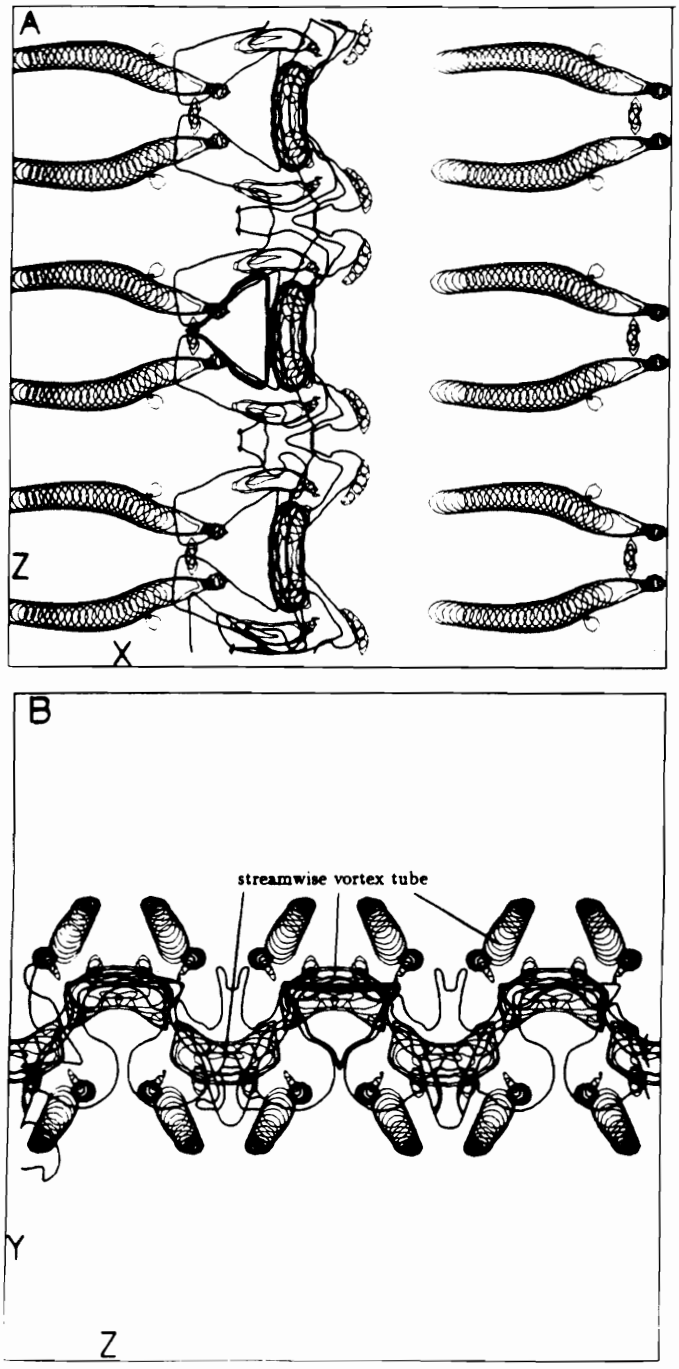

Fig. 6.33 Projections of constant pressure surface and vortex lines; $t = 80.8$, case B, without random disturbance; $P/(\rho_1 RT_1) = 0.855$; (A) upper-stream structures, on $x - z$ plane, (B) structures between $x = 1/4L_x$ and $x = 1/2L_x$, on $z - y$ plane.

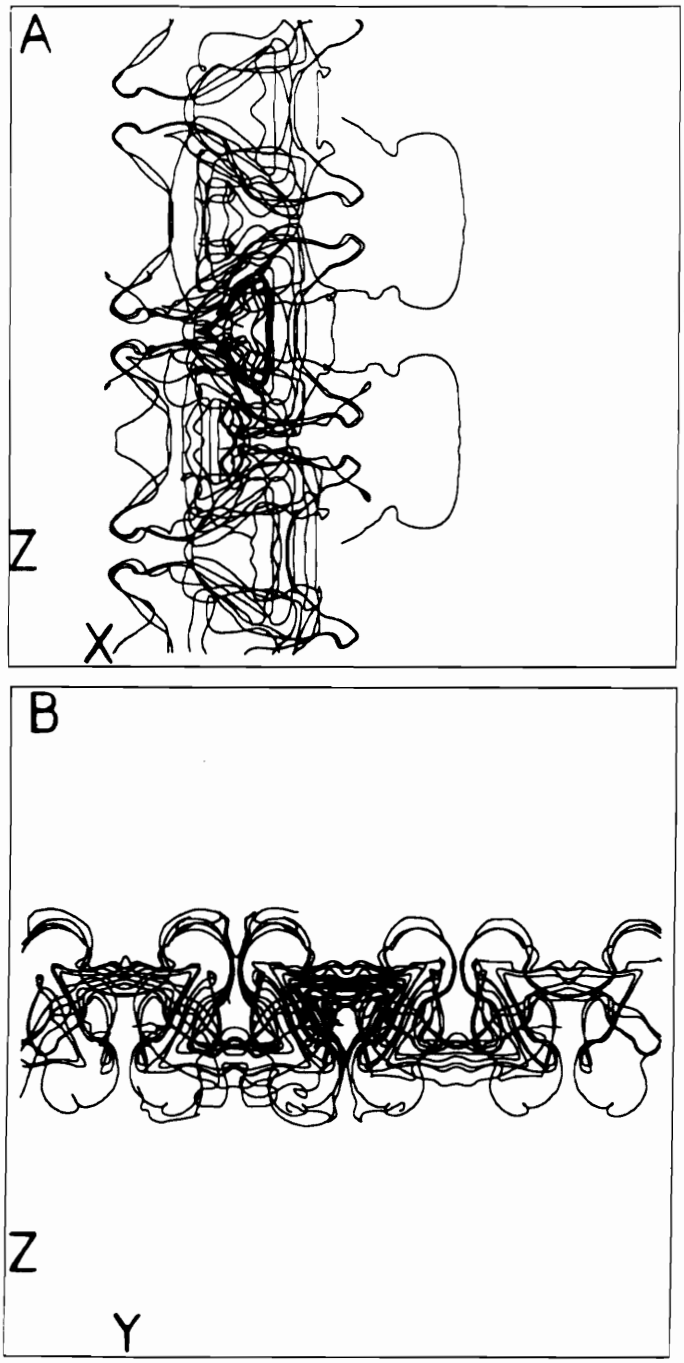

Fig. 6.34 Projections of vortex lines; $t = 80.8$; case B, without random disturbance; vortex lines start at $x = 1/2L_x$, along and near the interface ($y = 0$).

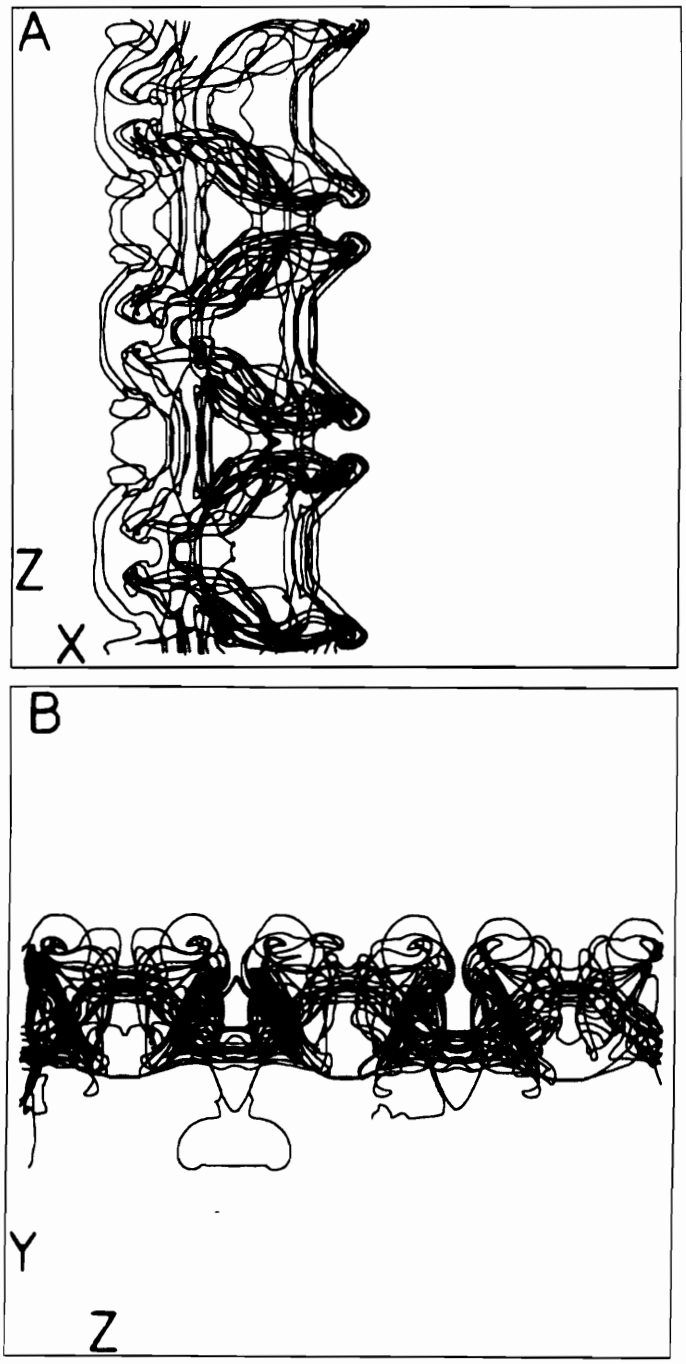

Fig. 6.35 Projections of vortex lines; $t = 80.8$; case B, without random disturbance; vortex lines start at $z = 5/8L_z$, along and near the interface ($y = 0$).

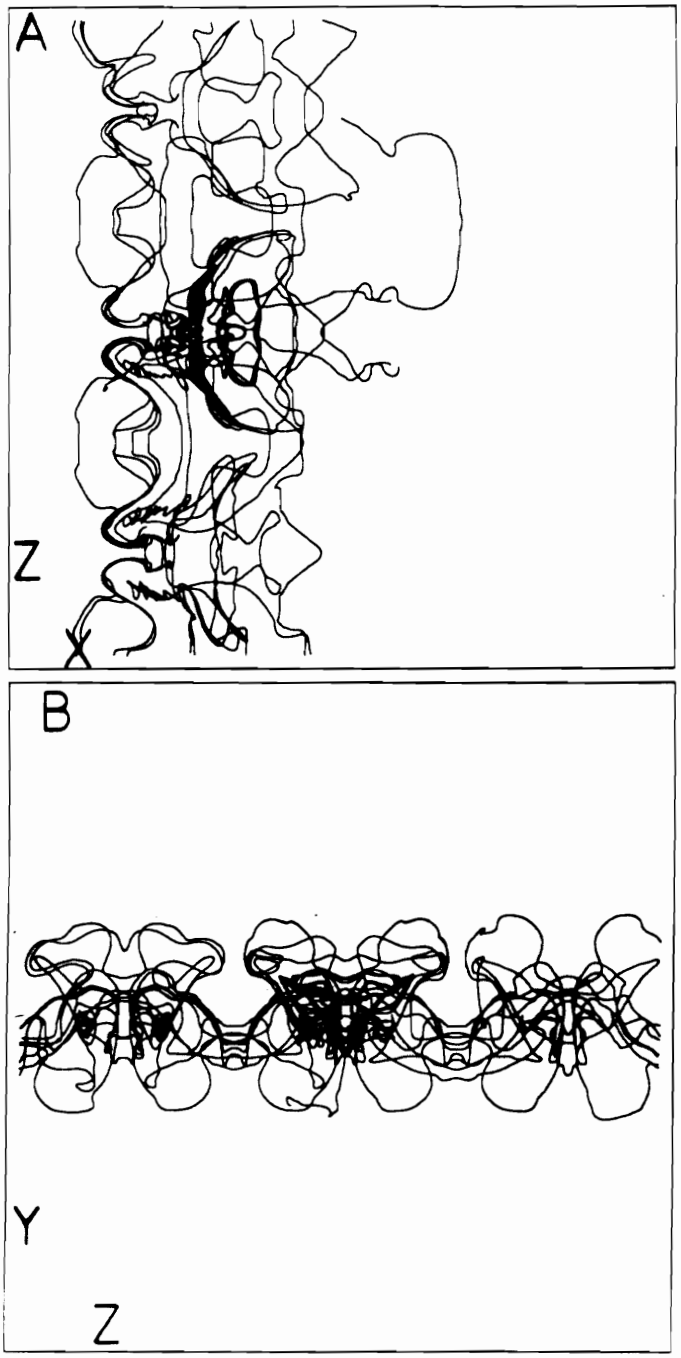

Fig. 6.36 Projections of vortex lines; $t = 80.8$; case B, without random disturbance; vortex lines start at $z = 3/4L_z$, along and near the interface ($y = 0$).

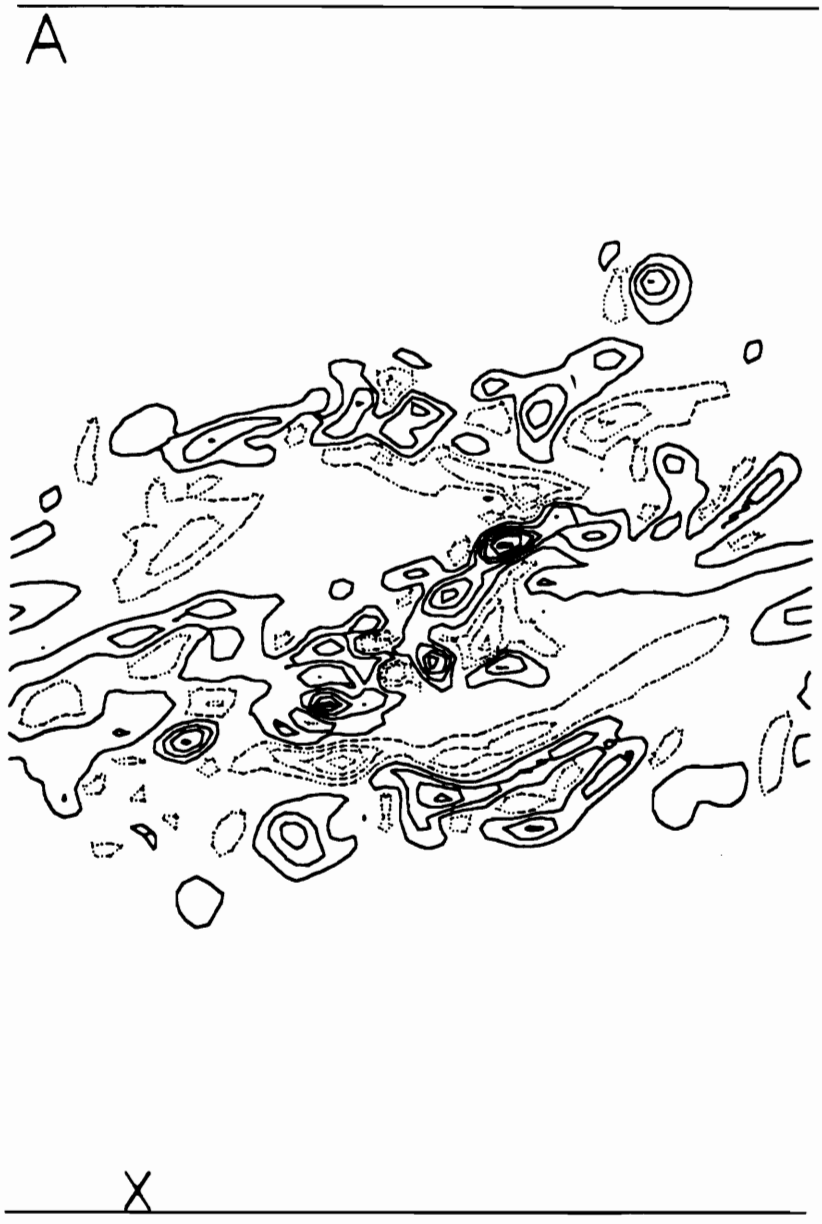

Fig. 6.37 Contours of ω_z, $t = 98.9$; case B; (A) at $z = 1/8L_z$, $\omega_{max} = 1.544$, $\omega_{min} = -2.426$, (B) at $z = 1/4L_z$, $\omega_{max} = 1.800$, $\omega_{min} = -1.800$; negative values are shown by solid lines.

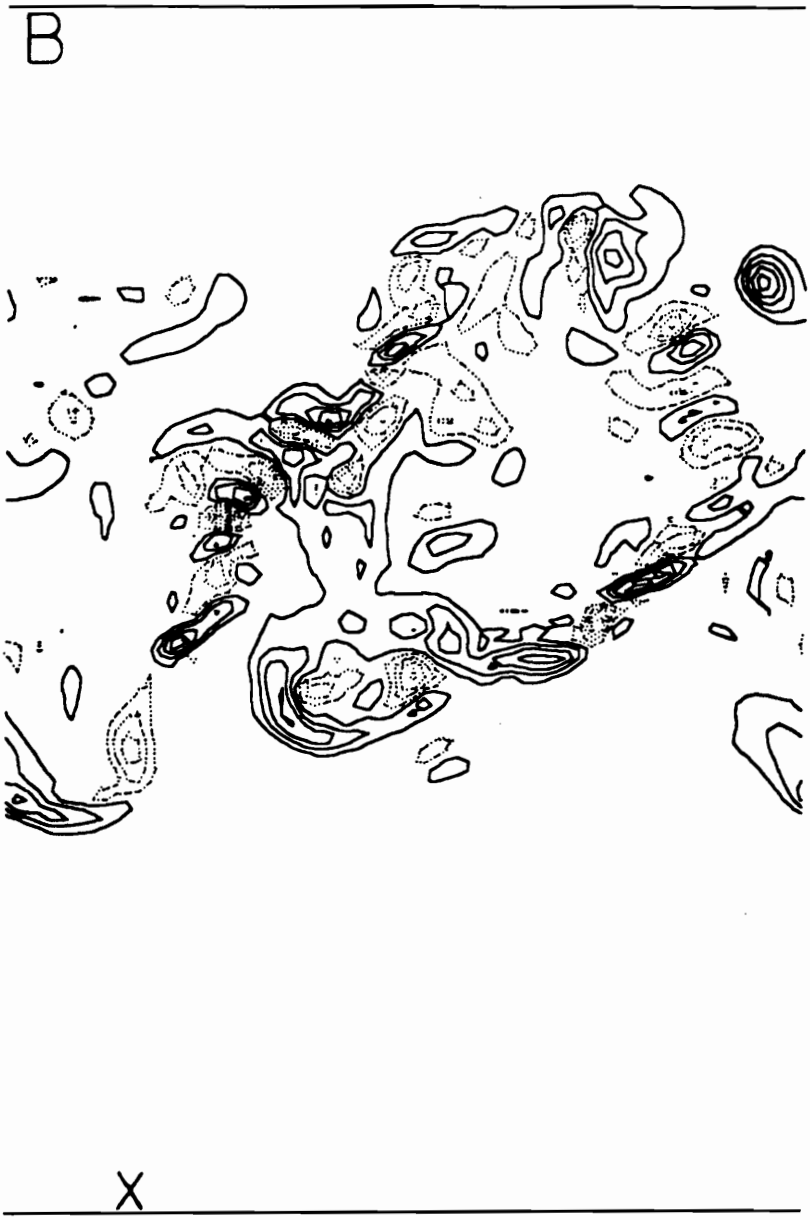

Fig. 6.37 (continued)

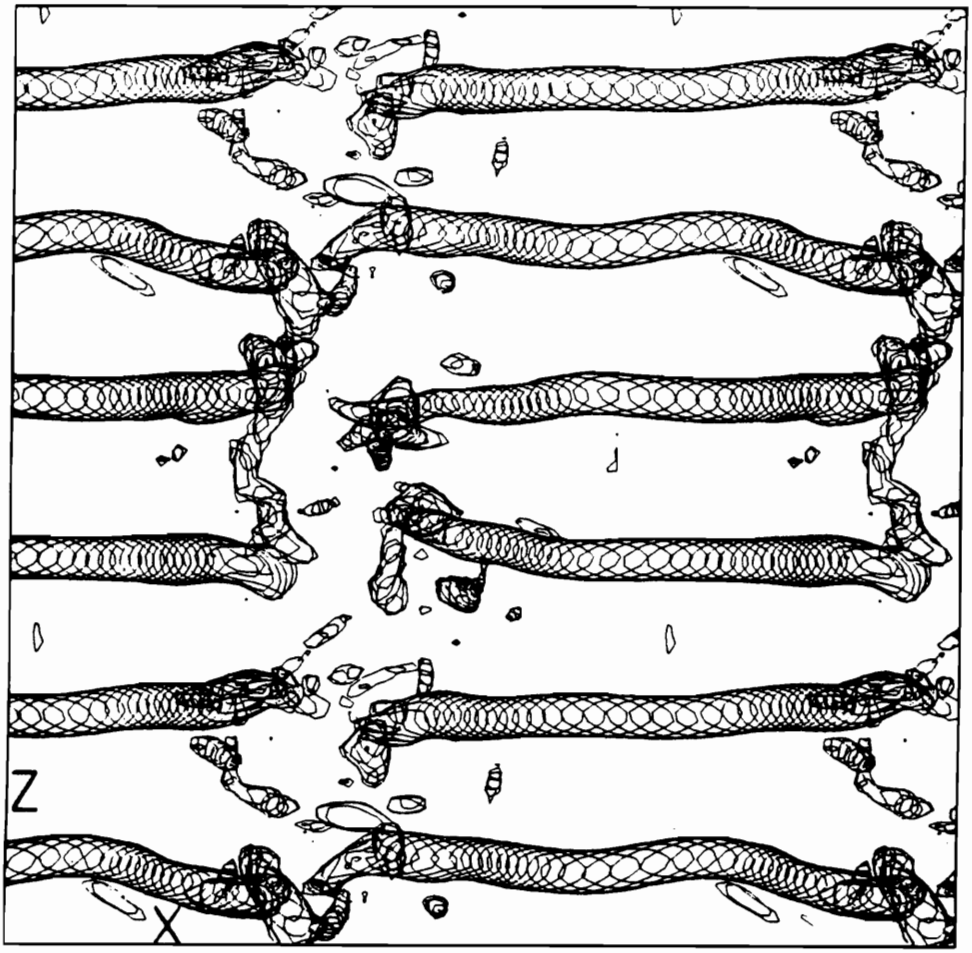

Fig. 6.38 Projection of constant pressure surface on the $x - z$ plane, $t = 98.9$, $P/(\rho_1 RT_1) = 0.885$, case B

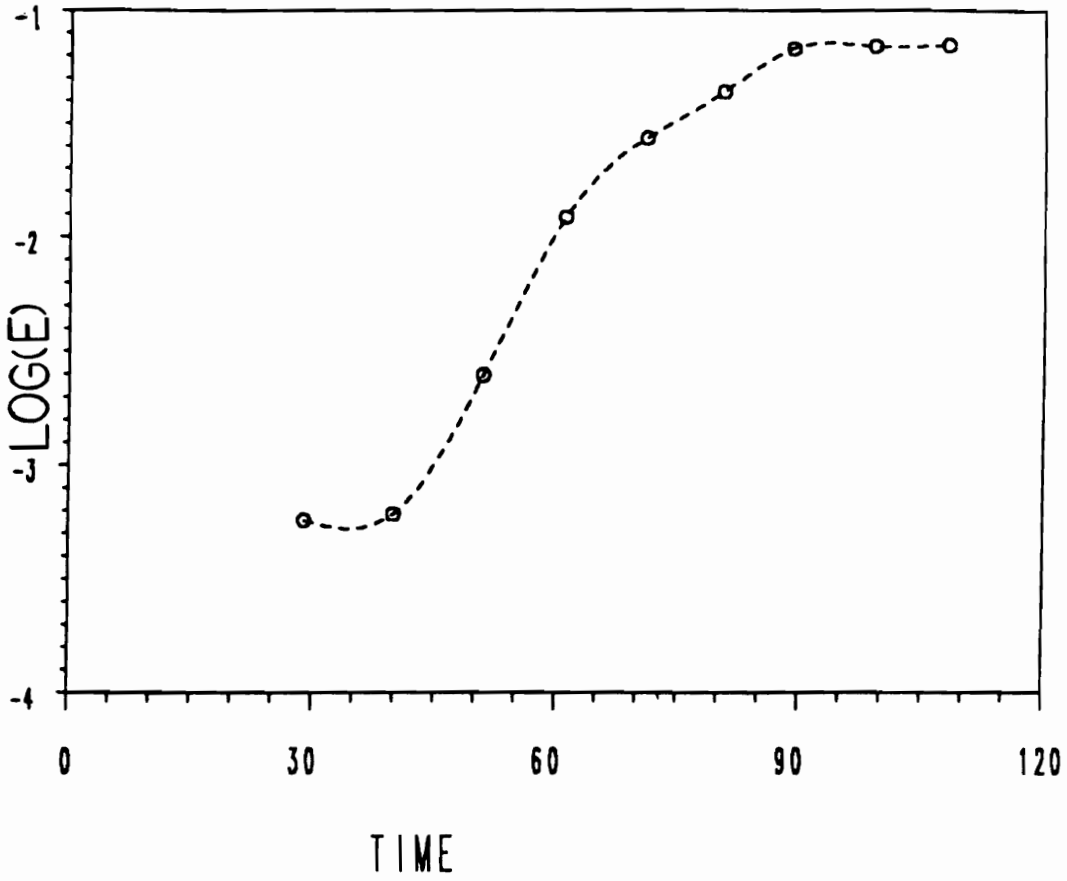

Fig. 6.39 Growth of kinematic energy in the small-scale motions; case B.

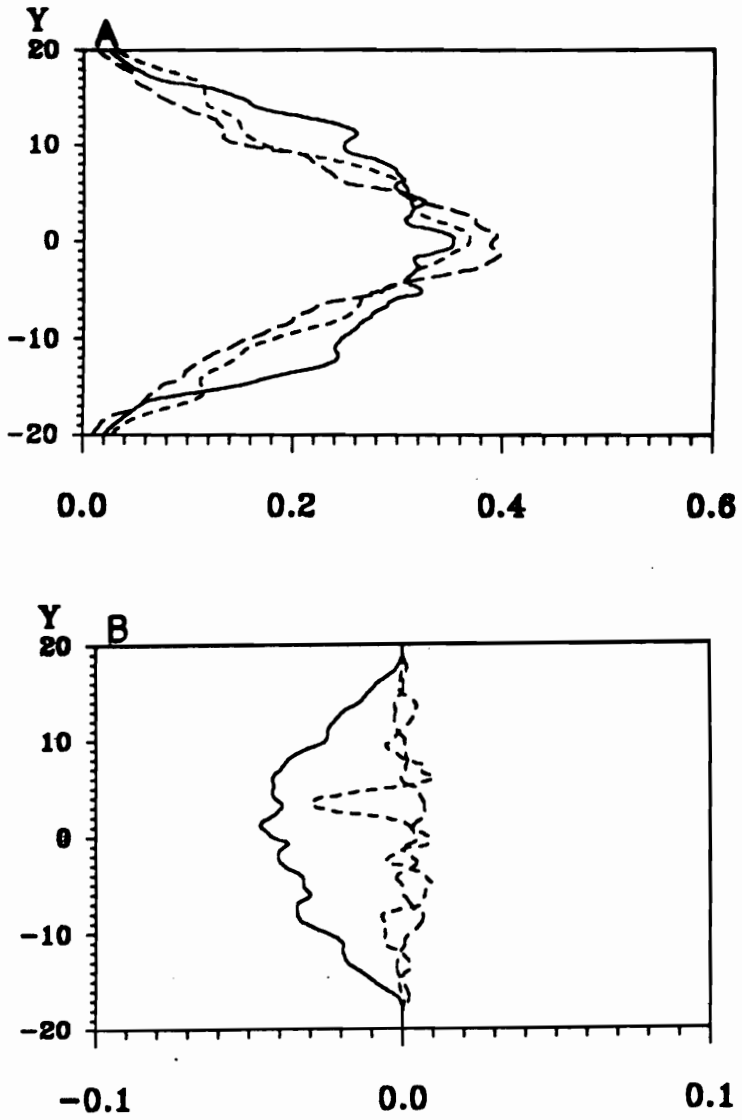

Fig. 6.40 (A) u', —; v', - - -; w', – – –. (B) $\overline{u'v'}$, —; $\overline{u'w'}$, - - -; $\overline{v'w'}$, – – –. $t = 108.4$, case B.

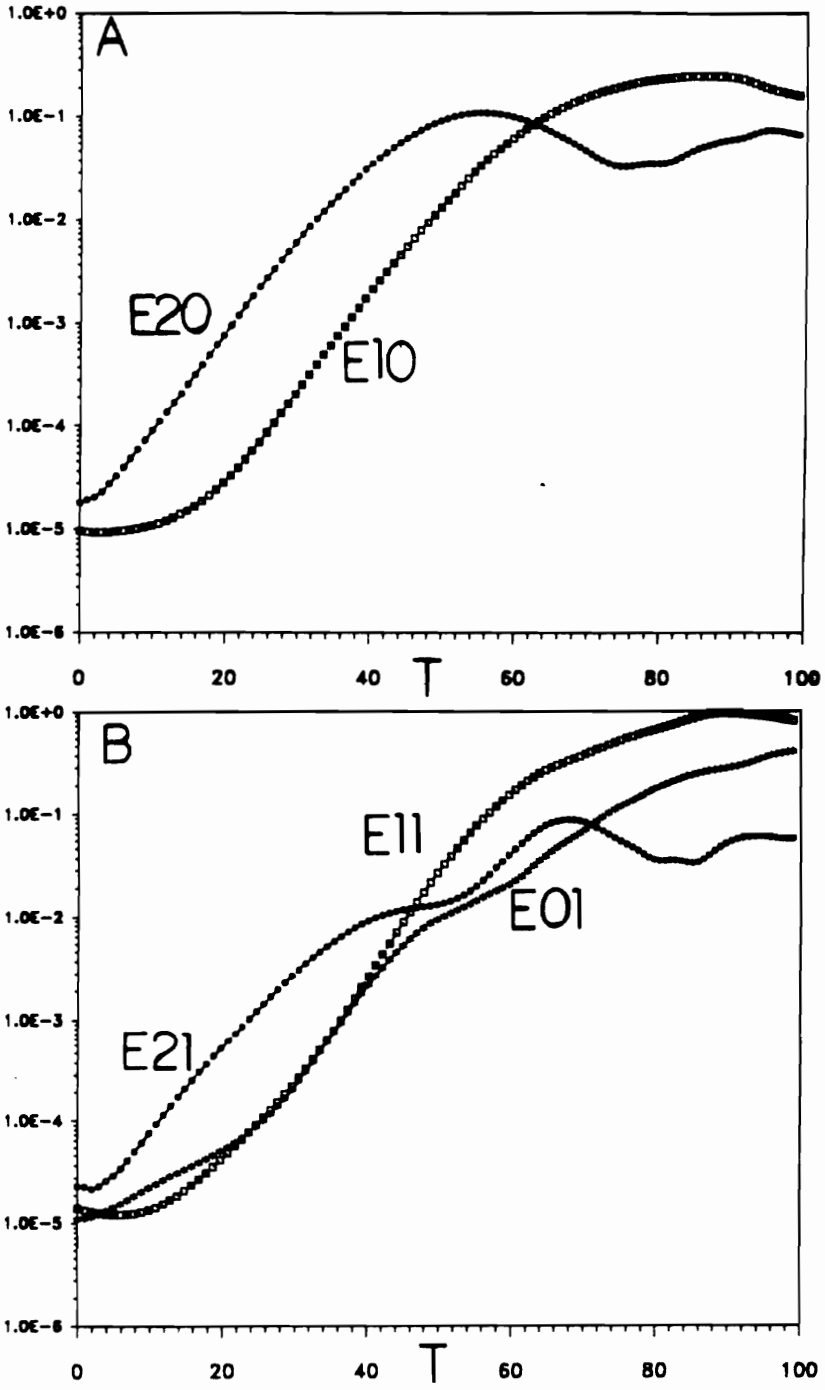

Fig. 6.41 Growth history of modal energy; case C.

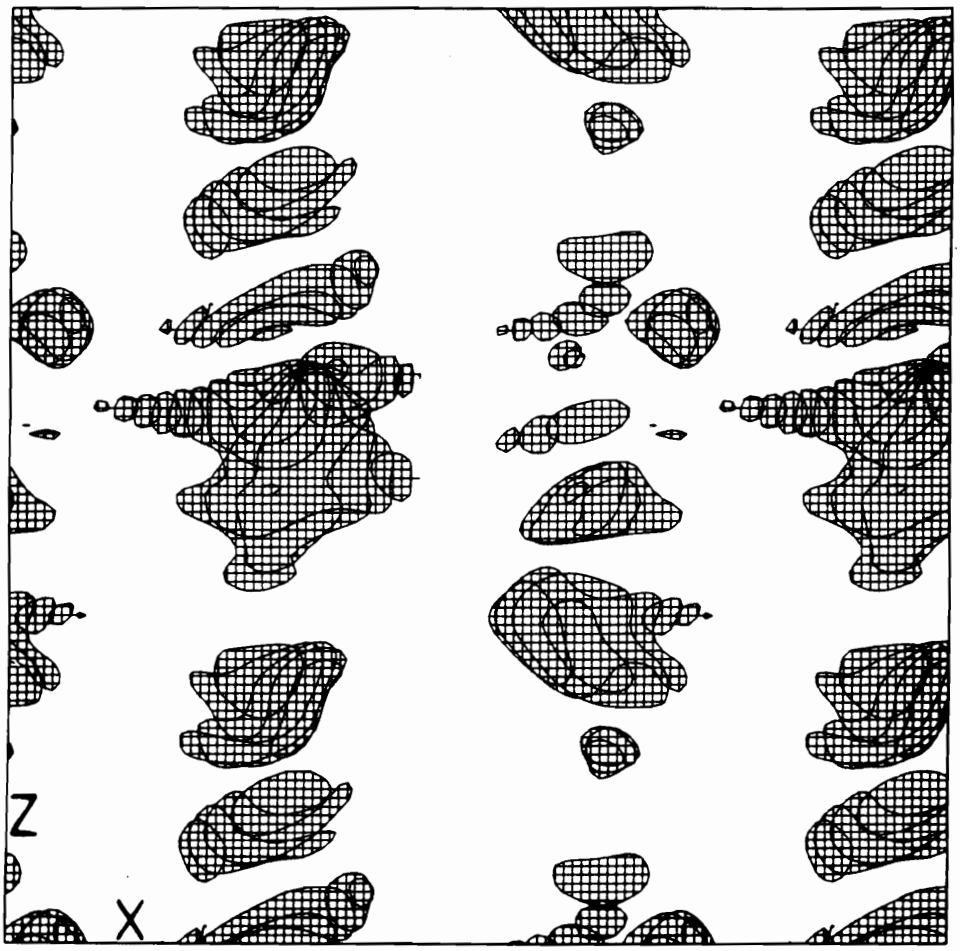

Fig. 6.42 Projection of constant ω_z surface on the $x - z$ plane; $t = 46.9$, case C; $\omega_z = -0.8$.

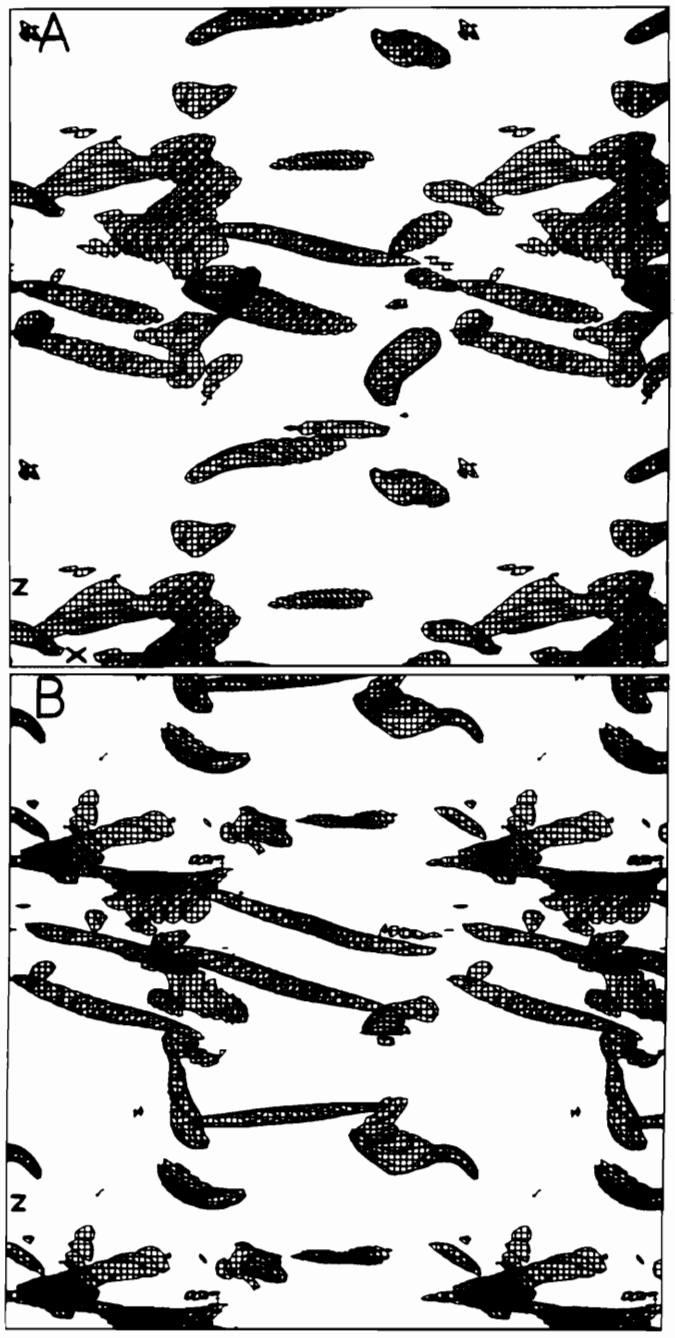

Fig. 6.43 Projections of constant ω_{xy} surface; case C; (A) $t = 56.03$, $\omega_{xy} = 0.65$, on $x - z$ plane, (B) $t = 64.7$, $\omega_{xy} = 1.0$, on $x - z$ plane, (C) $t = 64.7$, $\omega_{xy} = 1.0$, on $z - y$ plane; structures between $x = 0.43L_x$ and $x = 0.93L_x$.

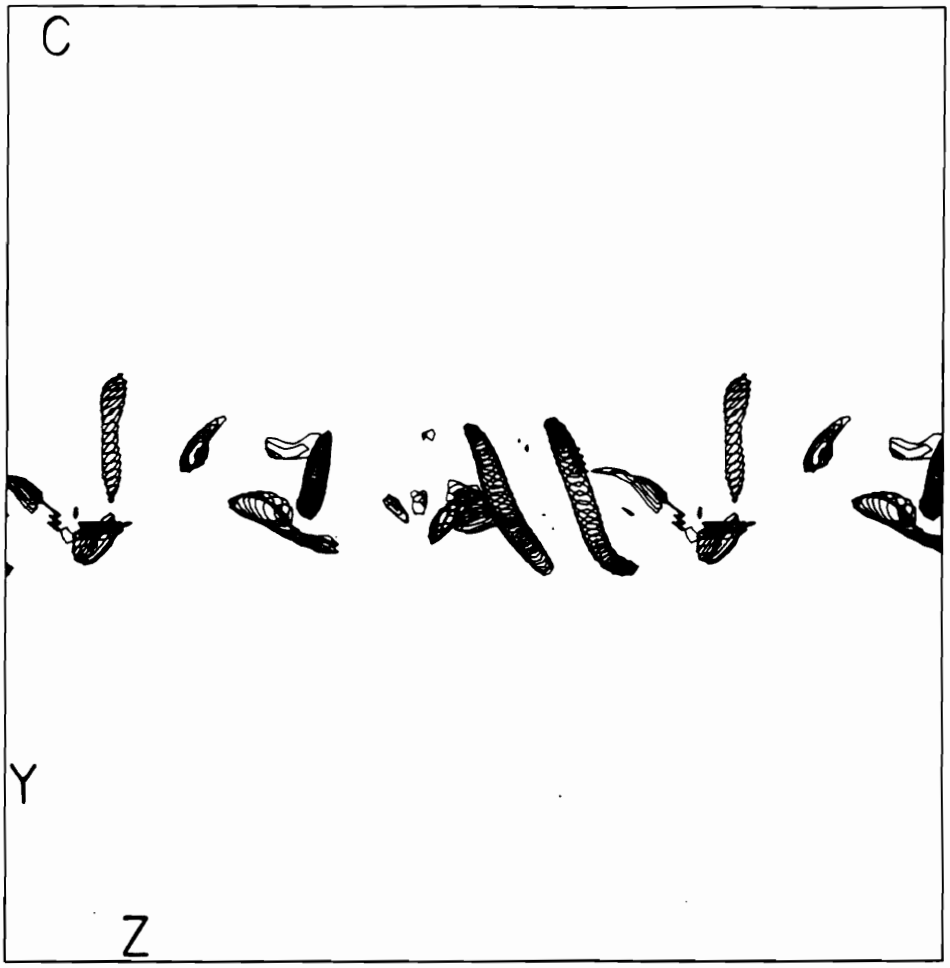

Fig. 6.43 (continued)

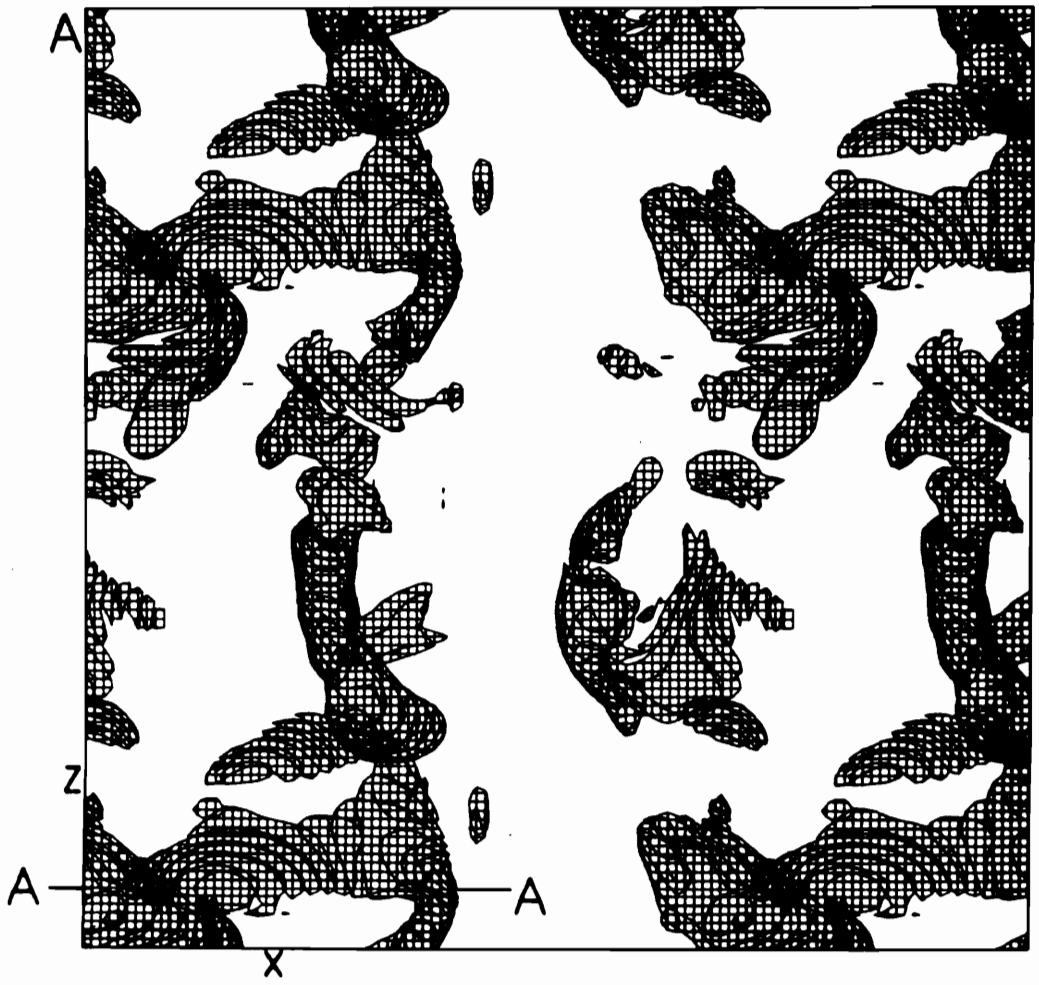

Fig. 6.44 (A) projection of constant ω_z surface on the $x - z$ plane, $\omega_z = -0.9$, (B) contours of ω_z in plane A-A in (A), $\omega_{max} = 0.478$, $\omega_{min} = -1.242$, (C) contours of ω_z in the $x - y$ plane at $z = 1/2L_z$, $\omega_{max} = 0.423$, $\omega_{min} = -2.115$; case C, $t = 64.7$.

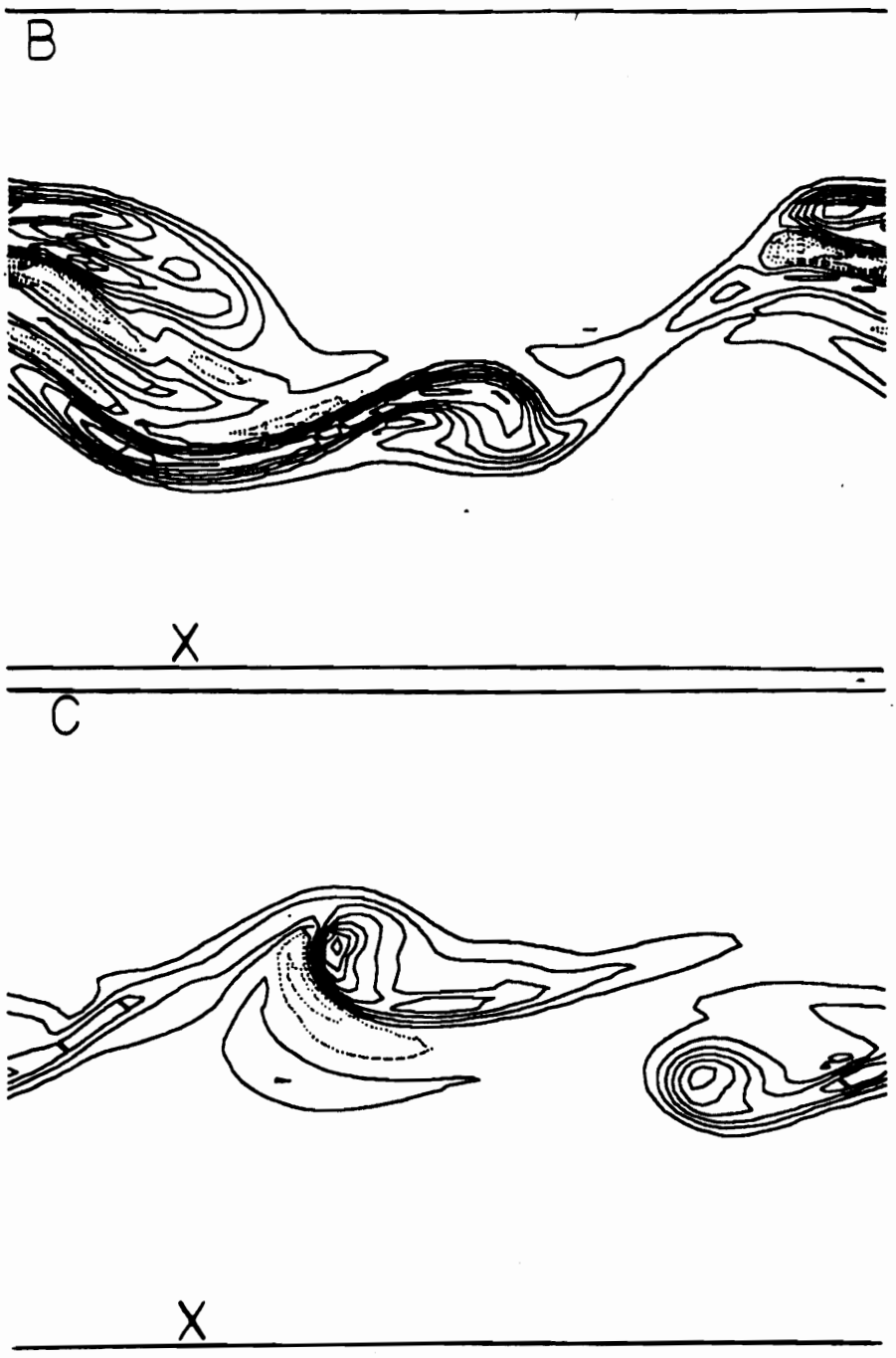

Fig. 6.44 (continued)

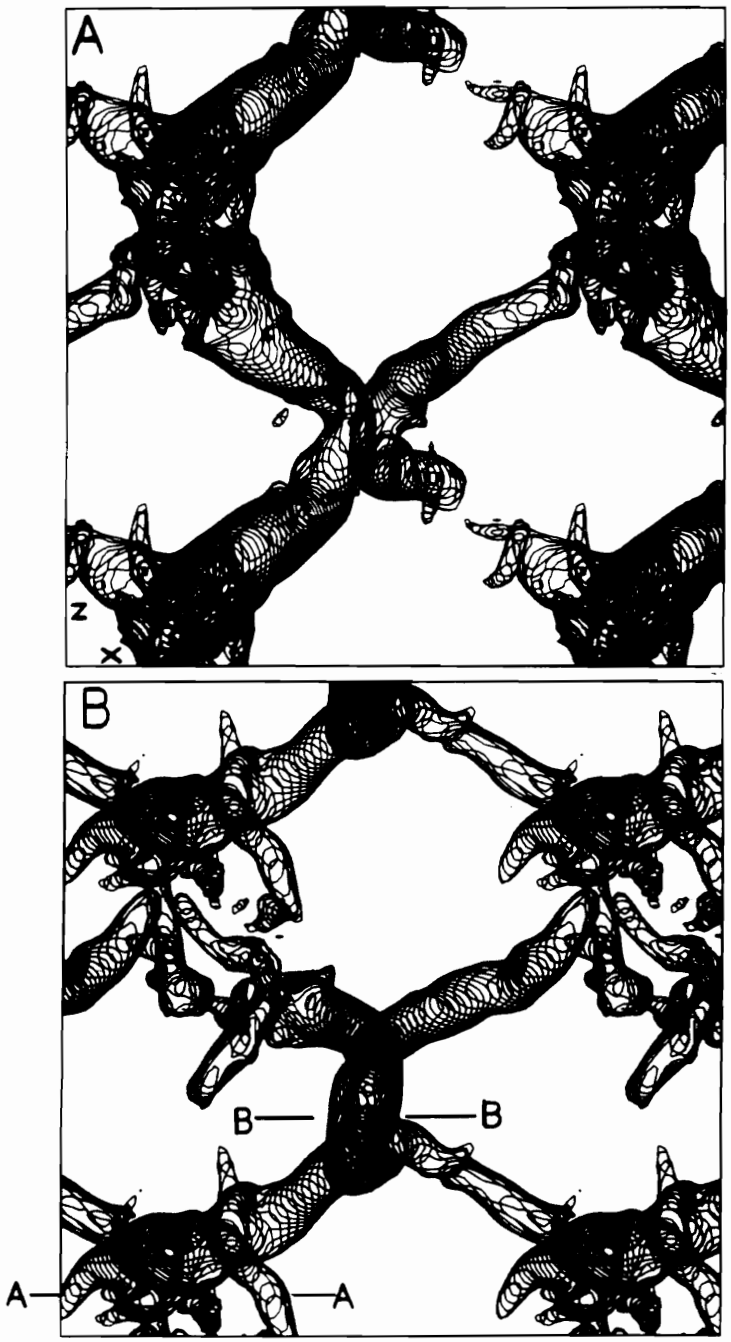

Fig. 6.45 Projections of constant pressure surface on the $x - z$ plane, case C; (A) $t = 89.7$, $P/(\rho_1 RT_1) = 0.90$, (B) $t = 98.9$, $P/(\rho_1 RT_1) = 0.89$.

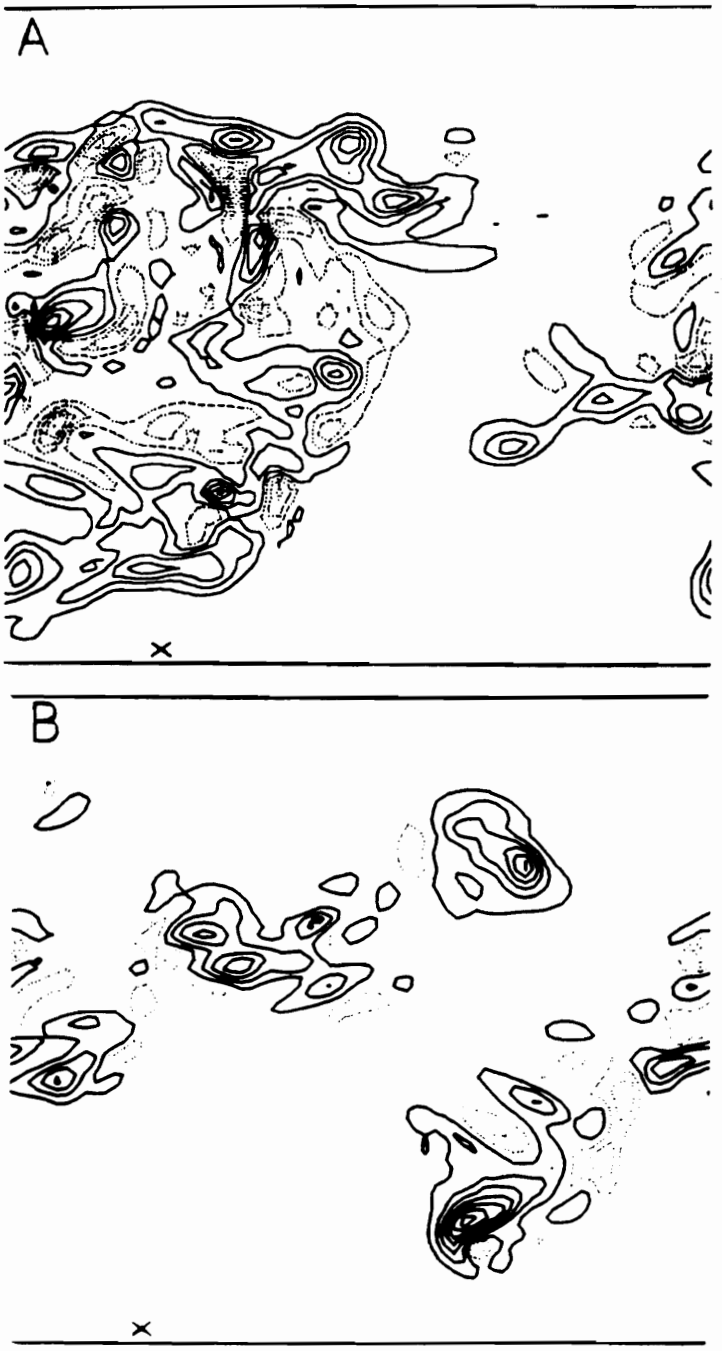

Fig. 6.46 Contours of ω_z; case C, $t = 98.9$; (A) plane A-A in Fig. 6.45, $\omega_{max} = 1.449$, $\omega_{min} = -1.449$, (B) plane B-B in Fig. 6.45, $\omega_{max} = 0.990$, $\omega_{min} = -2.574$; plots are truncated at $y = \pm 15$.

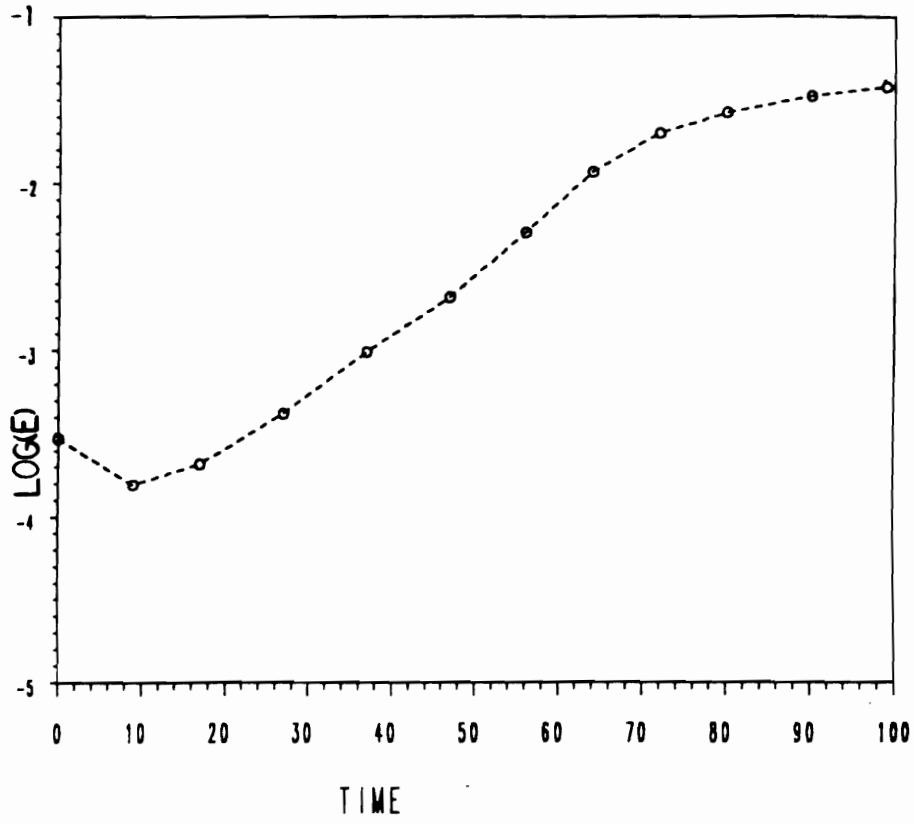

Fig. 6.47 Growth of kinematic energy in small-scale motions; case C.

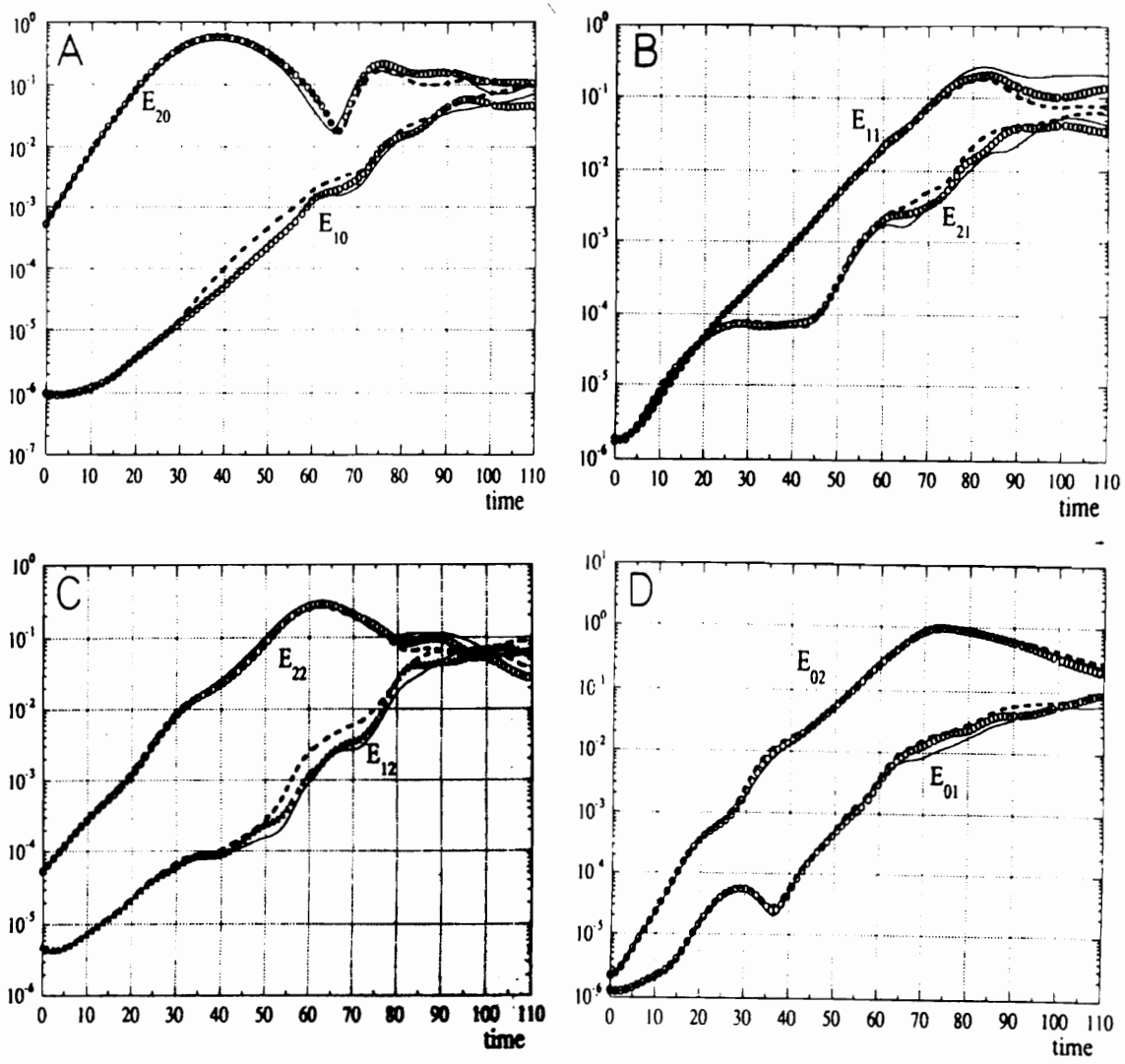

Fig. 7.1 Growth of modal energy. ooo, MacCormack, $C_R = 0.05$; - - - -, RK/central-difference, $C_R = 0.10$; —, flux-splitting, $C_R = 0.05$. All use Smagorinsky model.

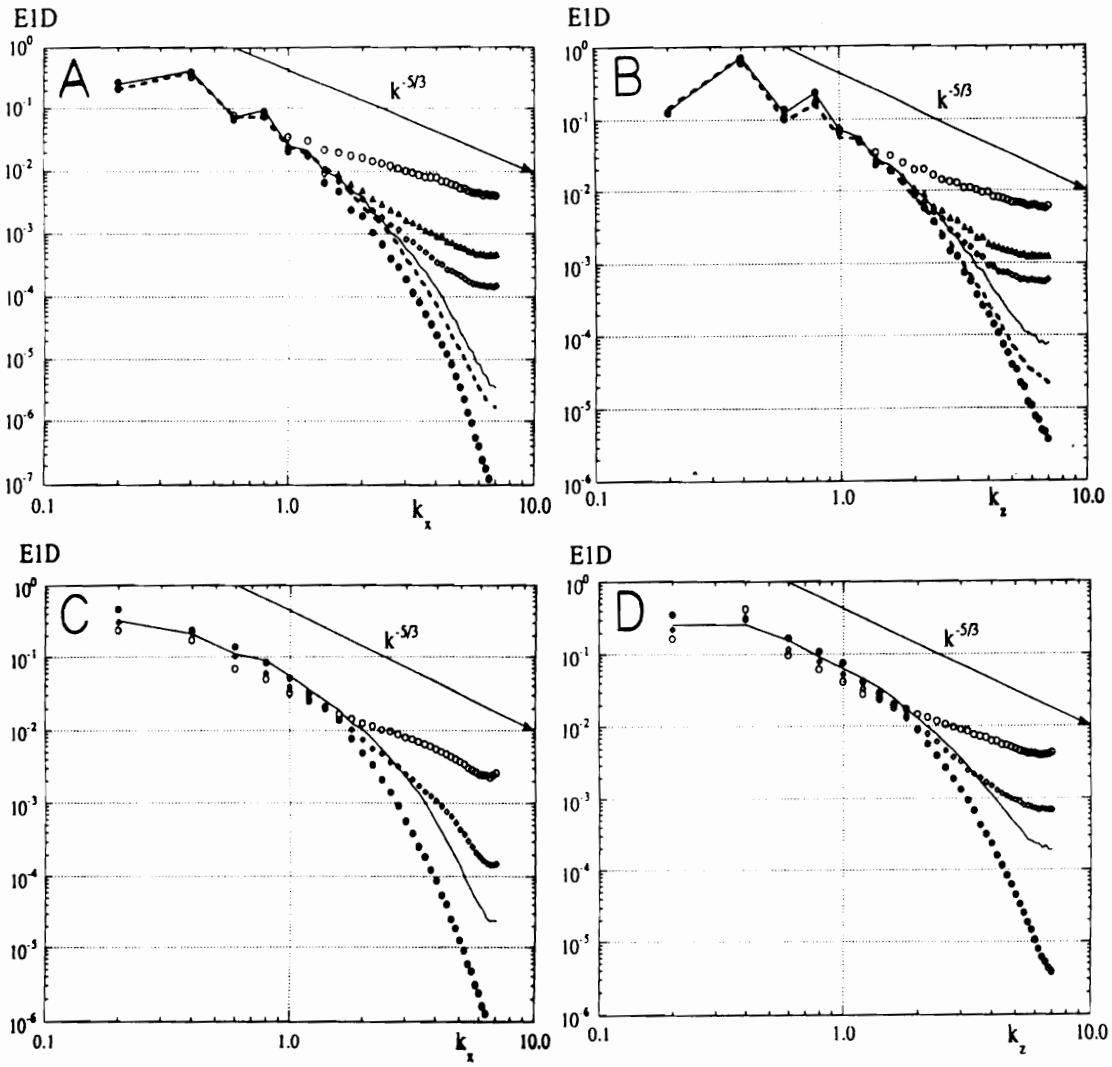

Fig. 7.2 Comparison of 1-D energy spectra (A) $t = 71, E_x$, (B) $t = 71, E_z$, (C) $t = 110, E_x$, (D) $t = 110, E_z$. —, MacCormack with Smagorinsky model, $C_R = 0.05$; - - - -, MacCormack with LCM, $C_R = 0.05$; ●●●, flux- splitting/RK, $C_R = 0.05$; ooo, central-difference/RK, $C_R = 0.05$; ◇◇◇, central-difference/RK, $C_R = 0.10$; △△△, central-difference/RK, $C_R = 0.08$. The RK schemes use Smagorinsky model.

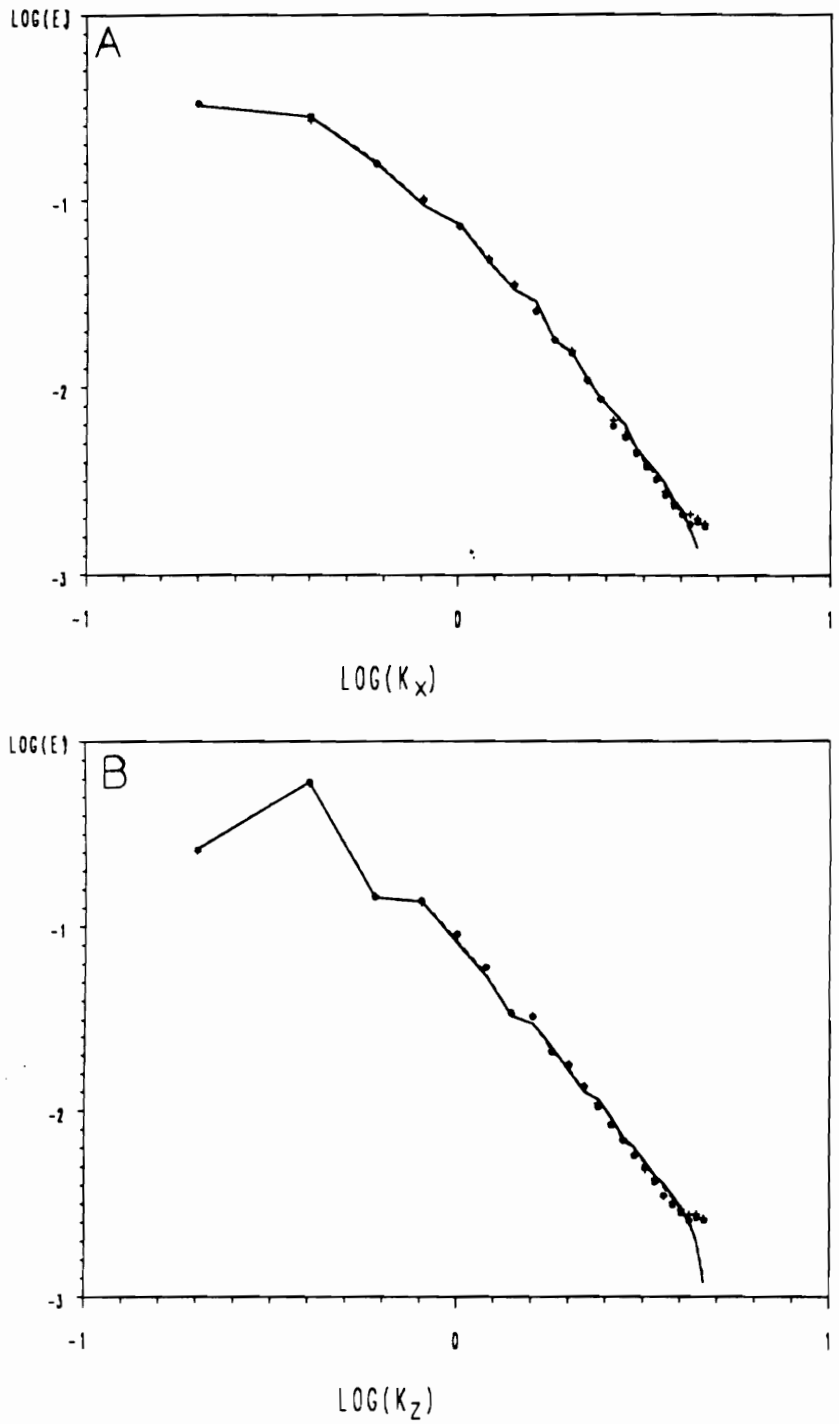

Fig. 7.3 Comparison of 1-D energy spectra of different dealiasing schemes; (A) E_x, (B) E_z; + + +, 2-step cut-square; ooo, 1-step cut-square; —, 2-step cut-circle; - - - -, 1-step cut-circle.

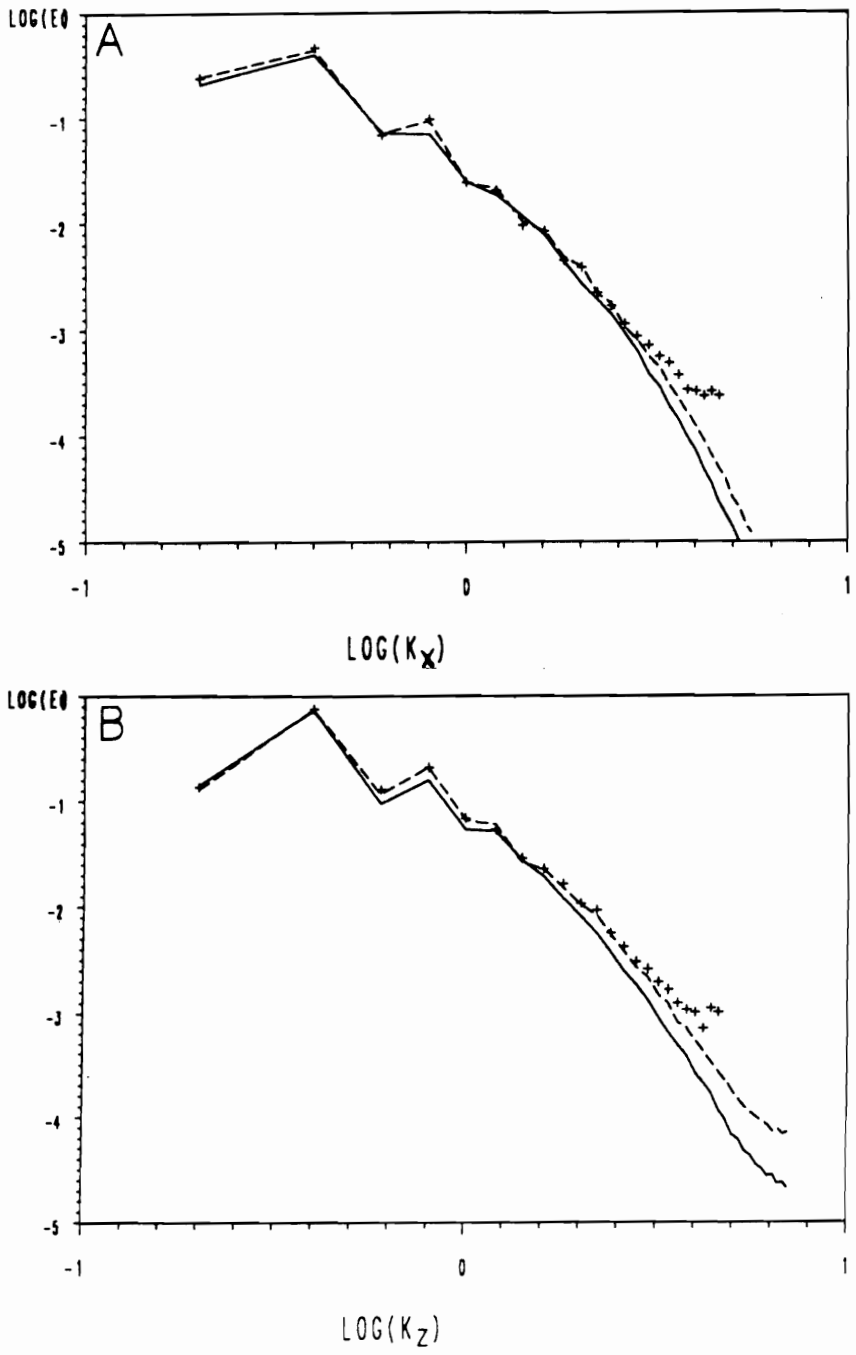

Fig. 7.4 Comparison of energy spectra of pseudo-spectral method and MacCormack scheme at $t = 71$. (A) E_x, (B) E_z; —, MacCormack with LCM; - - -, MacCormack with Smagorinsky model; + + +, pseudo-spectral with Smagorinsky model; (C) E_{3D}; + + +, MacCormack with LCM; square, MacCormack with Smagorinsky model; —, pseudo-spectral with Smagorinsky model.

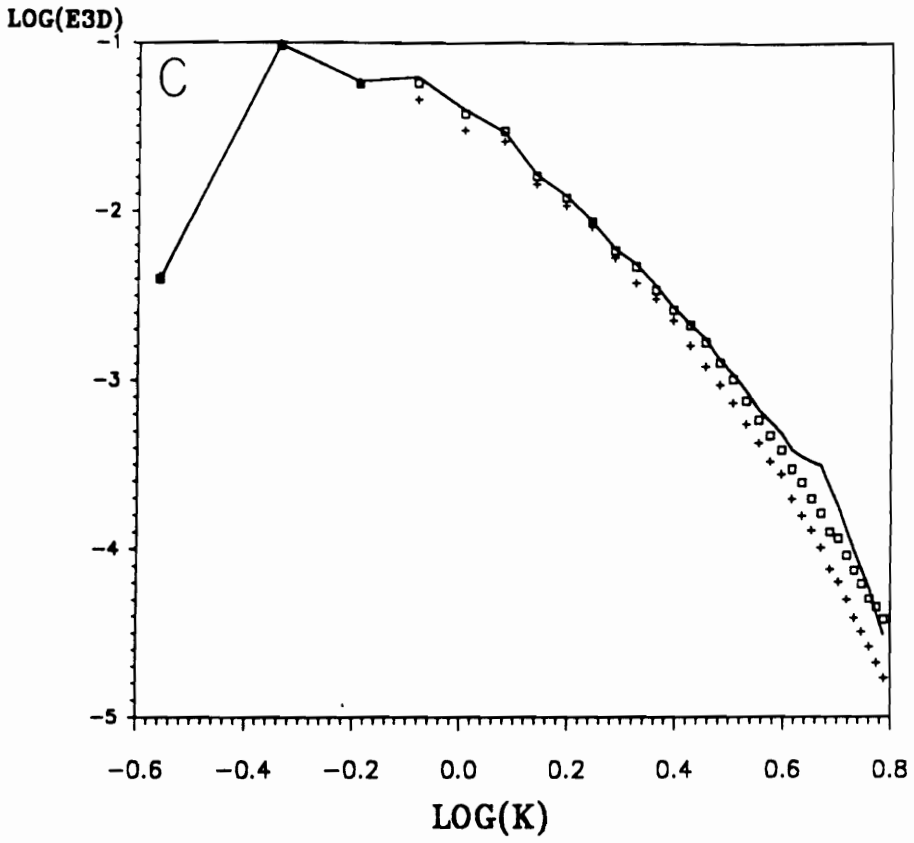

Fig. 7.4 (continued)

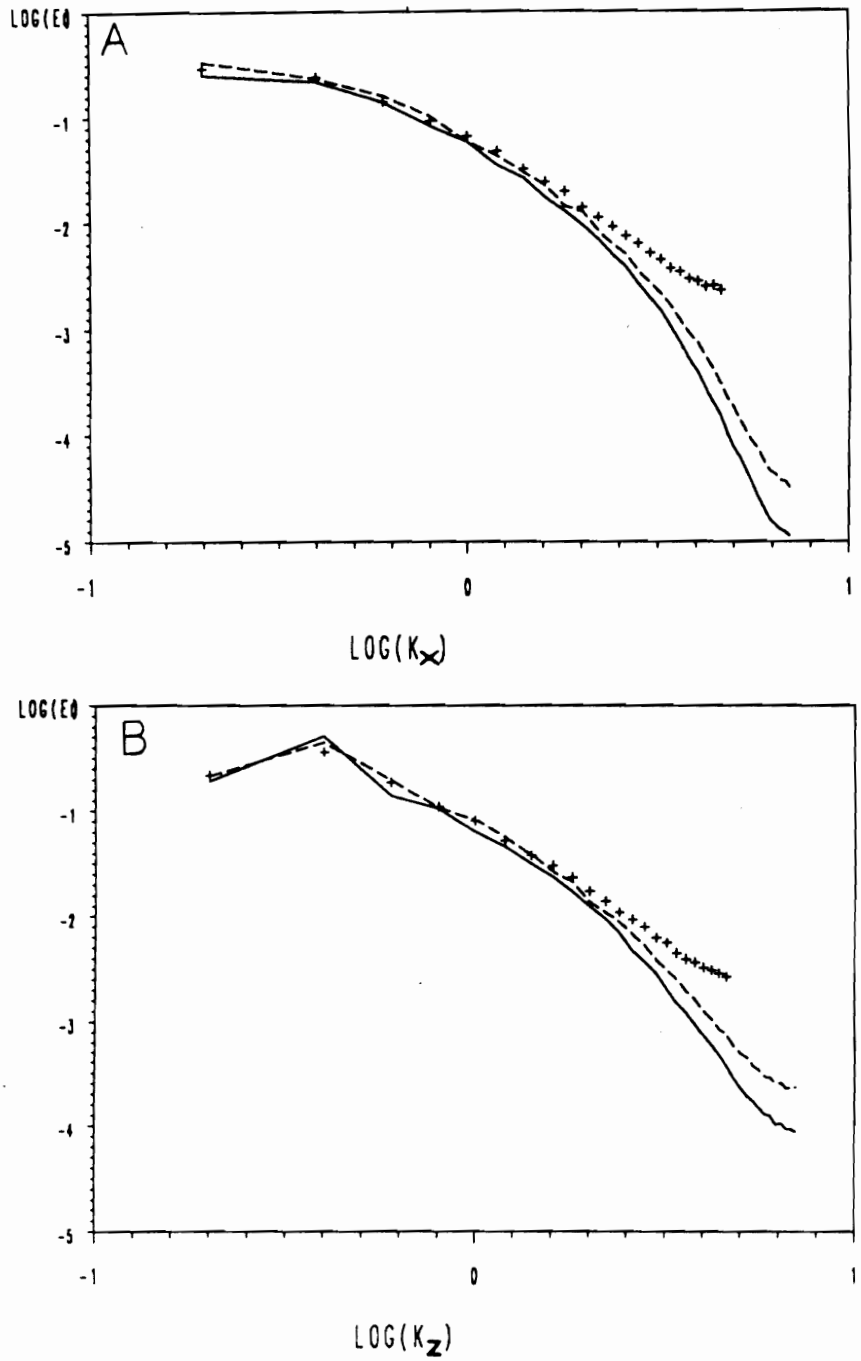

Fig. 7.5 Comparison of energy spectra of pseudo-spectral method and MacCormack scheme at $t = 99$; (A) E_x, (B) E_z; —, MacCormack with LCM; – – –, MacCormack with Smagorinsky model; + + +, pseudo-spectral with Smagorinsky model; (C) E_{3D}; + + +, MacCormack with LCM; square, MacCormack with Smagorinsky model; —, pseudo-spectral with Smagorinsky model.

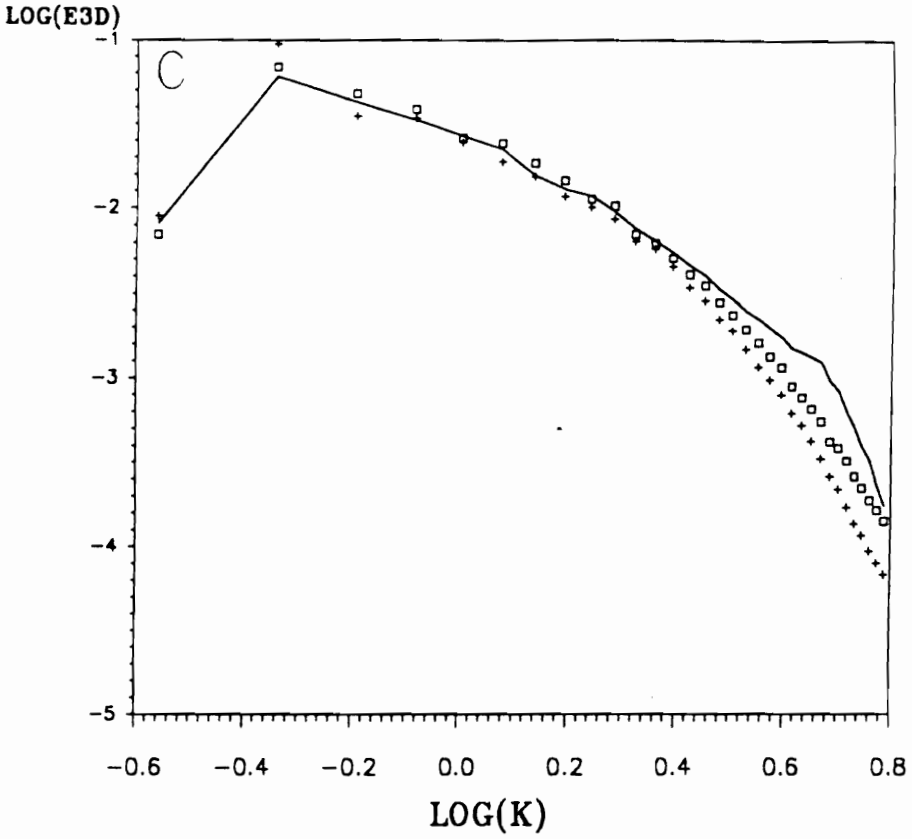

Fig. 7.5 (continued)

VITA

The author was born in Taiwan on April 8, 1961. He completed his undergraduate studies in mechanical engineering in Taiwan and earned a Master of Science in mechanical engineering from State University of New York at Stony Brook in December, 1986. He entered Virginia Polytechnic Institute and State University in August, 1988 to pursue a Doctor of Philosophy in engineering mechanics.